RAY W. HERRICK LABORATORIES

A Graduate Research Facility of The School of Mechanical Engineering

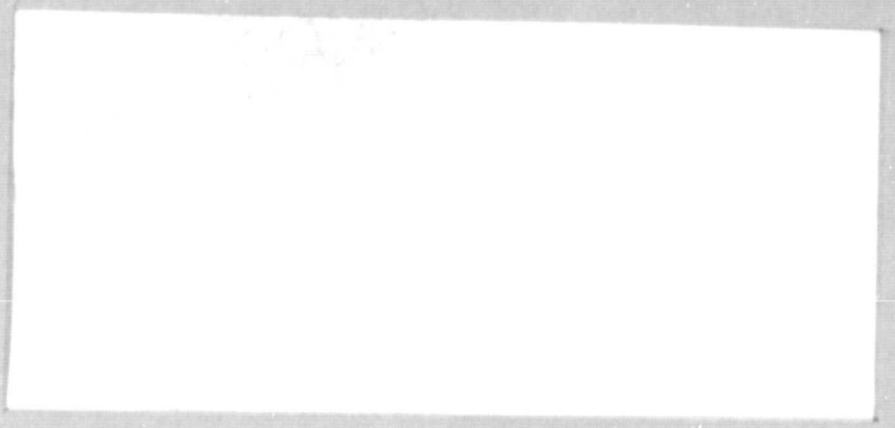

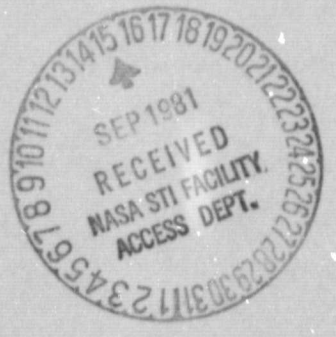

Purdue University

West Lafayette, Indiana 47907

A STUDY OF METHODS TO PREDICT AND MEASURE THE TRANSMISSION OF SOUND THROUGH THE WALLS OF LIGHT AIRCRAFT

Research Contract #NAG158
PRF #0121-52-12885

A STUDY OF METHODS OF PREDICTION AND MEASUREMENT OF THE TRANSMISSION OF SOUND THROUGH THE WALLS OF LIGHT AIRCRAFT

Sponsored by:

NATIONAL AERONAUTICS
AND SPACE ADMINISTRATION
Langley Research Center
Hampton, VA 23665

Report #1 HL 81-19

Submitted by:

B. Forssen: Graduate Research Assistant
Y. S. Wang: Graduate Research Assistant
P. K. Raju: Visiting Scholar
Malcolm J. Crocker: Principal Investigator

Approved by:

Raymond Cohen, Director
Ray W. Herrick Laboratories

August, 1981

PART I

CONTENTS

PART I

PART II

LIST OF FIGURES

LIST OF SYMBOLS

A_i = ith subarea of a complex structure, m^2

A_p = total panel area, m^2

A_2 = subarea No. 2 of the composite panel, m^2

a_1 = transverse acceleration at position 1, m/sec^2

a_2 = transverse acceleration at position 2, m/sec^2

B = bending stiffness, kgm^2/sec^2

C = speed of sound, m/sec

C_{pa} = real part of the one-sided cross spectral density between pressure and acceleration $(kg/sec^4)/Hz$.

E = Young's modulus, kg/sec^2m

E_i = total energy of the ith subsystem

E_1 = total energy of subsystem No. 1

E_2 = total energy of the subsystem No. 2

E_3 = total energy of the subsystem No. 3

$E\{\ \}$ = expected value of { }

f = frequency, Hz.

G_{12} = one-sided cross power spectrum between microphone systems 1 and 2, $(kg/ms^2)^2$

$\bar{G}_{12}$ = measured one-sided cross power spectrum between microphone systems 1 and 2, $(kg/ms^2)^2$

$|H_2|$ = gain of microphone system No. 2

I = magnitude of intensity, $watt/m^2$

$Im\{\ \}$ = imaginary part of { }

i = $\sqrt{-1}$

k = wavenumber, 1/m

$\overline{L_{p_1}}$ = space-averaged sound pressure level in the source room, dB

$\overline{L_{p_2}}$ = space-averaged sound pressure level in the receiving room, dB

L_w = sound power level, dB

m = mass per unit area, kg/m^2

m' = mass per unit length, kg/m

M_p = mass of panel, kg

M_{p_i} = mass of the ith subpanel, kg

M_{p_2} = mass of the 2nd subpanel in the composite panel, kg

M_{p_3} = mass of the 3rd subpanel in the composite panel, kg

N_1 = number of modes in a bandwidth Δ f of subsystem i

N_j = number of modes in a bandwdth of Δ f of subsystem j

n_i = modal density of the ith subsystem

NR = noise reduction, dB

p = sound pressure, Pa

p_{rms} = root mean squared pressure, Pa

P_B = power flow due to bending waves, watt

P_L = power flow due to longitudinal waves, watt

P_T = power flow due to tornsional waves, watt

p_1 = sound pressure at position 1, Pa

p_2 = sound pressure at position 2, Pa

Q = directivity factor

Q_{pa} = imaginary part of the cross spectral density between pressure and acceleration, $(kg/s^4)/Hz$.

$R_{i,rad}^{2\pi}$ = radiation resistance of the ith subarea on a complex structure

R_T = room constant

r_{ijk} = distance between source and observer, m

S = cross sectional area of a beam, m^2

T = reverberation time, sec.

T_2 = reverberation time in the receiving room, sec.

T_{12} = transfer function between microphone systems 1 and 2

TL = transmission loss, dB

TL_c = transmission loss of the composite panel, dB

TL_i = transmission loss of the ith subarea of a complex structure, dB

TL_1 = transmission loss of a subarea No. 1 of the composite panel, dB

TL_2 = transmission loss of subarea No. 2 of the composite panel, dB

T_s = torsional stiffness, m^4

U_r = particle velocity in the rth direction, m/s

V = volume, m^3

$\langle\ \rangle_t$ = time average of $\langle\ \rangle$

V_2 = volume of the receiving room, m^3

X_o = X-coordinate of the real source, m

X_k^+ = X-coordinate for image sources on the positive side of the X axis, m

X_k^- = X-coordinate for image sources on the negative side of the X axis, m

Y_o = Y-coordinate of the real source, m

Y_i^+ = Y-coordinate of the real source on the positive side of the Y axis, m

Y_i^- = Y-coordinate of the real source on the negative side of the Y axis, m

Z_o = Z-coordinate of the real source, m

Z_j^+ = Z-coordinate for image sources on the positive side of the Z axis, m

z_j^- = Z-coordinate for image sources on the negative side of the Z axis, m

GREEK LETTERS

α_1 = angular acceleration at position 1, rad/sec^2

α_2 = angular acceleration at position 2, rad/sec^2

α_r = average absorption coefficient of the right wall in the box

α_l = average absorption coefficient of the left wall in the box

α_u = average absorption coefficient of the upper wall in the box

α_b = average absorption coefficient of the bottom wall in the box

α_f = average absorption coefficient of the forward wall in the box

α_a = average absorption coefficient of the aft wall in the box

Δ = spacing between accelerometers, m

Δr = spacing between microphones, m

ϵ = energy density in a diffuse field, kg/s^2

$\Pi_{i,in}$ = input power to the ith subsystem, watt

$\Pi_{i,diss}$ = dissipated power of the ith subsystem, watt

$\Pi_{i,j}$ = power transfer between subsystems i and j, watt

Π_{nonres} = non-resonant power transfer, watt

$\Pi_{i,rad}$ = radiated power from the ith subsystem

$\Pi_{2,rad}$ = radiated power from subsystem 2, watt

$\Pi_{3,rad}$ = radiated power from subsystem 3, watt

Π_{ijk} = power radiated from image source with coordinates (i,j,k)

Π_{inc} = incident power, watt

ρ = density, kg/m^3

τ_i = transmission coefficient of the ith subarea of a complex structure

$\overline{\tau}$ = average transmission coefficient

τ_{nonres} = non-resonant transmission coefficient

$\tau_{i,nonres}$ = non-resonant transmission coefficient of the ith subpanel

η_i = internal loss factor of the ith subsystem

η_{ij} = coupling loss factor between subsystem i and j

$\eta_{i,rad}$ = radiation loss of the ith subsystem

ϕ = instrumentaion phaseshift, in degrees

ω = angular frequency, rad/sec

1. LITERATURE SURVEY

1.1 Introduction

After several decades of research in the development of a practical method for measuring acoustic intensity it was only recently that significant progress was made [1,2,3]. One, and probably the most important, reason behind this progress was the development of digital equipment for random data analysis capable of processing rapidly changing signals. In particular, the Fast Fourier Transform Analyzer has made it possible quite easily to perform measurement of sound intensity. Another important reason, has been the need to develop new methods of identifying noise sources and paths of propagation. The research has lately taken three paths associated with three different methods in obtaining the intensity inside of and radiated from a structure namely by use of, the surface intensity, the acoustic intensity and structural intensity methods.

All these methods are based on the estimate of the cross spectral density between two transducers and are therefore sometimes referred to as cross spectral methods. For the case of acoustic intensity the cross spectral density is calculated between two closely spaced microphones, for surface intensity between a microphone and an accelerometer and for structural intensity between two closely spaced accelerometers.

The surface intensity method [8-14] has been shown to be a useful tool in determining noise sources. One drawback is that

this method requires measurements at many microphone / accelerometer positions which makes the measurements on a big structure somewhat time consuming. Another drawback is the problem associated with the calibration of and phase shift between the microphone and accelerometer. However, a major advantage of the surface intensity method is that it gives the mean square surface velocity, radiated sound power and hence radiation efficiency of a vibrating surface all in one set of measurements.

The acoustic intensity method [1-7] does not have the drawbacks mentioned. Unless safety considerations prohibit, the microphones can be swept over the surface giving simultaneously both a spatially and time averaged-signal. The calibration as well as phase shift are easy to account for in a measurement program. This method of measurement of acoustic intensity has also opened the way for several important applications in the field of acoustics, which previously required more expensive facilities. This was demonstrated in our work in 1980 when this new method was successfully used in the evaluation of the sound transmission loss of structures. [4,5]

Very recently instrumentation has been developed by Bruel and Kjaer which is capable of evaluating and displaying in real time the acoustic intensity in one-third octave bands by using two closely spaced microphones. Another important factor, which has been carefully studied, is the calibration of and the ways of circumventing errors due to phase mismatch between the transducers [6,7]. The estimate of the cross spectra obtained from an

FFT Analyzer may be subject to some statistical errors. Some of these errors are discussed in reference 18.

It seems that least amount of work has been done on the method of measurement of structural intensity. [15,16,17]. This method might be very useful in determining reflection and transmission coefficients and coupling loss factors across structural joints.

Part one of this report presents both analytical and experimental results for the transmission loss of complex structures. On one side of the specimen the acoustic field is diffuse. On this side both the surface and acoustic intensity technique would give an erronous result when measuring the intensity since the pressure signal would then be composed of both incident and reflected soundwaves. On the other side of the specimen it was decided to use the acoustic intensity method.

In this chapter a brief review of the literature on surface intensity, acoustic intensity and structural power flow is presented.

1.2 Surface Intensity

Some important progress [8-14] has been reported on both the theory and application of the surface intensity technique as a tool for determining noise sources. The equation for the intensity is [13]

$$I = \frac{1}{2\pi} \int_0^\infty \left(\frac{1}{f}\right) \left[Q_{pa} \cos\phi + C_{pa} \sin\phi\right] df \qquad (1.1)$$

where Q_{pa} is the imaginary part of the one-sided cross- spectral density between pressure and acceleration, C_{pa} is the real part of the one-sided cross spectral density between pressure and acceleration and ϕ is the instrumentation phase shift. The main advantage with this technique is that it not only gives the radiated power but also the mean square surface velocity. Knowing both these quantities it is possible to calculate the radiation efficiency of the structure. It is important to note that a knowledge of the surface vibration is essential when attempting to reduce the emitted noise. One important drawback is that the method only works for the case of structure-radiated sound.

1.3 Acoustic Intensity

It appears that the first successful attempt to use the cross spectrum between two microphones was made by Alfredson [1]. He based his formulation assuming a simple harmonic signal. A more general expression was derived separately by Fahy [2] and Chung and Pope [3]. Probably the most useful expression for the acoustic intensity in connection with the use of a fast fourier analyzer was derived by Chung [6]. The equation for the intensity is as follows:

$$I = \mathrm{Im}\left[G_{12}\right]/\rho\ \omega\ \Delta r \qquad (1.2)$$

where Im ( ) stands for the "imaginary part of" and G_{12} is the one-sided cross-power spectrum ρ is the density, ω is the angular frequency and Δr is the microphone spacing. Chung also showed that by measuring the intensity twice, where the microphones and connections to the FFT were switched in the second measurement, he could circumvent the error caused by instrument phase mis-match. Another method of intensity measurement has been developed where the phase and gain mis-match errors are eliminated. This is accomplished by a microphone calibration, and consequently the measurement time is reduced by about a factor of two.

The errors associated with the finite difference approximation of the pressure gradient between the microphones have been carefully studied by Pavic. [15]

1.4 Structural Intensity

Quite an extensive study of the measurement of intensity of waves in structures is given by Pavic [16]. He has formulated methods for the cases of one- and two-dimensional wave propagation. The signal processing is done in the time domain with vibration transducers other than accelerometers. Similar work using accelerometers has been done by Verheij [17], in which the result is in the frequency domain. The equations for the power flow are expressed in terms of the spacing and cross power spectral density between two closely spaced accelerometers. The

power flow equations for bending waves on a beam are given by

$$\langle P_B \rangle_t = \frac{2(Bm')^2}{\Delta} \int_0^\infty \frac{\mathrm{Im}\left[G\ (a_1, a_2)\ \right]}{\omega^2}\, df \tag{1.3}$$

and for longitudinal (L) and torsional (T) waves on a beam-like structure are,

$$\langle P_L \rangle_t \approx \frac{-SE}{\Delta} \int_0^\infty \frac{\mathrm{Im}\left[G\ (a_1, a_2)\ \right]}{\omega^3}\, df \tag{1.4}$$

$$\langle P_L \rangle_t \approx \frac{-T_s}{\Delta} \int_0^\infty \frac{\mathrm{Im}\left[G\ (\alpha_1, \alpha_2)\ \right]}{\omega^3}\, df \tag{1.5}$$

where a_1 and a_2 are the transverse accelerations, and α_1 and α_2 are the angular accelerations of the accelerometers, $G(a_1, a_2, f)$ is the one sided cross spectral density between the accelerometers, S is the cross sectional area, E is Young's modulus of elasticity, T_s is the torsional stiffness, B is the bending stiffness, m' is the mass per unit length and Δ is the spacing between transducers. The same reference also gives a table where equivalent signal processing operations in the time and frequency domain are presented.

2. THE APPLICATION OF THE ACOUSTIC INTENSITY TECHNIQUE TO THE SOUND TRANSMISSION LOSS OF PANEL STRUCTURES

2.1 Introduction

In this chapter a new approach for evaluating the transmission loss of panels is presented. This approach is based on an estimate of the cross power spectrum between two closely spaced microphones [6]. The measured results will be compared with the transmission loss obtained by the conventional method, as well as the well known mass law. It will also be shown that by using this approach it is possible to identify paths of acoustic energy flow through a composite panel structure.

2.2 Historical Background

The transmission loss is defined as ten times the common logarithm of the sound power incident on the structure divided by the transmitted sound power. In principle the receiving side should be anechoic [19]. It seems that Buckingham [20] presented the first theoretical formulation of the transmission loss of a partition separating two reverberant rooms. This method which is the current standard, requires two reverberant rooms. The transmission loss is given by the difference between the space-averaged sound pressure levels of the two rooms. However, there seems to be some scatter in the data obtained by this method even for laboratory measurements with a simple panel [21]. The same problem for the case of field measurements is discussed in

reference [22]. Besides these difficulties the method is also inapplicable whenever the receiving side is a free space or is very dead. Suggestions to overcome this problem are discussed in references [23,24]. Quite an extensive survey on available analytical models together with a comparison with measured data are presented in references [25,28].

The new method [4,5] to be discussed, has advantages over the conventional method since only one reverberant room is required and that corrections for the panel area and absorption on the receiving side are not needed. The new method also provides a means of determining the sound power transmitted through different parts of a composite structure. In this report a single and a composite panel were chosen to verify the new method. A comparison was made between the measured transmission loss obtained by using the acoustic intensity technique and that obtained by the conventional method and the mass law. The surface intensity [13,14] technique would be an alternative way of measuring the transmitted sound power.

2.3 Transmission Loss of a Panel and its Measurement

The difference between the incident and transmitted intensity level is needed to rate the insulation of a panel [25]. There is no doubt that the transmission suite method is the most frequently used method for measurement of the transmission loss [27]. In this method the two reverberant rooms should be well

vibration-isolated to prevent mechanical transmission between rooms. The volume of a reverberant room sets the lower limiting frequency for a diffuse field. The excitation in the transmission room should be steady. By either using a rotating boom in each room or simply measuring simultaneously over an ensemble of microphones or by repeating the measurement for various microphone positions, space-time-averaged sound pressure levels in each room $\overline{L_{p_1}}$ and $\overline{L_{p_2}}$ can be obtained. The noise reduction is then defined as:

$$NR = \overline{L_{p_1}} - \overline{L_{p_2}} \quad . \tag{2.1}$$

Provided that the flanking transmission can be neglected, the transmission loss is given by: [27]

$$TL = NR + 10 \log \left[\frac{A_p c T_2}{24\ V_2\ Ln(10)} \right] \tag{2.2}$$

where A_p is the area of the panel, T_2 is the the reverberation time of the reception room, V_2 is the volume of the reception room and c is the speed of sound. The mass law is given by:

$$TL = 20 \log(mf) - 48 \text{ dB} \tag{2.3}$$

where: m = mass/unit area (SI units), and f is the frequency, Hertz.

The reception room was simulated by a large wooden box of 2.8 m^3 volume. Care was taken to seal the box. The sound pressure

level was averaged over 9 microphone locations in the box.

In the case of a composite panel with several elements composed of different materials having different transmission coefficients τ_i, i=1,2,3... and corresponding areas A_i, i=1,2,3,..., the average transmission coefficient is given by [29]

$$\bar{\tau} = \frac{1}{A_p} \Sigma A_i \tau_i \qquad (2.4)$$

where $A_p = \sum_i A_i$ is the total panel area. The transmission loss of the composite panel is then:

$$TL_c = 10 \log\left[\frac{1}{\bar{\tau}}\right] \qquad (2.5)$$

for a two element wall it can be shown [29] that the transmission loss is given by

$$TL_c = TL_1 - 10 \log \left[1 - \frac{A_2}{A} + \left[\frac{A_2}{A}\right] 10^{\left[TL_1 - TL_2\right]}\right] \qquad (2.6)$$

where

$$TL_i = 10 \log\left[\frac{1}{\tau_i}\right] , \quad i = 1,2$$

2.4 Diffuse Field Intensity and Acoustic Intensity

The average rate of flow of sound energy through and normal to a unit area in a sound field is by definition, the sound intensity in that direction [31]. The energy density in a diffuse field is given by [30]

$$\epsilon = p_{rms}^2/\rho c^2 \qquad (2.7)$$

and the space-time averaged intensity is given by [30]

$$\langle I \rangle_t = p_{rms}^2/4\rho c \qquad (2.8)$$

where p_{rms} is the rms sound pressure, ρ is the density of air and c is the speed of sound.

2.5 Acoustic Intensity by Cross Spectral Method.

Consider two omni-directional pressure microphones separated by a distance r. For a random, stationary, ergodic signal [31], the acoustic intensity I_r at a location in a sound field in a given direction r is [5,6]

$$I = E(pu_r) \qquad (2.9)$$

where E( ) stands for the expected value and p and u_r are the acoustic pressure and particle velocity respectively. The pressure in equation (10) is the pressure at the midpoint between the microphones. It can be approximated by the mean value

$$p = \frac{p_1 + p_2}{2} \tag{2.10}$$

where p_i, $i = 1,2$ is the signal response from the microphones. By using a centered finite difference approximation [36] it can be shown that the particle velocity can be expressed as

$$u_r = \frac{i\,(p_2 - p_1)}{\rho\,\Delta r\;\omega} \tag{2.11}$$

where ω is the angular frequency. This derivation is based on the criterion that $k\Delta r \ll 1$. Using equations (10), (11), and (12), it can be shown that the intensity is given by [6]

$$I_r = \mathrm{Im}\left[G_{12}\right] / \rho\,\Delta r\;\omega \tag{2.12}$$

where Im( ) means the imaginary part of the argument, G_{12} is the one sided cross power spectrum between the two pressure signals. By using the transfer function between the two microphones, the correction for the phase shift can be included in the measurement method. The corrected cross power spectrum is [5]

$$G_{12} = \frac{\bar{G}_{12} T_{12}}{|H_2|^2} \tag{2.13}$$

where $\bar{G}_{12}$ is the measured cross spectrum between the two microphones, T_{12} is the transfer function between microphone systems 1 and 2 and $|H_2|$ is the gain of microphone system 2. For a description of the procedure in measuring the transfer function see the next section.

2.6 Experimental Measurements

2.6.1 Introduction

The diffuse field in the reverberation room was measured by taking about 100 samples of the pressure signal from a rotating microphone boom during which time it made about two revolutions. The transmitted intensity was obtained by using the acoustic intensity method. The pair of microphones were swept with the center line of the pair held perpendicular to the panel surface. The distance between the midpoint of the microphones and the panel surface was about 20 mm. The speed with which the sweeping was done was approximately 4 cm/sec. The panel was clamped in an iron frame and fixed in the window of the reverberant room. The edges were sealed with clay to reduce the flanking transmission. A schematic diagram of the experimental set up is shown in Figure 2.1. A diffuse field was used for the excitation of the single panel. This field was generated by an air jet noise source which gave most power in the higher frequencies and a loud speaker fed by a random noise generator which provided high levels for the lower frequencies. The spectrum was fairly flat and the overall level came to about 110-120 dB. During later measurements on the composite panel, the loudspeaker was replaced by a pneumatic driver which increased the levels at the lower frequencies and raised the overall sound pressure level (SPL) in the reverberant room to about 133 dB.

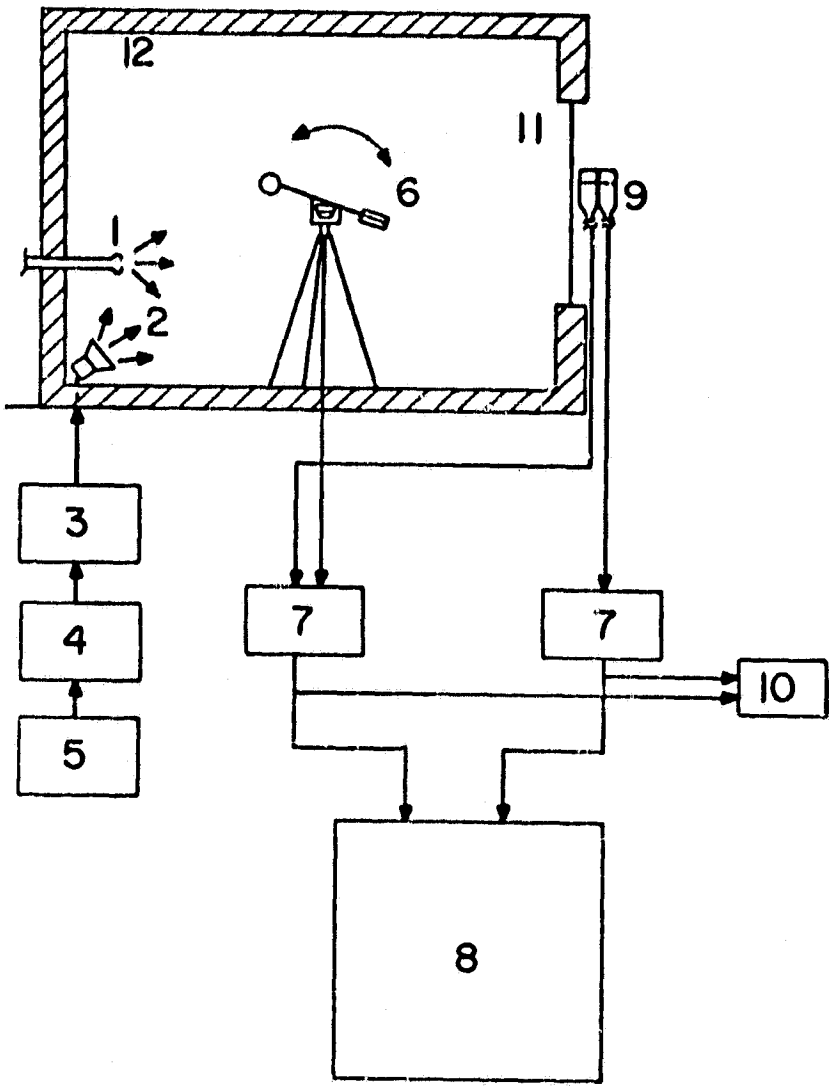

Figure 2.1 Experimental set-up for measurement of transmission loss of a panel by acoustic intensity method.

1. Jet Noise Source
2. Loudspeaker
3. Power Amplifier GR1308A
4. Band Pass Filter, Krohn-Hite, 3343
5. RN Generator, GR1381
6. Rotating Boom, B&K3923 Microphone B&K4133
7. Measuring Amplifier B&K2107
8. FFT Analyzer HP5451C
9. Microphones, B&K4133
10. Oscilloscope, Tektronix 5103N
11. Panel
12. Reverberation Room

2.6.2 Measurement of Acoustic Intensity

The experimental set-up for measuring the transfer function between the two microphones is shown in Figure 2.2. The 1/2 inch microphones were calibrated before they were inserted at the end of the tube. A loud speaker driven by a random noise generator was fixed at the other end of the tube. The tube was made long enough to assure that plane waves existed at the location of the microphones. The signals from the microphones were fed through two measuring amplifiers before being processed by the FFT system. The transfer function was evaluated by using a key-board program.

The experimental set up for measuring the acoustic intensity is shown in Figure 2.1. The array of two microphones were taped together. Their separation distance was about 14 mm as discussed in section 2.6.1. The acoustic intensity was then computed from the cross power spectrum of the two microphones as given in equations (13) and (14).

2.6.3 Measurement of Free-Field Intensity

The two microphone intensity technique was tested in the following way. The plane wave intensity was measured in an anechoic room by using the two-microphone technique. One hundred samples of the pressure signals were taken. This result was compared with the plane wave intensity $p_{rms}^2/\rho c$, evaluated from the auto-power spectrum from one of the microphones.

The noise source was a loudspeaker fed by a random noise generator. The measurements were made at a distance of 1.5 m from the loudspeaker. Figure 2.3 shows a comparison between the two methods in obtaining the intensity. This shows that the agreement is good between 400 and 2500 Hz. For frequencies below 400 the discrepancy is about 0.5 dB and above 2500 Hz. it is about 1.5 dB.

2.7 Measurement of Diffuse Field Intensity

A second test was performed to verify the two-microphone method. The diffuse field intensity $p^2_{rms}/4\rho c$, was measured inside the reverberation room while the window was open. The noise source consisted of a jet noise source run in combination with a loudspeaker. The auto-power spectrum of the pressure signal measured by a microphone on the rotating boom was sampled 100 times. The intensity at an imaginary surface in the open window in one wall of the reverberant room was then obtained by the acoustic intensity method. The signal was sampled at the same rate as in the previous measurement.

Figure 2.4 shows the plots of diffuse field intensity in narrow bands obtained by these two methods. Curve number 2 has been lowered by 10 dB to show clearly the very good similarity between the two curves. The measurements were made by 1/4 inch microphones. The corresponding plot in one-third octave band averaged values is shown in Figure 2.5. The discrepancy above 4000 Hz. is most likely with the two-microphone results and is

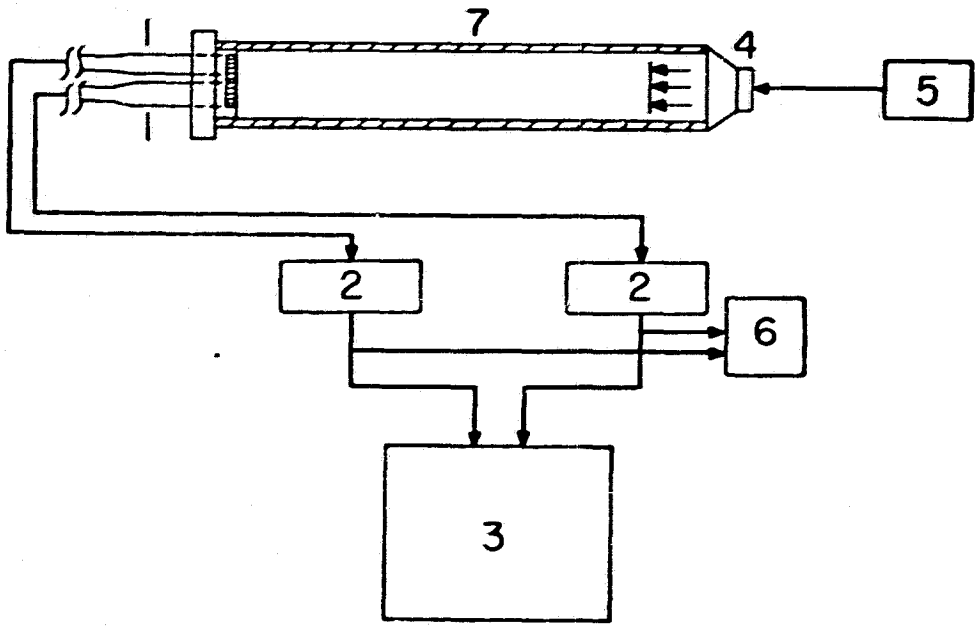

Figure 2.2 Experimental set-up for the measurement of transfer function.

1. Microphone, B&K4133
2. Measuring Amplifier B&K2107
3. Fast Fourier Analyzer, HP5451C
4. Loudspeaker
5. RN Generator, GR1381
6. Oscilloscope, Tektronix 5103N
7. Tube

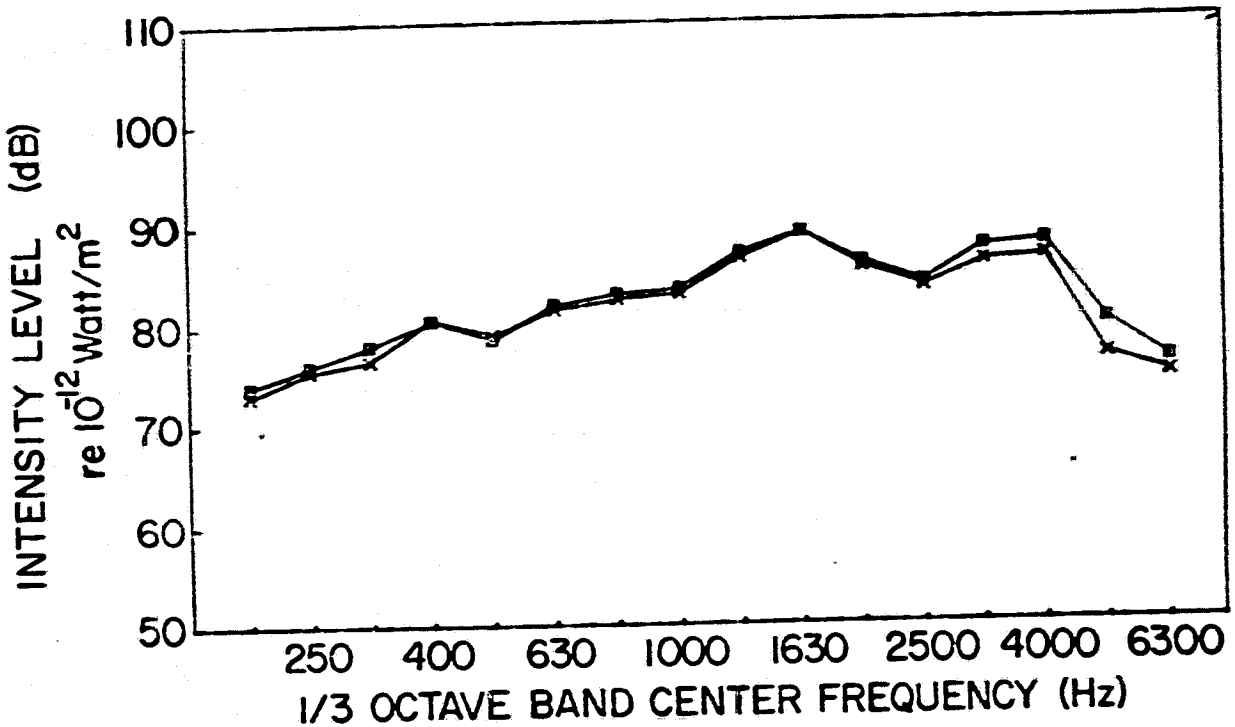

Figure 2.3 Comparison of free field intensities.

□-□-□-□-□- free field intensity obtained from $(p^2_{rms}/\rho c)$;

x-x-x-x-x-x-x by acoustic intensity measurement.

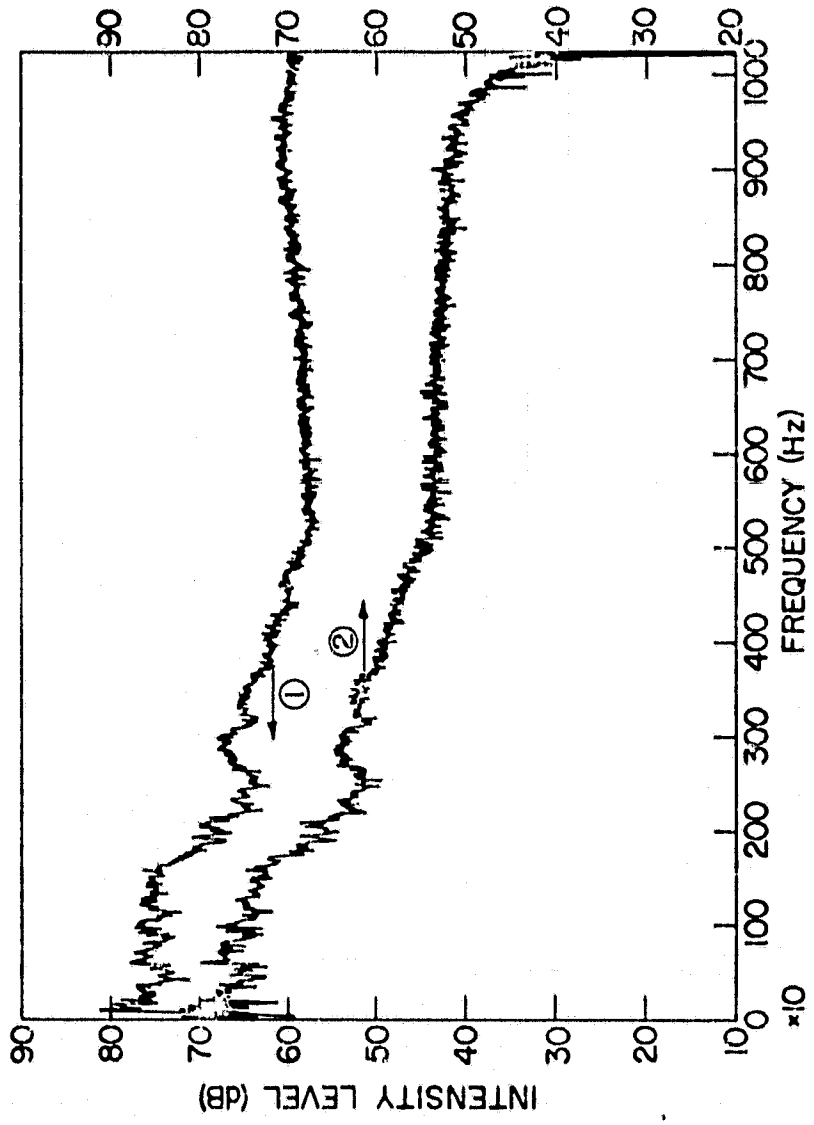

Figure 2.4 Comparison of diffuse field intensities averaged over narrow frequency bands.

1 from $p^2_{rms}/4\rho c$ from single microphone measurement in diffuse field

2 from two-microphone acoustic intensity measurement in an open "window"

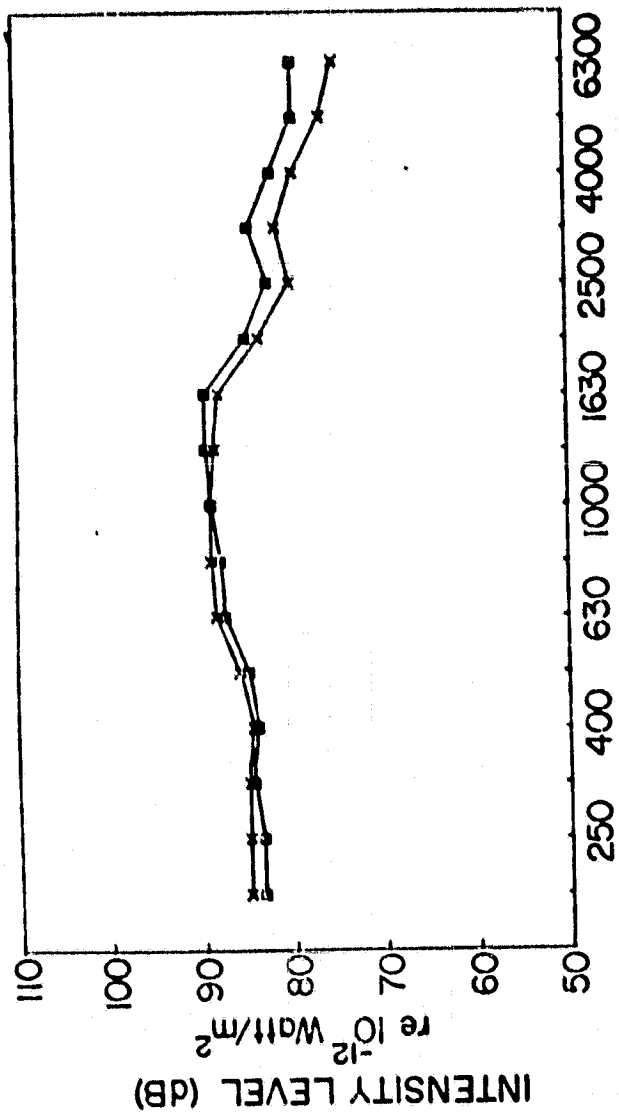

Figure 2.5 Comparison of diffuse field intensities.

□-□-□-□-□- Diffuse field intensity obtained from $p^2_{rms}/4\rho c$;

x-x-x-x-x-x-x-x-x By acoustic intensity measurement in an open "window."

due to the fact that $k\Delta r \ll 1$ is no longer satisfied. Because of this, the pressure gradient is not accurately determined by the centered finite difference approximation (Equation 12).

2.7.1 Measurement of Transmission Loss

Two different panel structures were selected for the transmission loss measurements. The first structure was a clamped steel panel of dimensions 121 cm x 121 cm x 1.6 mm. The area of the panel on which the sweeping was done, ie. the area facing the outside of the reverberation room excluding the part covered by the wooden frame was for the steel panel and all the other panels was 113 cm x 113 cm. The second structure was an aluminum panel with a thickness of 3.2 mm. The panels were clamped in a window of the reverberation room. The room volume was 212 cu.m. The sound pressure signal from the microphone on a rotating boom inside the reverberation room was used to determine the incident intensity. The transmitted intensity was obtained by sweeping the microphones on the outside of the panel. The result in one third octave bands is shown in Figures 2.6 and 2.7.

The transmission loss of a composite panel with the same inside dimensions and 3.2 mm thick was also measured. The composite panel consisted of an aluminum panel with a plexiglass window which covered about one ninth of the total panel area. The plexiglass window was concentric with this panel. The plexiglass thickness was about 1.6 mm. The result from the measurement of

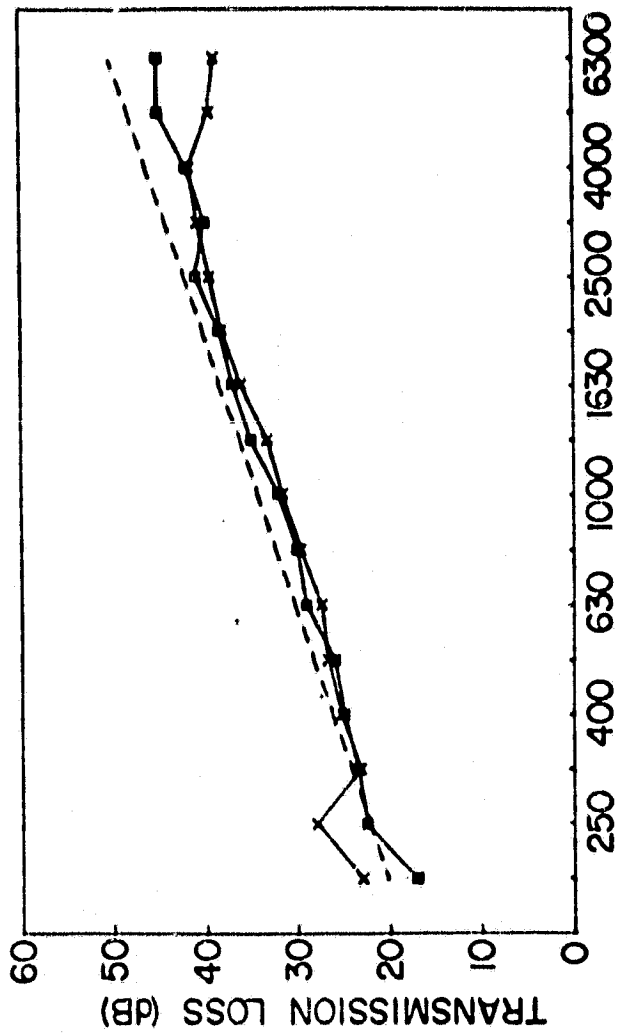

Figure 2.6 Transmission loss measurements on a steel panel (1.6 mm thick).

□-□-□-□-□- By acoustic intensity method;

-x-x-x-x-x-x-x- Conventional method;

---------- Mass law.

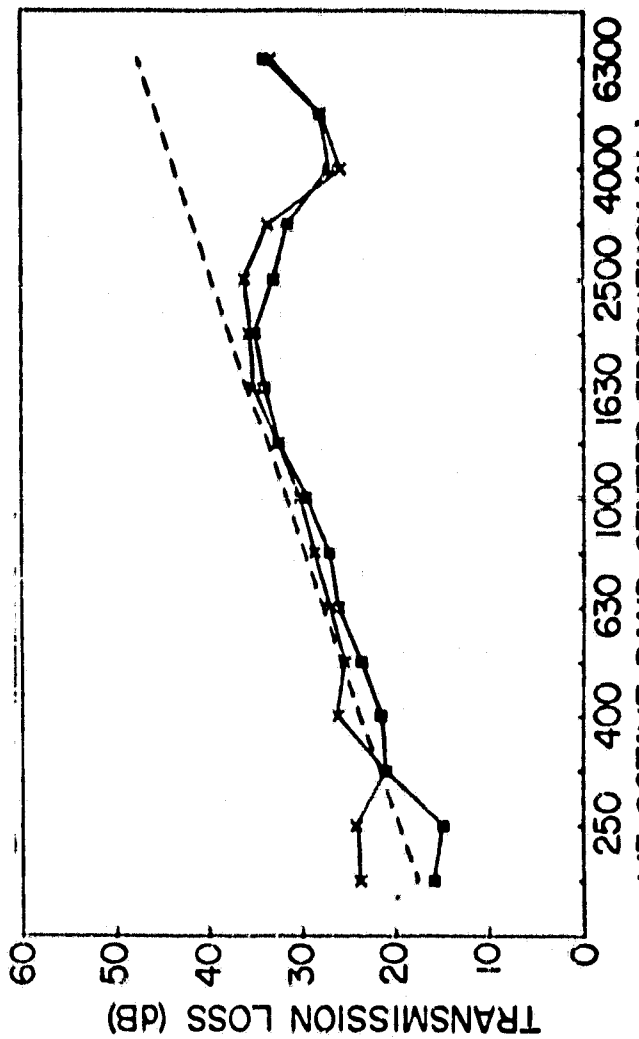

Figure 2.7 Transmission loss measurements on an aluminum panel (3.2 mm thick).

□-□-□-□-□- Ey acoustic intensity method;

-x-x-x-x-x-x-x- Conventional method;

---------- Mass law.

the transmission loss of the two different materials of the composite panel is shown in Figure 2.8. Also in the same figure are shown the predicted values as obtained from Equation (4). It is clear that this method is, able to identify the power transmitted through different areas of a complex structure.

2.7.2 Results and Conclusions

The results obtained by using the acoustic intensity technique agrees well with the transmission loss measurements made by the conventional transmission suite method as seen in Figures 2.6 through 2.8.

There are several advantages with this new method Firstly, it only requires one reverberant room. This means that the cost in building facilities for measuring transmission loss can be cut substantially. This also means that for already existing facilities with only one reverberation room there is now a method available for measuring the transmission loss. Secondly, it seems quite possible, with this method, to identify paths of power flow through structures. The conventional method does not have this possibility. When the measured values of transmission loss (by this new method) of the plexiglass and the aluminum parts of the compostie panel were substituted into Equations (4) and (5) the resulting total transmission loss agreed fairly well with the total transmission loss obtained by measurements made over the whole area of the composite panel.

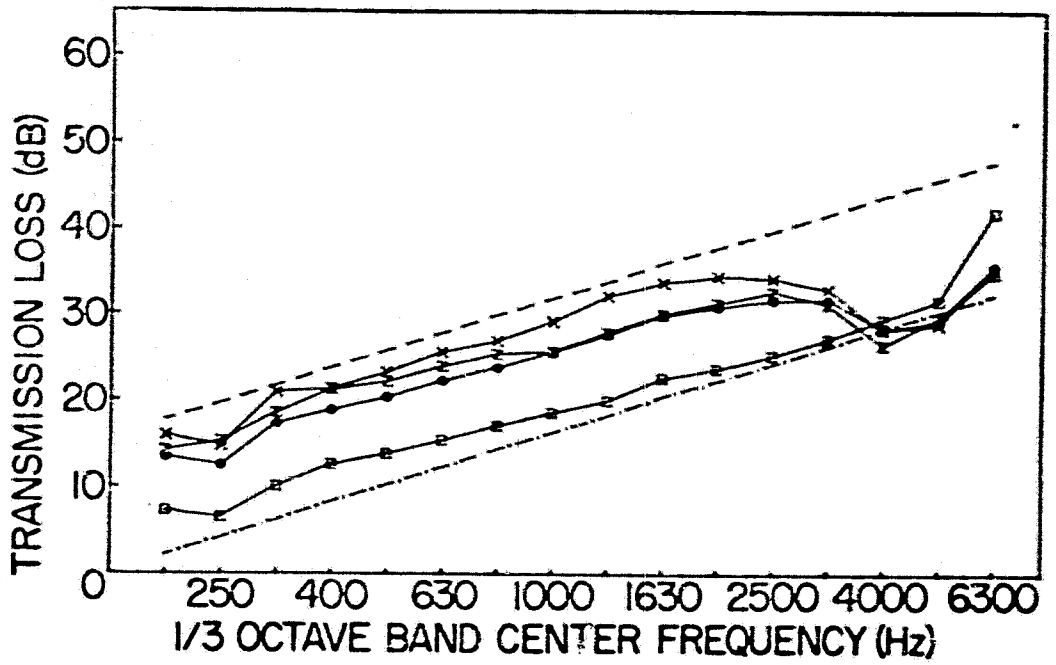

Figure 2.8 Measured and calculated transmission loss of a composite aluminum-plexiglass panel.

-x-x-x- Aluminum 3.2 mm thick;

-[]-[]- Plexiglass 1.6 mm thick;

-z-z-z- Total TL measured;

-*-*-*- Total TL theory;

------- Mass law aluminum;

-.-.-.- Mass law plexiglass.

One of the problems associated with this method is the frequency limit set by the microphone spacing. This could be overcome by reducing the spacing to obtain intensity values in higher frequency ranges or increase the spacing of microphones to obtain data in lower frequency range.

3. EXPERIMENTAL AND THEORETICAL STUDIES OF THE SOUND TRANSMISSION THROUGH SINGLE, COMPOSITE AND STIFFENED PANELS

3.1 Introduction

After the two microphone intensity technique had proved to be successful in measuring the transmission loss of a homogeneous single panel, it was decided that the same method should be applied to more complicated structures such as a composite panel consisting of a metal panel with a plexiglass window and a panel with stiffeners. The latter structures are more similar to those of a typical small aircraft fuselage than the homogeneous single panels studied earlier. It was also decided that the measured values should be compared with those obtained theoretically. The theoretical model was based on the principles of Statistical Energy Analysis (SEA).

3.2 Experimental Work

The instrumentation and the procedure used were quite similar to those outlined in Section 2. However there were some

differences.

A powerful driver shown in Fig. 3.1 was used instead of a loudspeaker. The sound sources shown in Figure 3.1 and 3.2 were run simultaneously. A typical sound source spectrum and level measured in the reverberation room are shown in Figure 3.7. The overall sound pressure level was about 133 dB. For the composite panel, to obtain the acoustic intensity transmitted microphone sweeping was performed with a distance of about 20 mm from the midpoint between the microphones to the panel (see Fig. 3.3 and 3.4). The clamped stiffened panel is shown in figures 3.5 and 3.6. The sweeping was done (see Figure 3.6) over a grid composed of very thin threads. The grid was used to assure uniformity in sweeping from the structure. However, in this procedure the sweeping was performed at a distance equal to the beam width plus about 10 mm, (between the microphone mid-point and the beams,) as shown in the figure below.

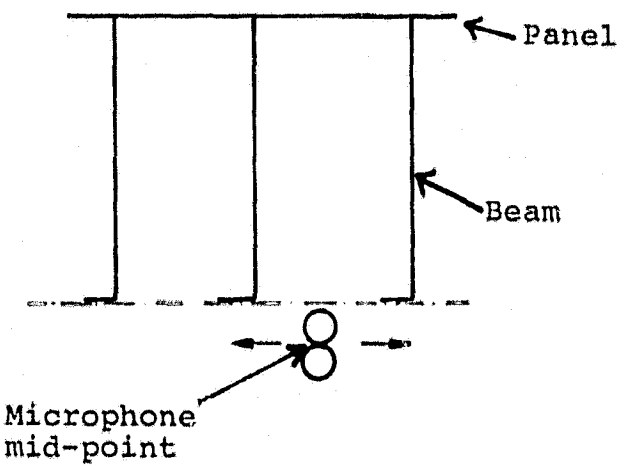

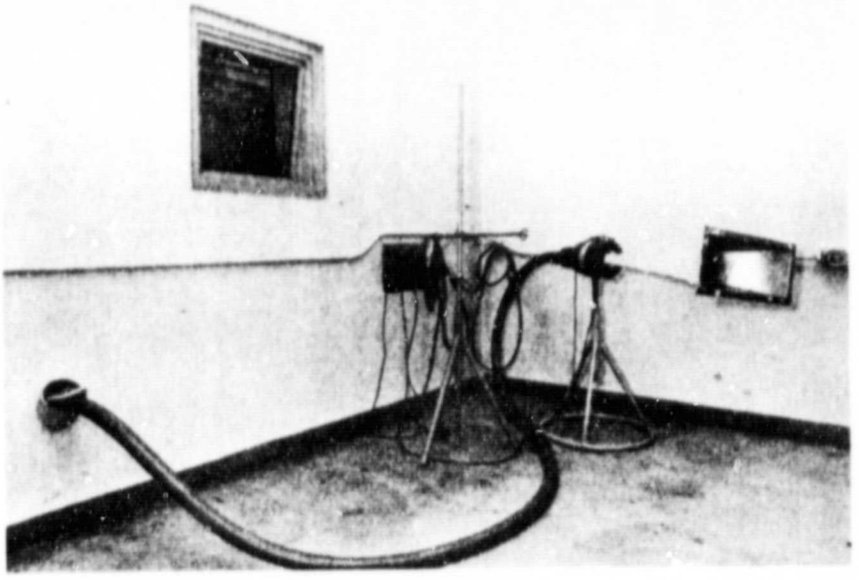

Figure 3.1 Pneumatic driver and jet noise source

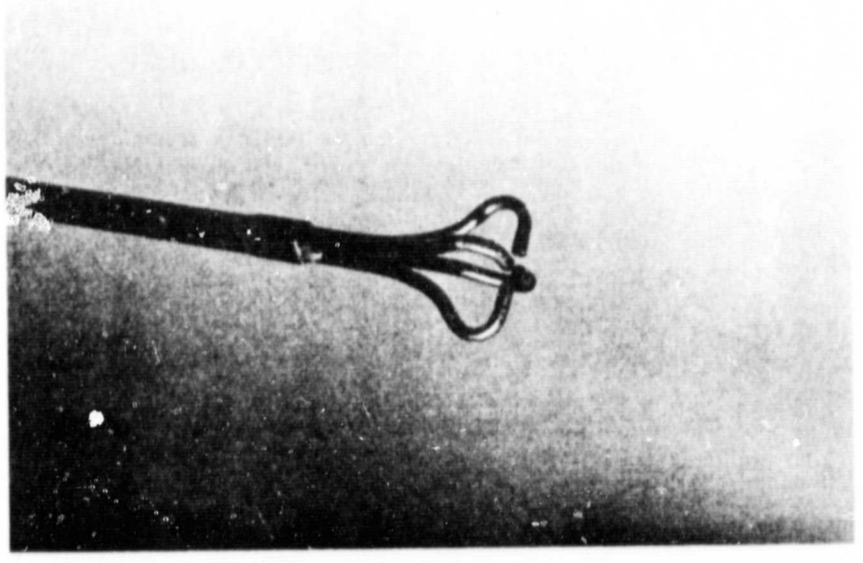

Figure 3.2 Jet noise source

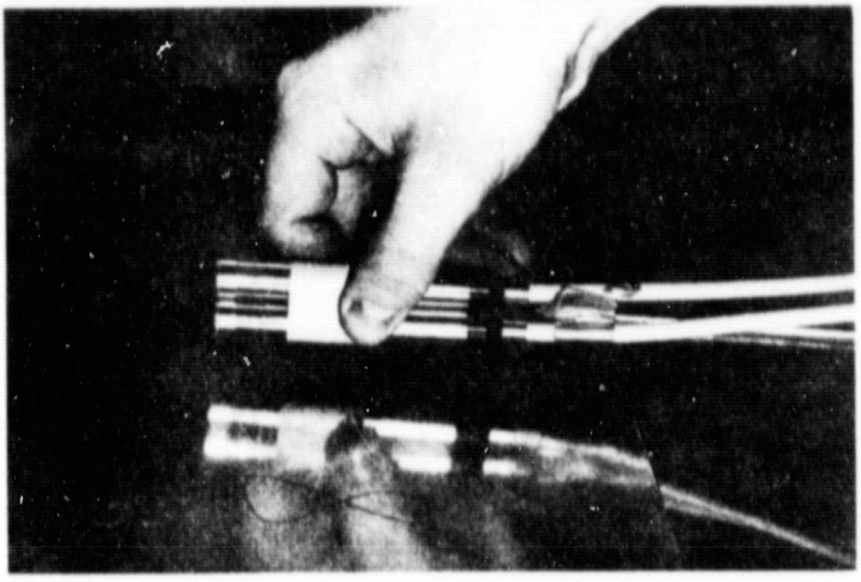

Figure 3.4 Photograph illustrating the microphone position relative to the panel.

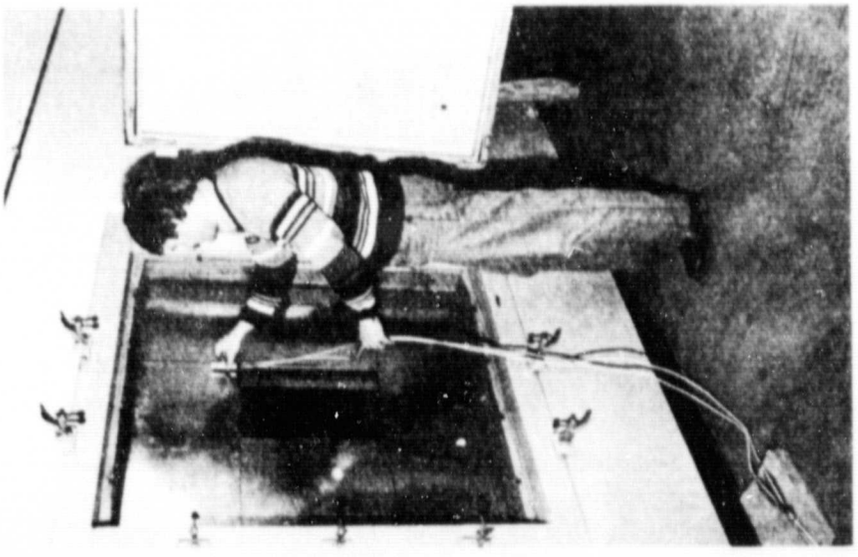

Figure 3.3 Photograph showing the sweeping over the composite panel with the two microphone array.

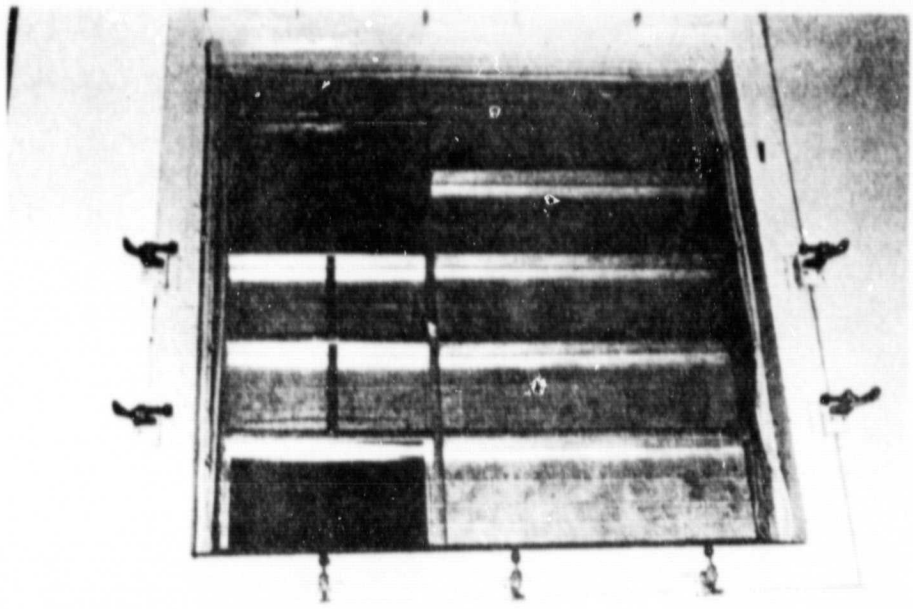

Figure 3.6 The stiffened panel as seen from outside the reverberation room.

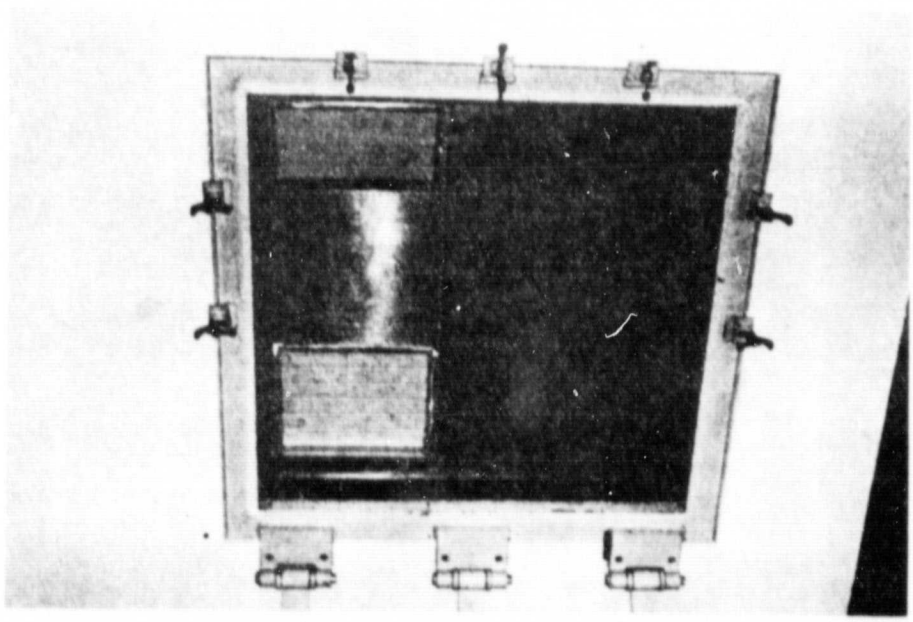

Figure 3.5 The stiffened panel as seen from inside the reverberation room.

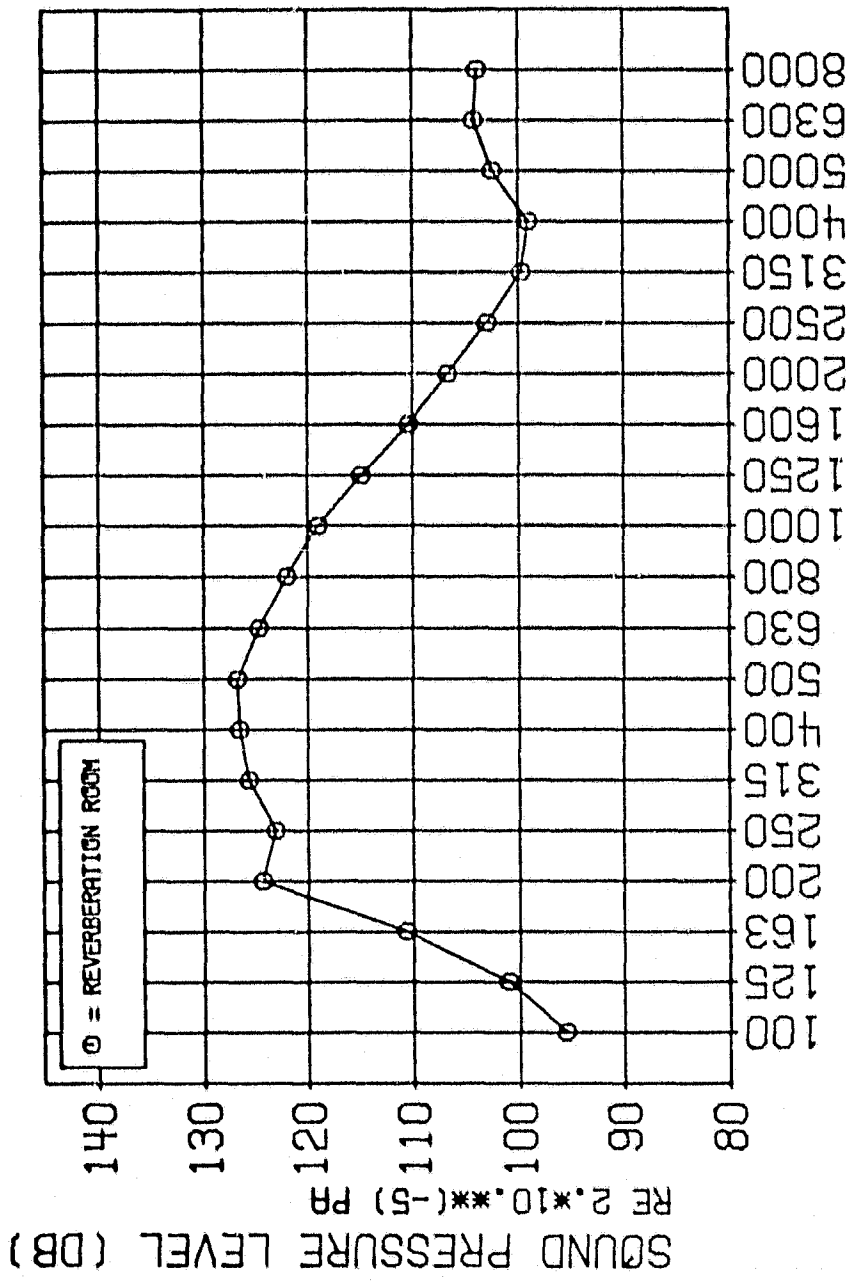

Figure 3.7 Typical sound pressure level spectrum inside the reverberation room due to the pneumatic driver (20 psia/6.0V) and the jet noise (80 psia).

The reason for this was that if the sweeping was done closer to the structure, the effects of standing waves in between the beams and scatter from the beams may affect the measurements.

3.3 SEA Modelling of the Panels

3.3.1 Derivation of the Transmission Loss

Consider the composite panel clamped in the window of the reverberation room. In this case the composite panel consists of two sub panels namely the plexiglass window and the aluminum panel. The diffuse field in the reverberation room is meant here to model the exterior noise field of a fuselage, and the panel a possible substructure. Before applying the statistical energy analysis to the following problem, it should be said that this theory is based on the fact that in each bandwidth of interest in each subsystem there must be enough resonant modes present to make the concept statistically meaningful. Following references 27 and 32 it seems logical to divide the problem into three sub-structures:

1. The reverberation room,
2. The plexiglass window and
3. The aluminum panel,

as shown in Figure 3.8. Conservation of energy in each subsystem requires that

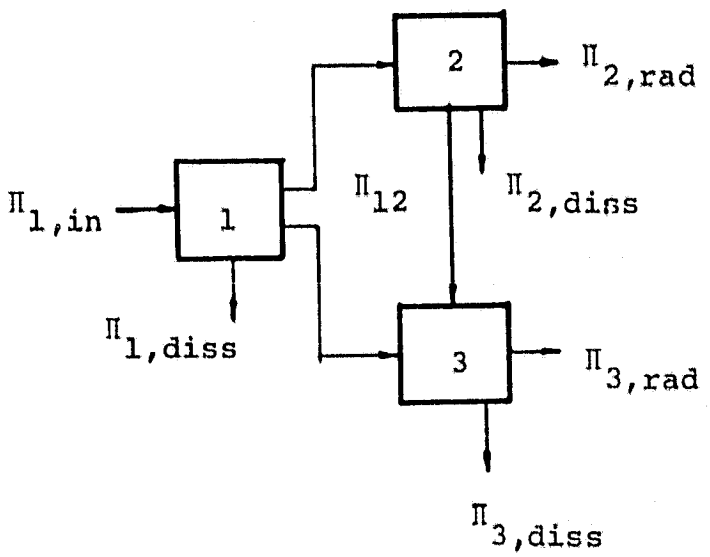

Figure 3.8 Block diagram representing power flow between three coupled systems of the composite panel.

$$\Pi_{i,in} = \Pi_{i,diss} + \sum_{j=i}^{N_i,} \Pi_{ij} \qquad (3.1)$$

where the prime on the sum means that j=i is excluded; further the power flows in equation (1) are as follows:

$\Pi_{i,in}$ = input power the ith subsystem, and

$$\Pi_{i,diss} = \omega \eta_i E_{i,tot} \qquad (3.2)$$

is the dissipated power of the ith subsystem, where η_i is the internal loss factor and $E_{i,tot}$ is the total energy, and finally

$$\Pi_{ij} = \omega \Pi_{ij} E_i - \omega \Pi_{ji} E_j \qquad (3.3)$$

is the power flow between subsystem i and j, η_{ij} is the coupling loss factor.

The number of resonant modes N_i, N_j in a bandwidth of Δf in subsystems i and j and the coupling loss factors η_{ij} and η_{ji} must satisfy the consistency relationship:

$$N_i \eta_{ij} = N_j \eta_{ji} \qquad (3.4)$$

Using equations (3.1),(3.2),(3.3), and (3.4), the power balance equations of the three system model become:

$$\begin{aligned} \Pi_{1,in} &= \Pi_{1,diss} + \Pi_{12} + \Pi_{13} + \Pi_{nonres} \qquad (3.5) \\ 0 &= \Pi_{2,diss} - \Pi_{12} + \Pi_{23} + \Pi_{2,rad} \\ 0 &= \Pi_{3,diss} - \Pi_{13} - \Pi_{23} + \Pi_{3,rad} \end{aligned}$$

where τ_{nonres} stands for the non-resonant power flow and and $\Pi_{3,rad}$ represents here the power radiated to an infinite half space. The non-resonant power flow is given by

$$\Pi_{nonres} = \tau_{nonres}\, \Pi_{inc} \tag{3.6}$$

where τ_{nonres} is the non-resonant transmission coefficient and Π_{inc} is the incident sound sound power on the side of the panel facing the reverberation room. Now it holds that

$$\Pi_{nonres} = \tau_{nonres}\, \Pi_{inc} = \tau_{nonres}\, A_p \frac{\langle p_{rms}^2 \rangle_t}{4\rho C} = \tag{3.7}$$

$$= \tau_{nonres}\, \frac{A_p C}{4V} \left[\frac{\langle p_{rms}^2 \rangle_t}{\rho C^2}\, V \right] = \tau_{nonres}\, \frac{A_p C}{4V}\, E_1$$

where $\langle p_2 \rangle_t$ is the space time averaged sound pressure, A_p is the panel area, ρ is the density of the ambient medium, C is the speed of sound and V is the volume of the room. With this in mind, equations (3.5) can be written as:

(3.8)

$$\frac{\Pi_{1,in}}{\omega} = \eta_1 E_1 + \eta_{12} n_1 \left[\frac{E_1}{n_1} - \frac{E_2}{n_2} \right] + \eta_{13} n_1 \left[\frac{E_1}{n_1} - \frac{E_3}{n_3} \right] + A_p\, \frac{C E_1}{4V\omega}\, \tau_{nonres}$$

$$0 = \eta_2 E_2 - \eta_{12} n_1 \left[\frac{E_1}{n_1} - \frac{E_2}{n_2} \right] + \eta_{23} n_2 \left[\frac{E_2}{n_2} - \frac{E_3}{n_3} \right] + \eta_{rad,2} E_2$$

$$0 = \eta_3 E_3 - \eta_{13} n_1 \left[\frac{E_1}{n_1} - \frac{E_3}{n_3} \right] - \eta_{23} n_2 \left[\frac{E_2}{n_2} - \frac{E_3}{n_3} \right] + \eta_{rad,3} E_3$$

or in matrix form as:

(3.9)

$$\begin{bmatrix} \eta_1 + \eta_{12} + \eta_{13} + \frac{A_p}{4\omega v} C\,\tau_{nonres} & -\eta_{21} & -\eta_{31} \\ -\eta_{12} & (\eta_2 + \eta_{21} + \eta_{23} + \eta_{rad,2}) & -\eta_{32} \\ -\eta_{13} & -\eta_{23} & (\eta_3 + \eta_{31} + \eta_{32} + \eta_{rad,3}) \end{bmatrix} \begin{bmatrix} E_1 \\ E_2 \\ E_3 \end{bmatrix} = \begin{bmatrix} \frac{\Pi_{1,in}}{\omega} \\ 0 \\ 0 \end{bmatrix}$$

The non-resonant transmission coefficient τ_{nonres}, of each sub area is found by using the mass law [33]

$$10 \log\left[\frac{1}{\tau_{i,nonres}}\right] = 10 \log\left[\frac{\pi m' f}{\rho C}\right]^2 - 10 \log\left\{0.23\left[10 \log\left[1 + \left(\frac{\pi m' f}{\rho C}\right)^2\right]\right]\right\} \quad (3.10)$$

then an average transmission coefficient is given by

$$\tau_{nonres} = \bar{\tau} = \frac{\tau_1 A_1 + \tau_2 A_2}{A_p} \quad (3.11)$$

where A_1 are subareas and A_p is the total panel area. The transmission loss is defined as

$$TL = 10 \log\left[\frac{\Pi_{inc}}{\Pi_{rad} + \Pi_{nonres}}\right] \quad (3.12)$$

for the composite panel this becomes

$$TL_C = 10 \log\left[\frac{\Pi_{inc}}{\Pi_{2,rad} + \Pi_{3,rad} + \Pi_{nonres}}\right] \qquad (3.13)$$

The radiated power is [27]

$$\Pi_{i,rad} = \frac{R_{i,rad}^{2\pi}}{M_{p_i}} E_i \qquad (3.14)$$

where for ith subpanel area, M_{p_i} is the mass of the panel, $R_{i,rad}^{2\pi}$ is the radiation resistance to half space. The derivation of $R_{i,rad}^{2\pi}$ is given in [34]. The corrected equation is given in [33]. Substituting equation (12) for i=1,2, and Equation (7) into Equation (11) gives:

$$TL = 10 \log\left[\frac{\frac{A_p C}{4V} E_1}{\frac{R_{2,rad}^{2\pi}}{M_{p_2}} E_2 + \frac{R_{3,rad}^{2\pi}}{M_{p_3}} E_3 + \frac{A_p}{4V} \tau_{nonres} E_1}\right] \qquad (3.15)$$

rearranging this equation gives the final expression for the transmission loss as

$$TL = 10 \log\left[\frac{1}{\tau_{nonres} + \frac{4V}{A_p c}\left\{\frac{R_{2,rad}^{2\pi}}{M_{p_2}} \frac{E_2}{E_1} + \frac{R_{3,rad}^{2\pi}}{M_{p_3}} \frac{E_3}{E_1}\right\}}\right] \qquad (3.16)$$

The ratios of the total energies $E_1, E_2,$ and E_3 are determined

from Equation (8). This Equation shows that for the case of a single panel Equation (14) reduces to

$$TL = 10 \log \left[\frac{1}{\tau_{nonres} + \frac{4V}{A_p C} \frac{R_{rad}^{2\pi}}{M_p} \frac{E_2}{E_1}} \right] \qquad (3.17)$$

Two computer programs have been written to solve for the transmission loss given by Equations (14) and (15). A reduction scheme [37] was written to solve the set of linear equations.

In order to solve for the energies in Equation (8), the loss factors would have to be known either through measurement or based on empirical data. The following section discusses these parameters and how they were obtained, for the particular set-up.

3.3.2 Loss Factors

The loss factors are the internal loss factor, coupling loss factor and radiation loss factor. The internal loss factor of the reverberation room is related to the reverberation time by:

$$\eta = \frac{2.2}{fT} \qquad (3.18)$$

where T is the reverberation time, and f is the center frequency.

An automated program developed by Bruel and Kjaer [36] was used, to measure the decay of the sound pressure level in the room and to calculate the reverberation time. The triggering of

the noise source was controlled by the program through the interface between the source and a HP 9825A desk top calculator. The levels were calculated from a real-time analyzer BK 2131 and the data was then transferred to the calculator. (See figure 3.9.) The rotating boom had a speed of about 1 revolution per 16 seconds. Four recordings, each based on 65 spectra spaced 88 ms apart were taken to cover one revolution.

The internal loss factors of the single panel were obtained by using a program developed by Simon Wang (details are given in Part II of this report). The panel, mounted in the window to assure the same boundary conditions as those present in the measurement of the transmission loss was excited by a shaker. Five accelerometer positions were used to record the decay of the signal. For each accelerometer position, five decay curves were taken in each one-third octave band. The set-up and the results for the aluminum panel are shown in figures 3.10 and 3.11. As seen from figure 3.11, the internal loss factor is much higher at the critical coincidence frequency (3987 Hz). The reason is that the above program gives the sum of the radiation loss factor and internal loss factor. Other investigators [27,37] have shown that it is probably only near the critical coincidence frequency that the radiation loss factor may exceed the internal loss factor.

It is planned to measure the internal loss factors for the other panels later this spring. The radiation loss factor is obtained from theory [27].

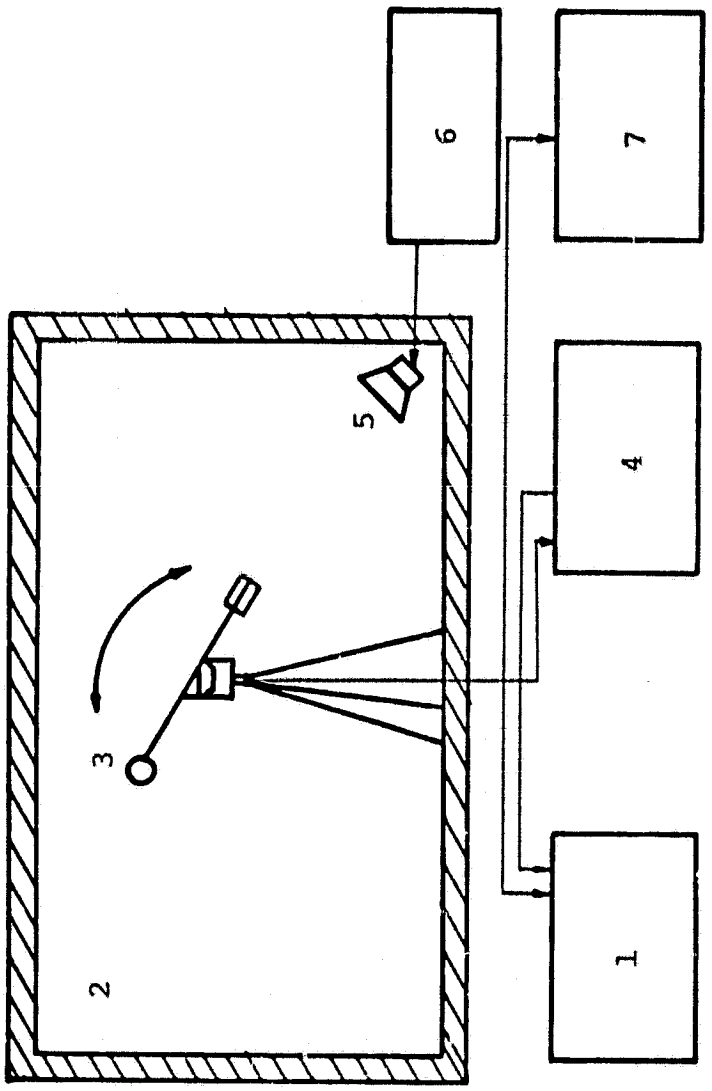

Figure 3.9 Schematic diagram of the instrumentation used for the measurement of the reverberation time in a room

1. HP9825A (minicomputer)
2. Rev. Room
3. Rotating Box
4. BK2131 Real Time Analyzer
5. Loudspeaker
6. Amplifier
7. Random Noise Generator

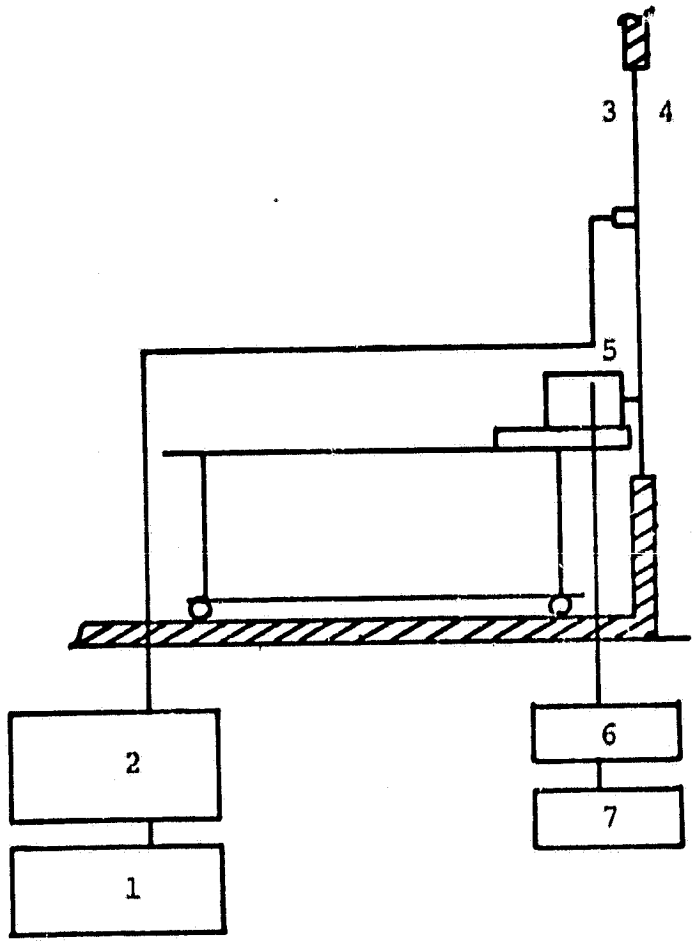

Fig. 3.10 Experimental setup for the measurement of the the loss factor of the panel

1. HP5451C (FFT)
2. Charge Amplifier
3. Accelerometer
4. Panel
5. Shaker
6. Amplifier
7. Random Noise Generator

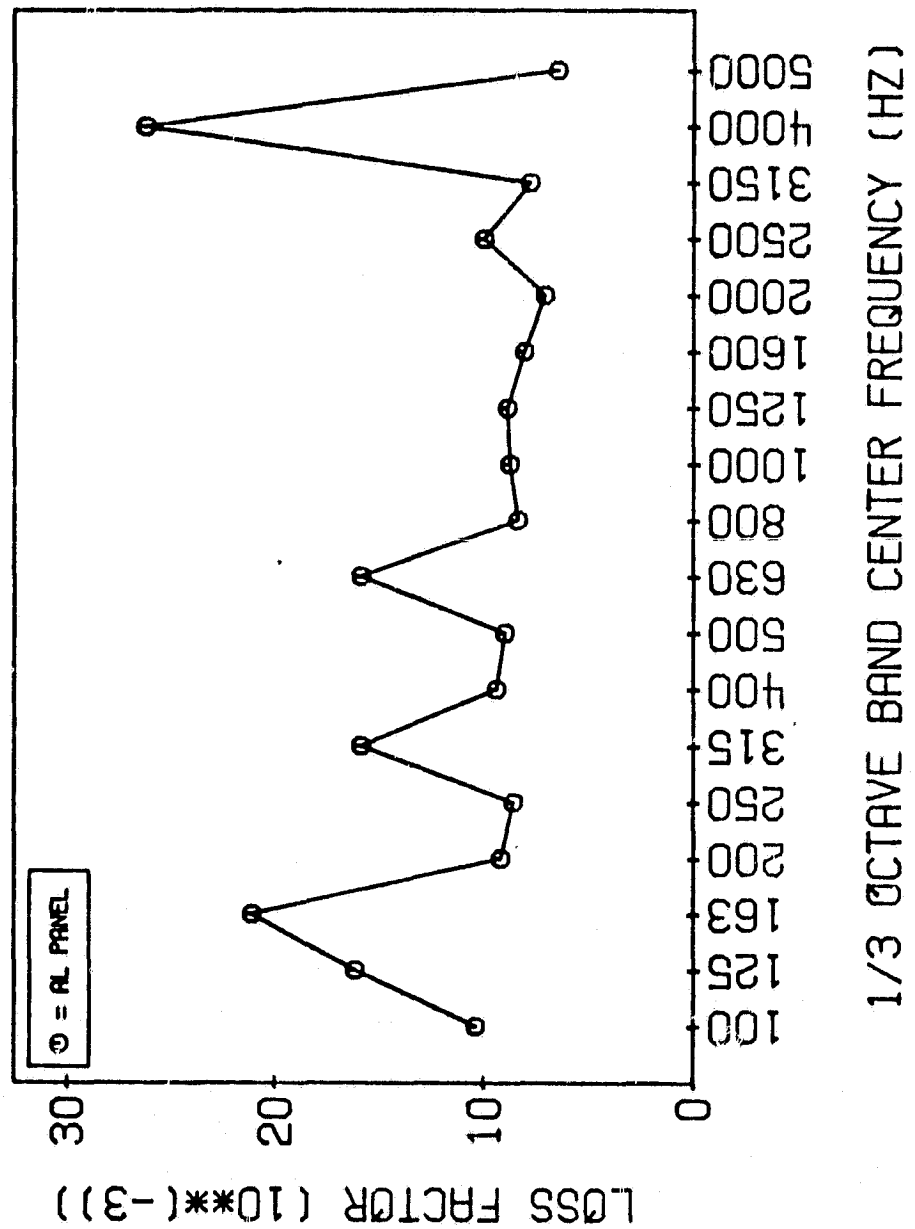

Figure 3.11 Total loss factor of the aluminum panel

The coupling loss factor between the plexiglass and the aluminum panels has been derived. However the derivation is similar to the given in reference [38]. The derivation is lengthy and will not be presented here.

3.3.3 The Single Panel

It can be seen from Figure 3.12 that the SEA-model predicts the transmission loss fairly well for frequencies up to the coincidence dip. The disagreement above the critical coincidence frequency might be partially explained by the fact that the microphone spacing (14 mm) no longer satisfies the condition that $k\Delta r \ll 1$. However, other experiments which show the effect of the spacing on intensity measurements show in contrast that this error should be small. Another more likely reason is that the panel is radiating less efficiently than that predicted by the theory. An average value of radiation loss in each one third octave band was taken while evaluating the transmission loss shown in the figure.

3.3.4 The Composite Panel

The narrow band values of the sound pressure levels and intensity levels are shown in figures 3.13 to 3.19. It can be seen in Figure 3.13 that the intensty level is fairly smooth up to about 5,800 Hz. The ripples above that frequency are due to the effect of crossmodes in the tube where the transfer function was measured. So, this effect is carried through the calculation to the final value of the imaginary part of the cross spectrum.

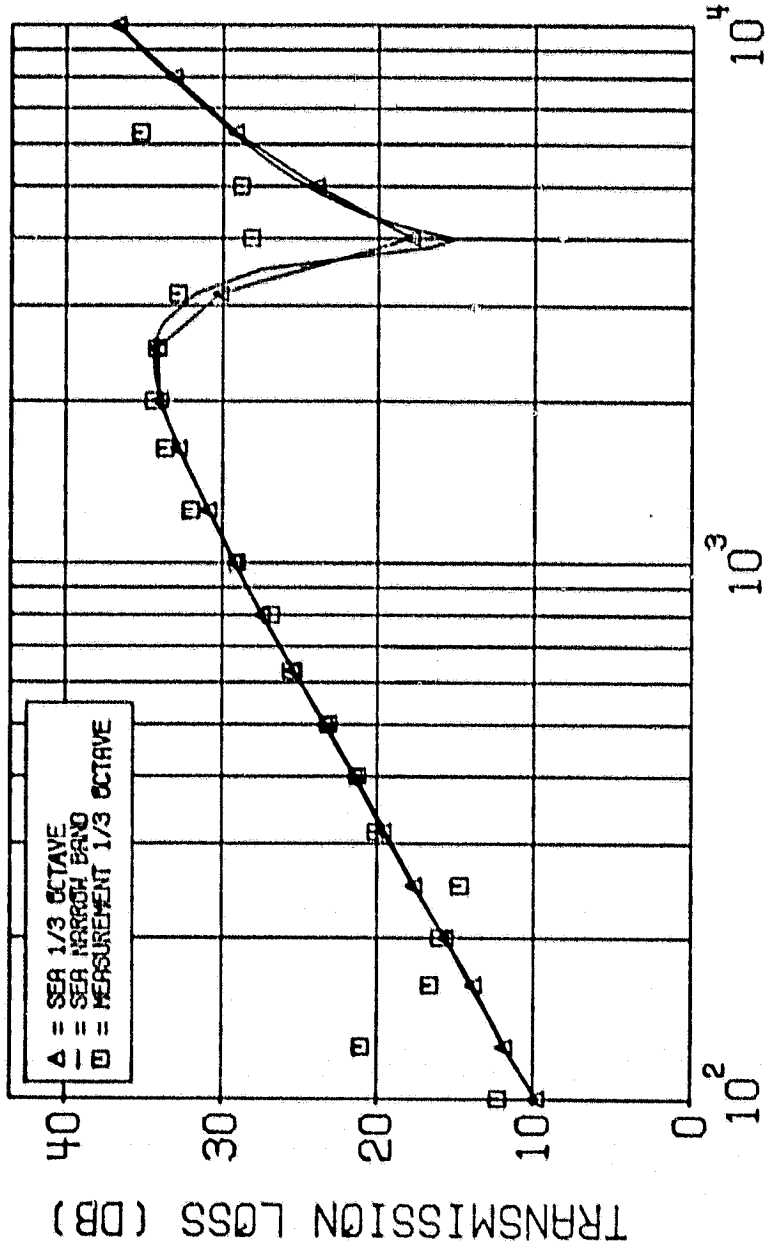

Figure 3.12 Comparison between measured and predicted values of transmission loss for the aluminum panel (1/8" thick).

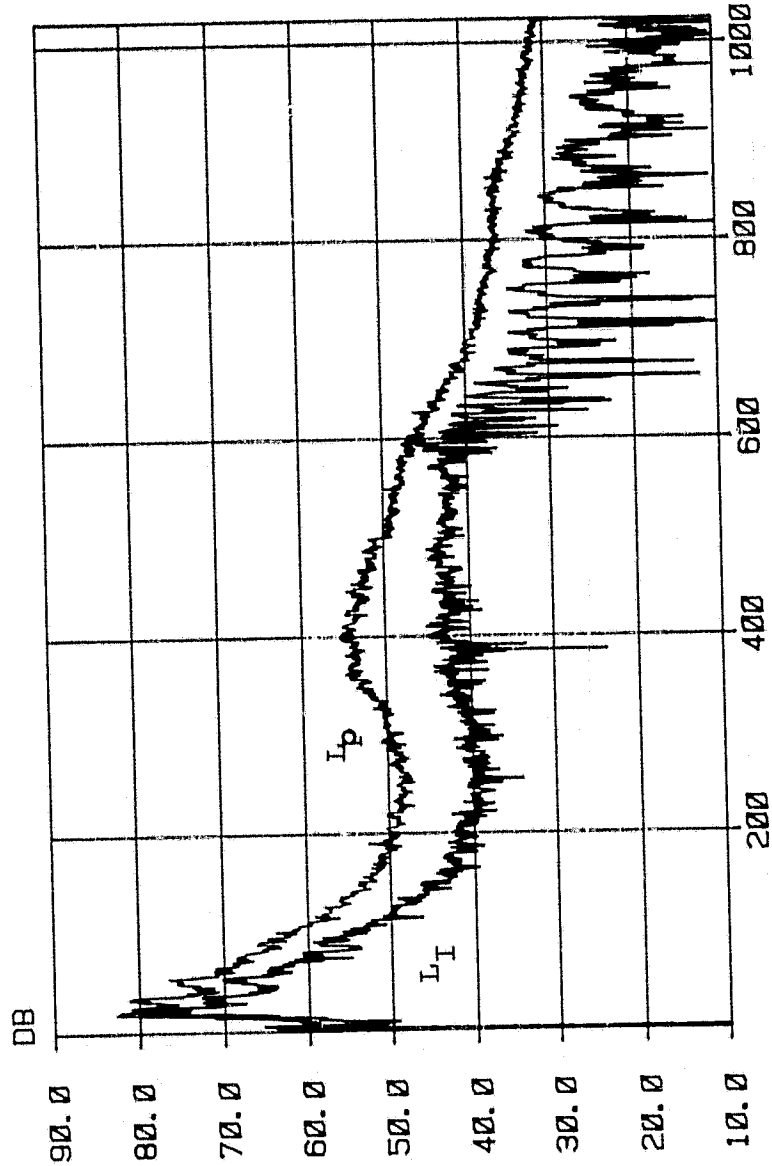

Figure 3.13 Sound pressure level, L_p, and intensity level, L_I, of the aluminum subarea of the composite panel presented over narrow frequency bands.

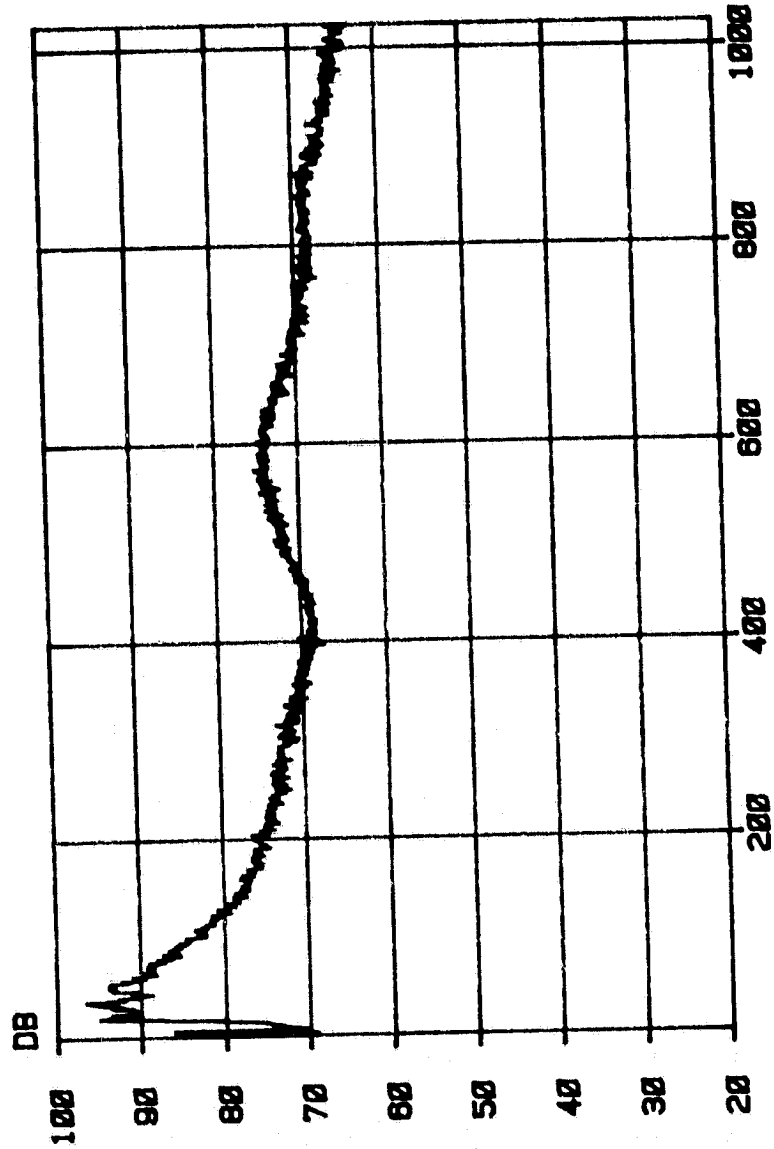

Figure 3.14 Intensity level of the whole composite panel presented over narrow frequency bands.

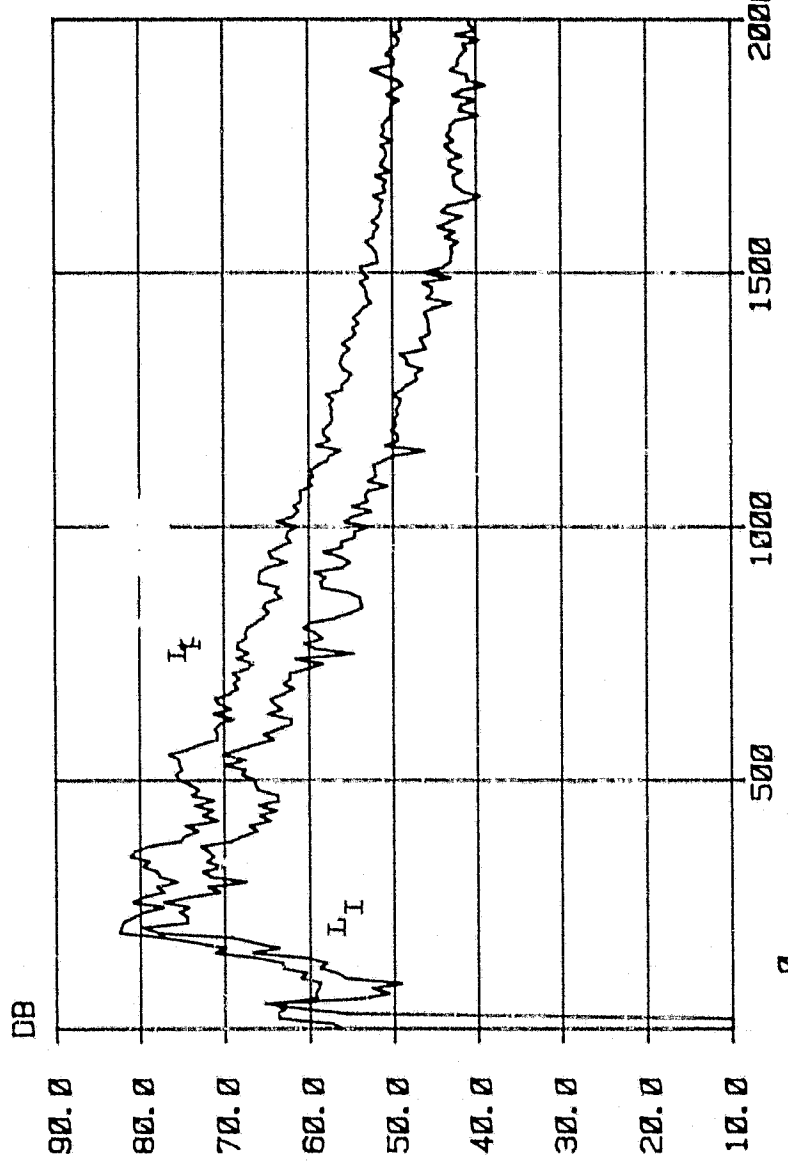

Figure 3.15 Sound pressure level, L_p, and intensity level, L_I, of the aluminum sub panel of the composite panel presented over narrow frequency bands and expanded in the frequency range 0 to 2000 Hz.

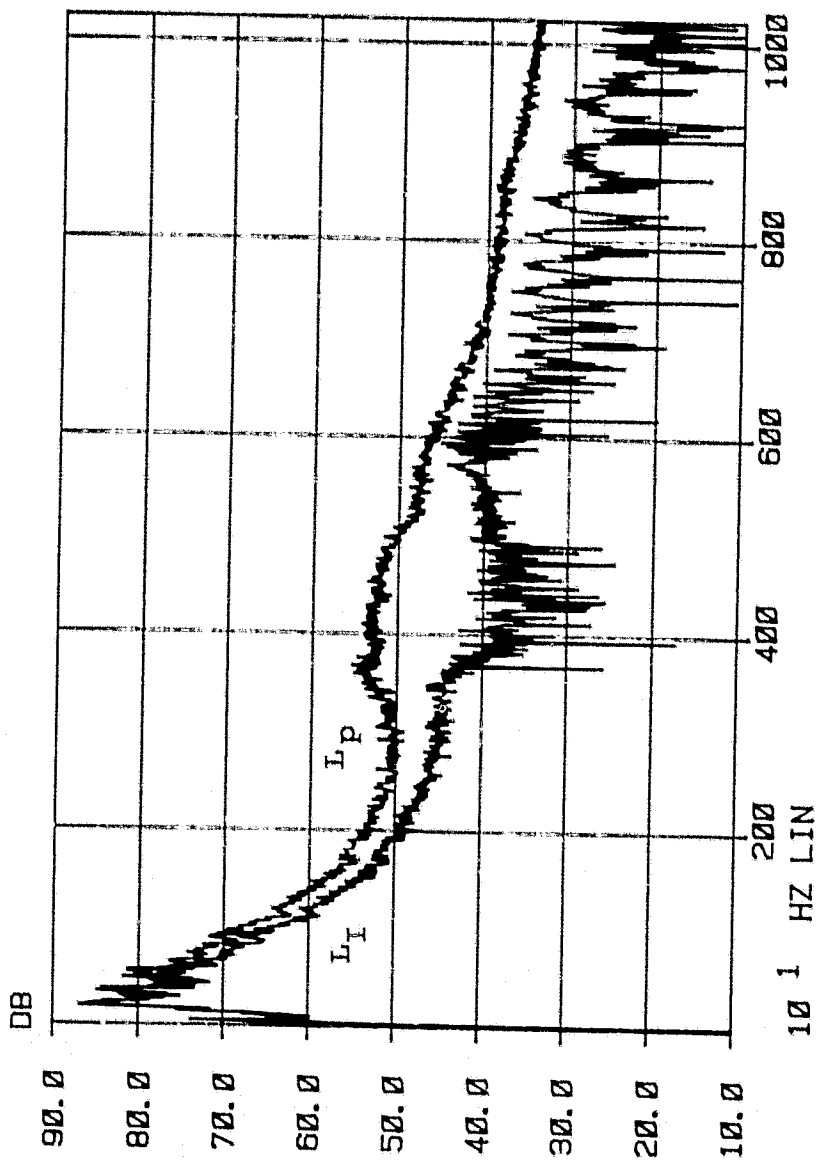

Figure 3.16 Sound pressure level, L_p, and intensity level, L_I, of the plexiglass window of the composite panel presented over narrow frequency bands; (note different frequency scale)

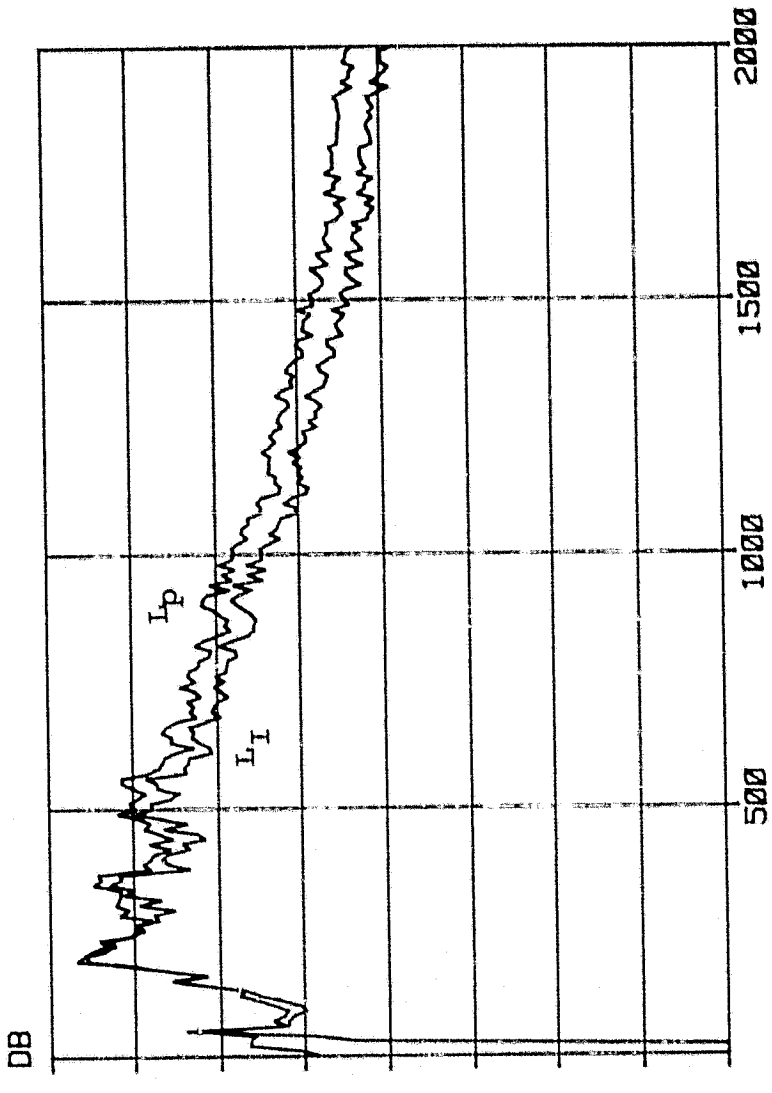

Figure 3.17 Sound pressure level, L_p, and intensity level, L_I, of the plexiglass window of the composite panel presented over narrow bands and expanded in the frequency range 0 to 2000 Hz.

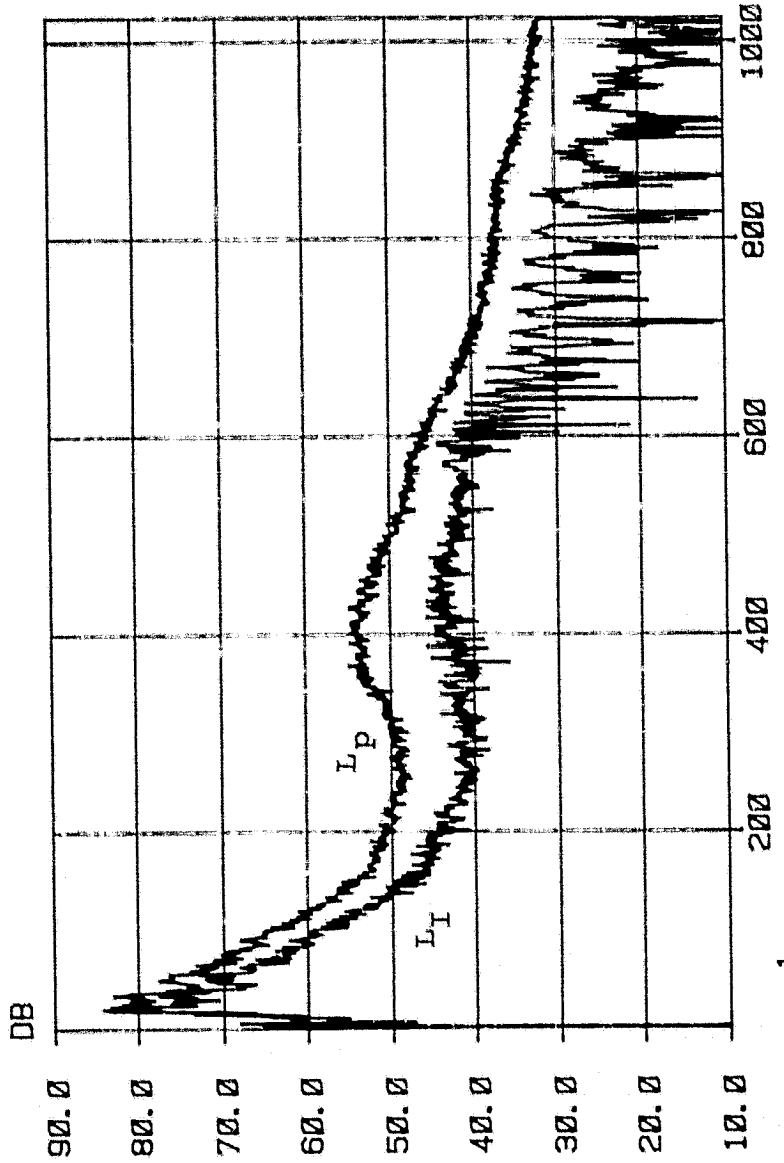

Figure 3.18 Sound pressure level, L_p, and intensity level, L_I, of the whole composite panel presented over narrow frequency bands; (note different frequency scale).

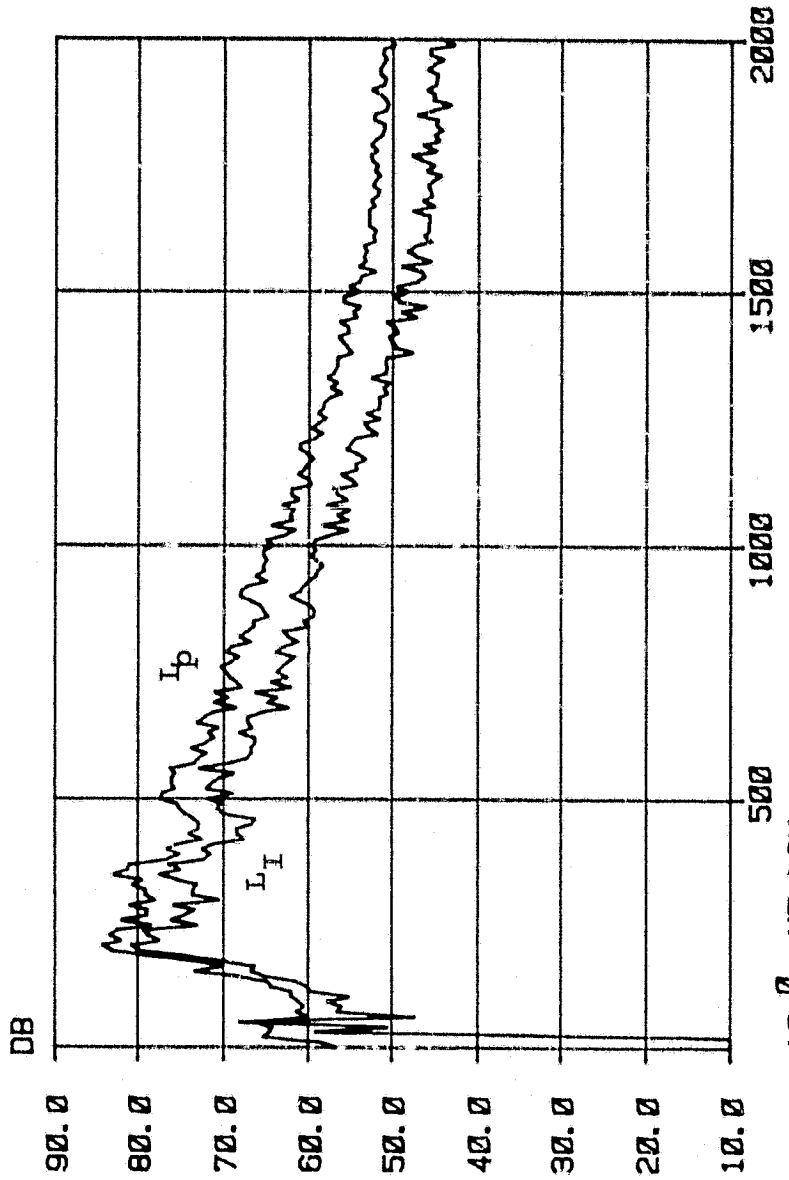

Figure 3.19 Sound pressure level, L_p, and intensity level, L_I, of the whole composite panel presented over narrow frequency bands and expanded in the frequency range 0 to 2000 Hz.

The intensity level has a minimum around 2000 Hz and increases up to about 5000 Hz. For the same frequencies, the intensity level, shown in Figure 3.14, inside the reverberation room drops up to about 4000 Hz, after which it recovers. This demonstrates experimentally the effect of the transmission loss dip at the critical coincidence frequency which for the aluminum panel is 3987 Hz. In figure 3.15 the intensity level and the sound pressure level are superimposed.

The intensity from the plexiglass area of the composite panel is shown in figures 3.16 and 3.17. For frequencies around 3500 Hz to 5500 Hz, it seems that less intensity, than might be expected, is emitted from the plexiglass area. A possible reason for this is that the aluminum panel area absorbs energy from the plexiglass area.

The intensity obtained for the whole area is presented in plots 3.18 to 3.19. The general trend as shown in Figure 3.18 seems to follow that of the aluminum sub panel area (see Figure 3.14).

The comparison between predicted and measured values is shown in Figure 3.20. There is fairly good agreement for frequencies between 163 Hz and about 4000 Hz. The reason for the discrepancy above the coincidence dip is possibly due to uncertainties in the estimates of the internal loss factor and radiation efficiency.

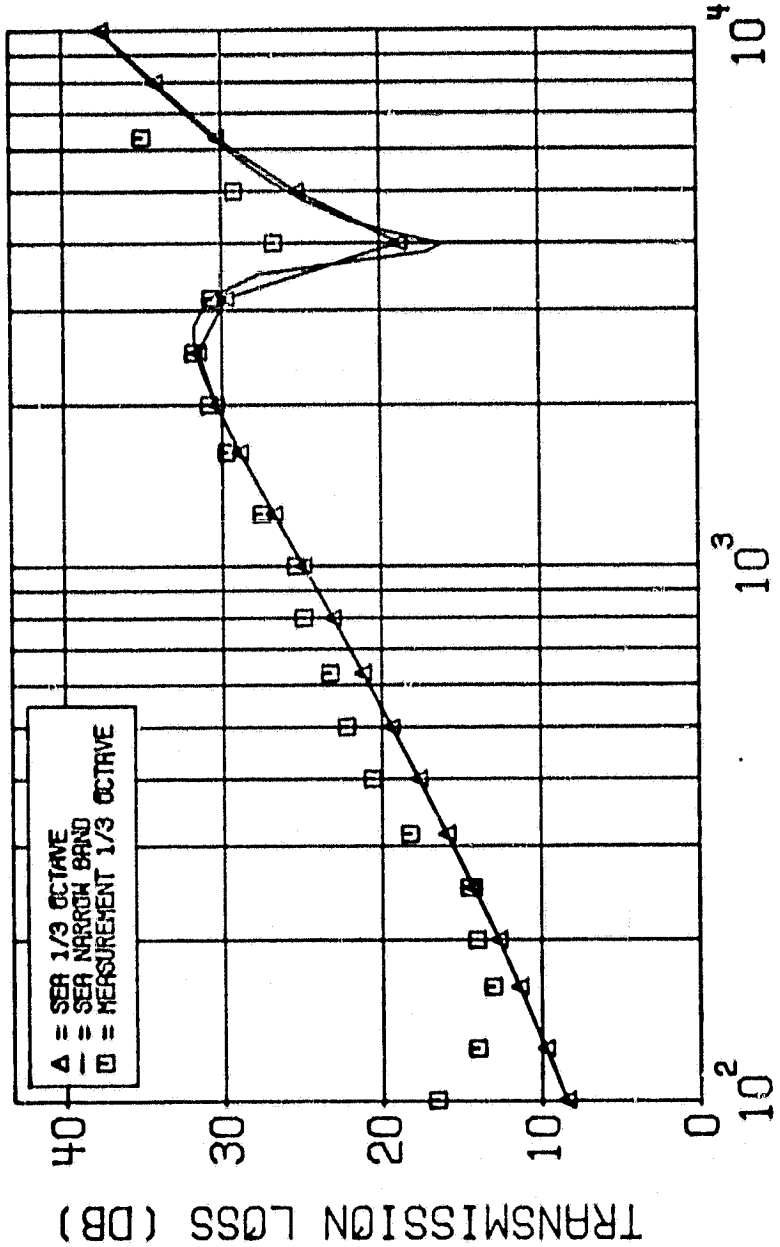

Figure 3.20 Comparison between measured and predicted values of transmission loss for the composite panel (for the internal loss factor of the plexiglass an empirical value of 0.1 was used).

3.3.5 The Stiffened Panel

It was decided that the first attempt to formulate the powerbalance equations should only consider the subareas shown in Figure 3.21. The power balance equation is shown in Figure 3.22. However, for the measurements the panel was divided into five subareas:

a) the small plexiglass window (1),

b) the area in between the windows (2),(3),(4), & (5),

c) the big plexiglass window (6),

d) the left stiffened bay (7),(8), and half of (9),

e) the right stiffened bay (10),(11), and half of (9),

where the bracketed numbers indicate corresponding areas in Figure 3.21. The narrow band values for the soundpressure and intensity levels between 0 and 2000 Hz for different subareas are shown in figures 3.23 to 3.26. Figures 3.27 to 3.31 show the consistency between the three measurements. If these graphs are overlayed, it can be seen that they are all quite close to each other above 2000 Hz. This suggests that there might be some contamination from neighboring areas. This might be due to measurements made with too big a distance between the microphones and the panel. Below 2000 Hz it seems that the stiffened areas give a higher transmission loss.

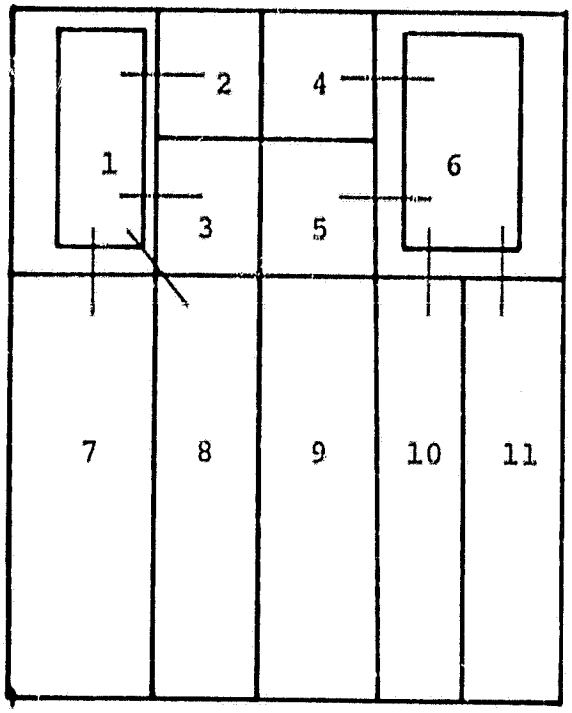

Figure 3.21 Labeling of subsystems on the stiffened panel and the power flow between them.

A_{11}	$-\eta_{12}$	$-\eta_{31}$				$-\eta_{71}$	$-\eta_{81}$				$-\eta_{12,1}$	E_1	0
$-\eta_{12}$	A_{22}										$-\eta_{12,2}$	E_2	0
		A_{33}									$-\eta_{12,3}$	E_3	0
			A_{44}		$-\eta_{6,4}$						$-\eta_{12,4}$	E_4	0
				A_{55}	$-\eta_{6,5}$						$-\eta_{12,5}$	E_5	0
			$-\eta_{4,6}$	$-\eta_{4,5}$	A_{66}				$-\eta_{10,6}$	$-\eta_{11,6}$	$-\eta_{12,6}$	E_6	0
$-\eta_{17}$						A_{77}					$-\eta_{12,7}$	E_7	0
$-\eta_{18}$							A_{88}				$-\eta_{12,8}$	E_8	0
								A_{99}			$-\eta_{12,9}$	E_9	0
					$-\eta_{6,10}$				A_{1010}		$-\eta_{12,10}$	E_{10}	0
					$-\eta_{6,11}$					A_{1111}	$-\eta_{12,11}$	E_{11}	0
$-\eta_{1,12}$	$-\eta_{2,12}$	$-\eta_{3,12}$	$-\eta_{4,12}$	$-\eta_{5,12}$	$-\eta_{6,12}$	$-\eta_{7,12}$	$-\eta_{8,12}$	$-\eta_{9,12}$	$-\eta_{10,12}$	$-\eta_{11,12}$	$A_{12,12}$	E_{12}	Π_{12}/ω

Figure 3.22 The power balance equation for the stiffened panel. (see appendix for the diagonal terms)

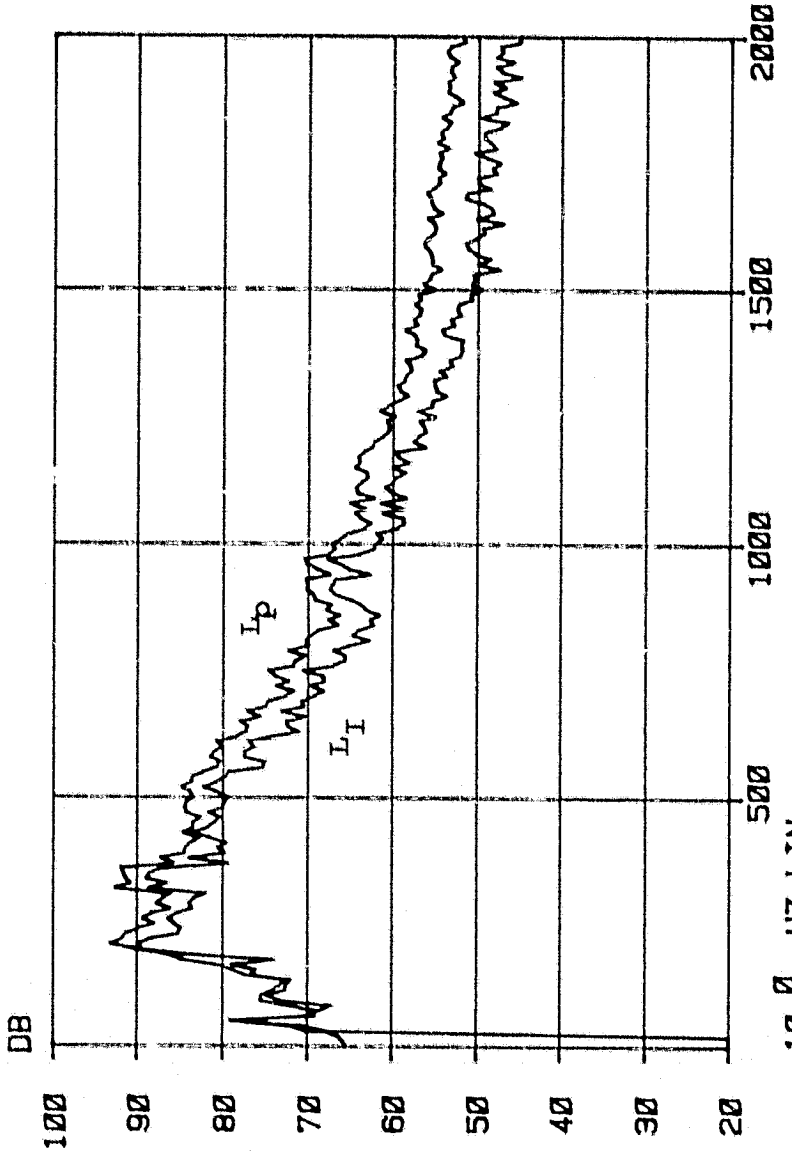

Figure 3.23 Sound pressure level, L_p, and intensity level, L_I, of the small plexiglass window presented over narrow frequency bands and expanded in the frequency range 0 to 2000 Hz.

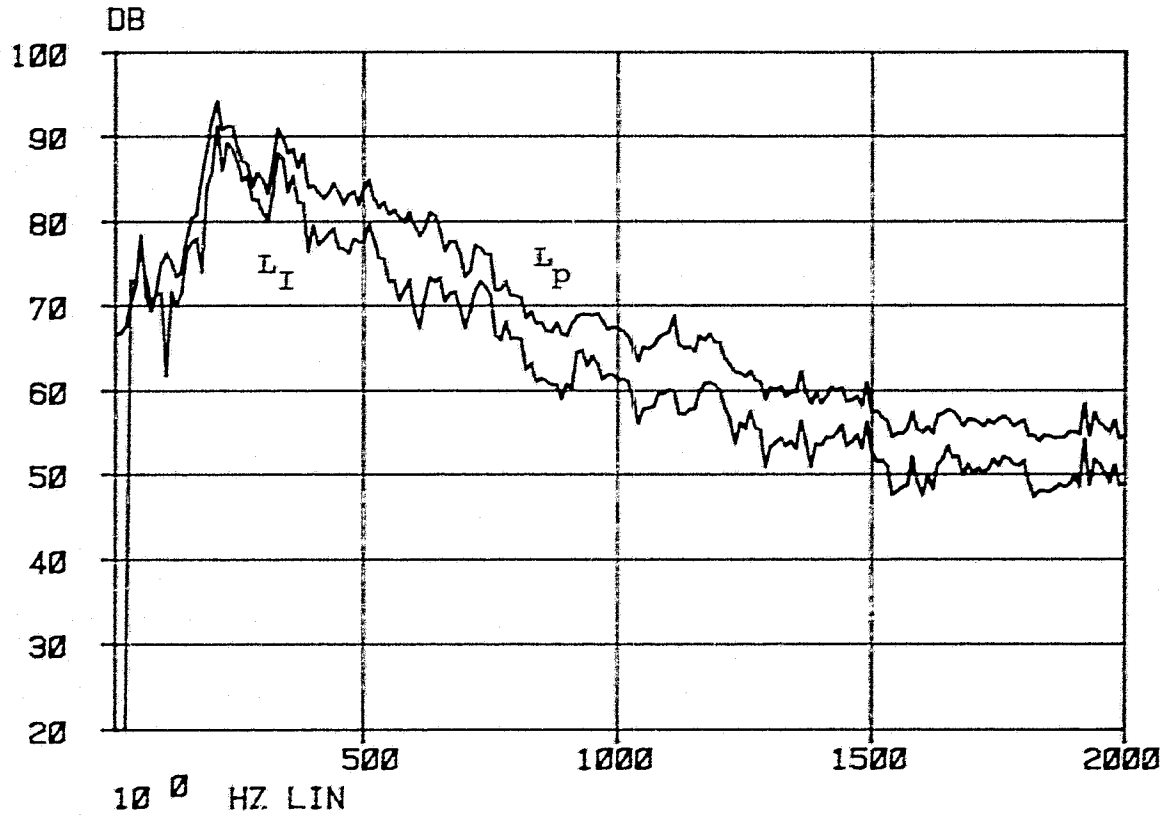

Figure 3.24 Sound pressure level, L_p, and intensity level, L_I, of the area between the windows presented over narrow frequency bands and expanded in the frequency range 0 to 2000 Hz.

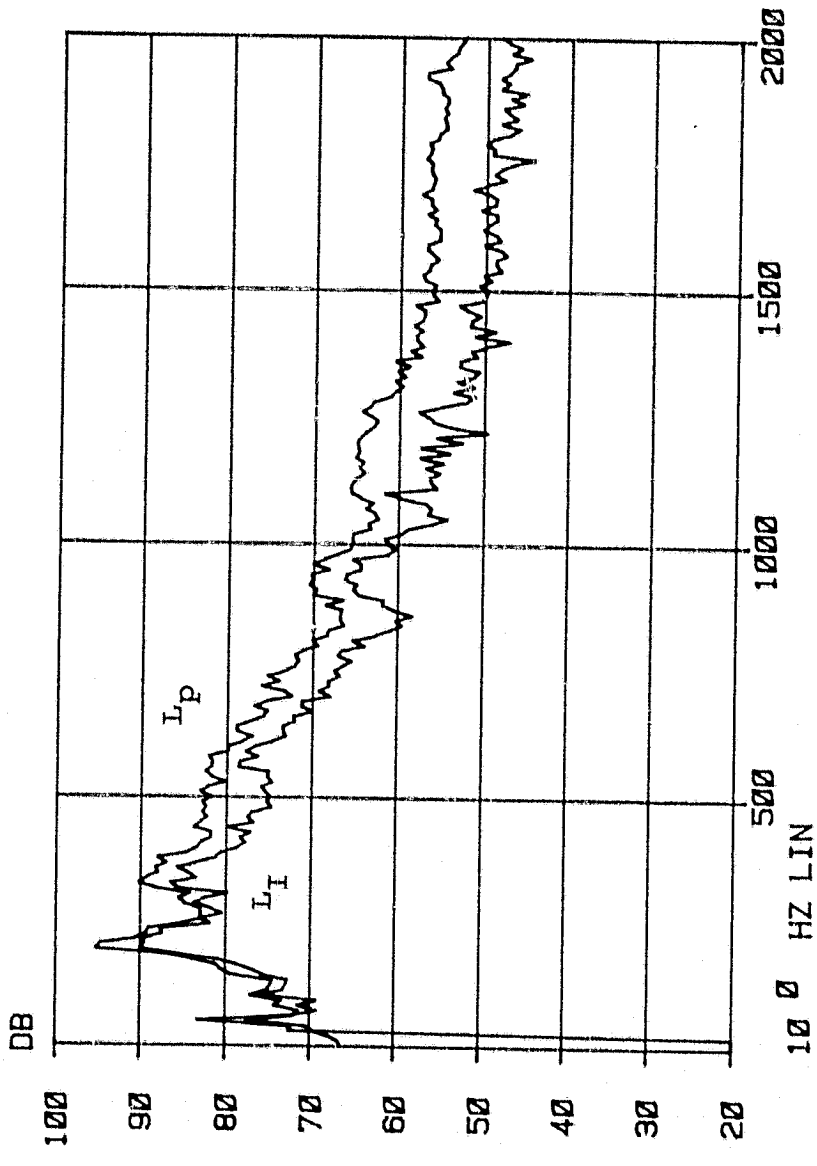

Figure 3.25 Sound pressure level, L_p, and intensity level, L_I, of the lower left stiffened bay presented over narrow frequency bands and expanded in the frequency range range 0 to 2000 Hz.

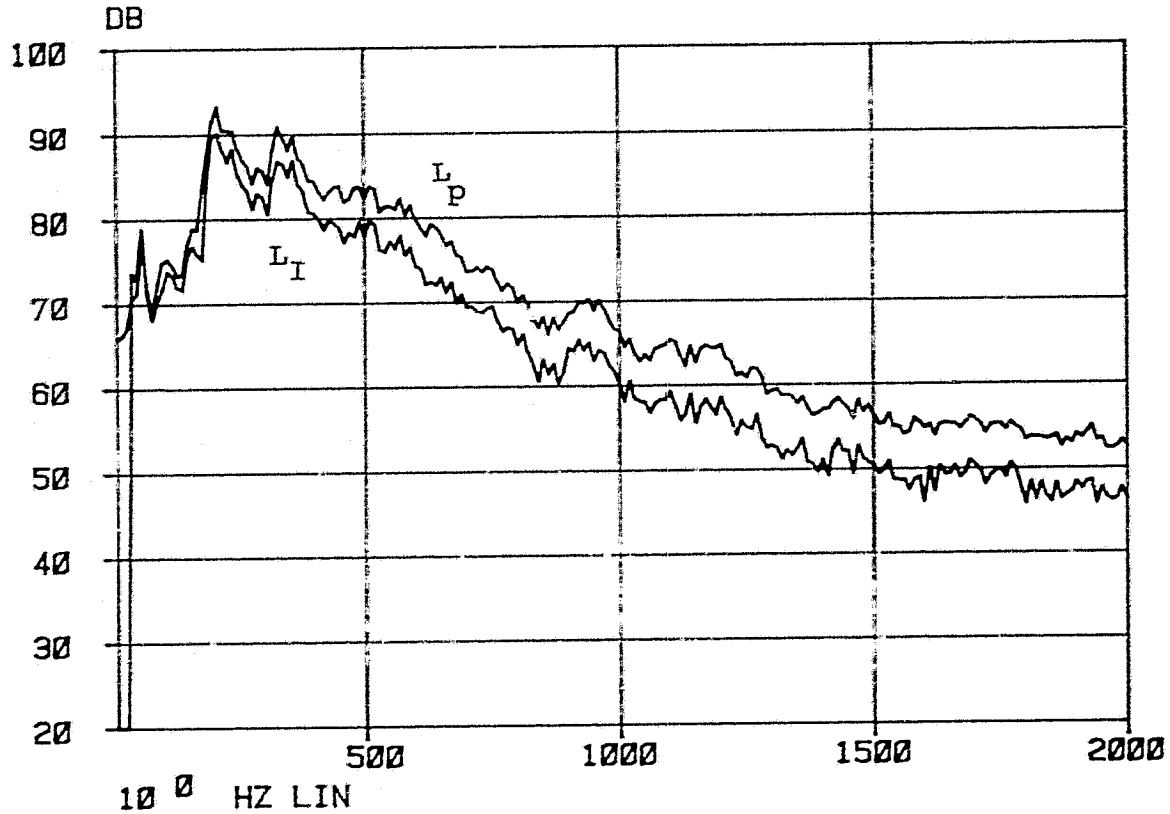

Figure 3.26 Sound pressure level, L_p, and intensity level, L_I, of the whole stiffened panel presented over narrow frequency bands and expanded in the range of 0 to 2000 Hz.

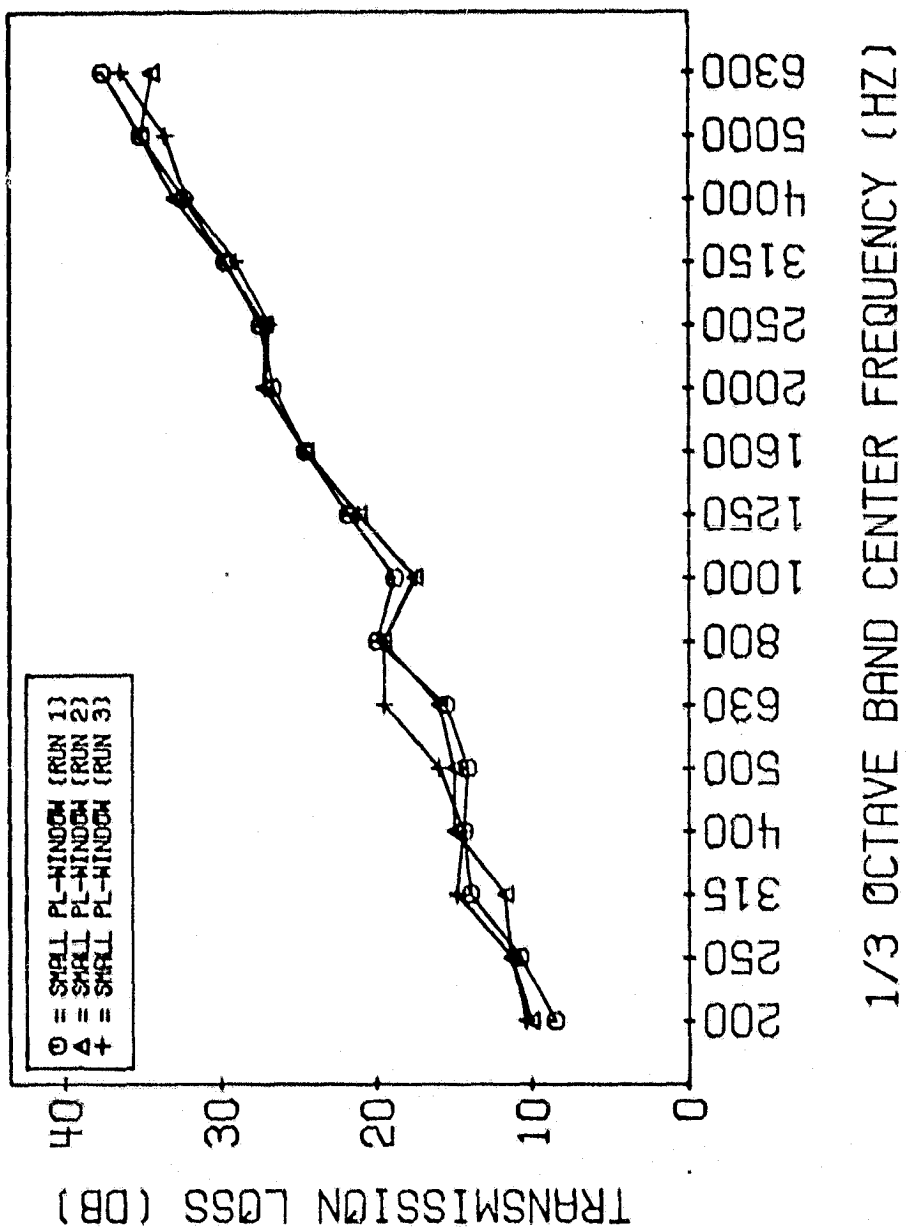

Figure 3.27 Comparison between the three measurements of the transmission loss of the small plexiglass window in the stiffened panel.

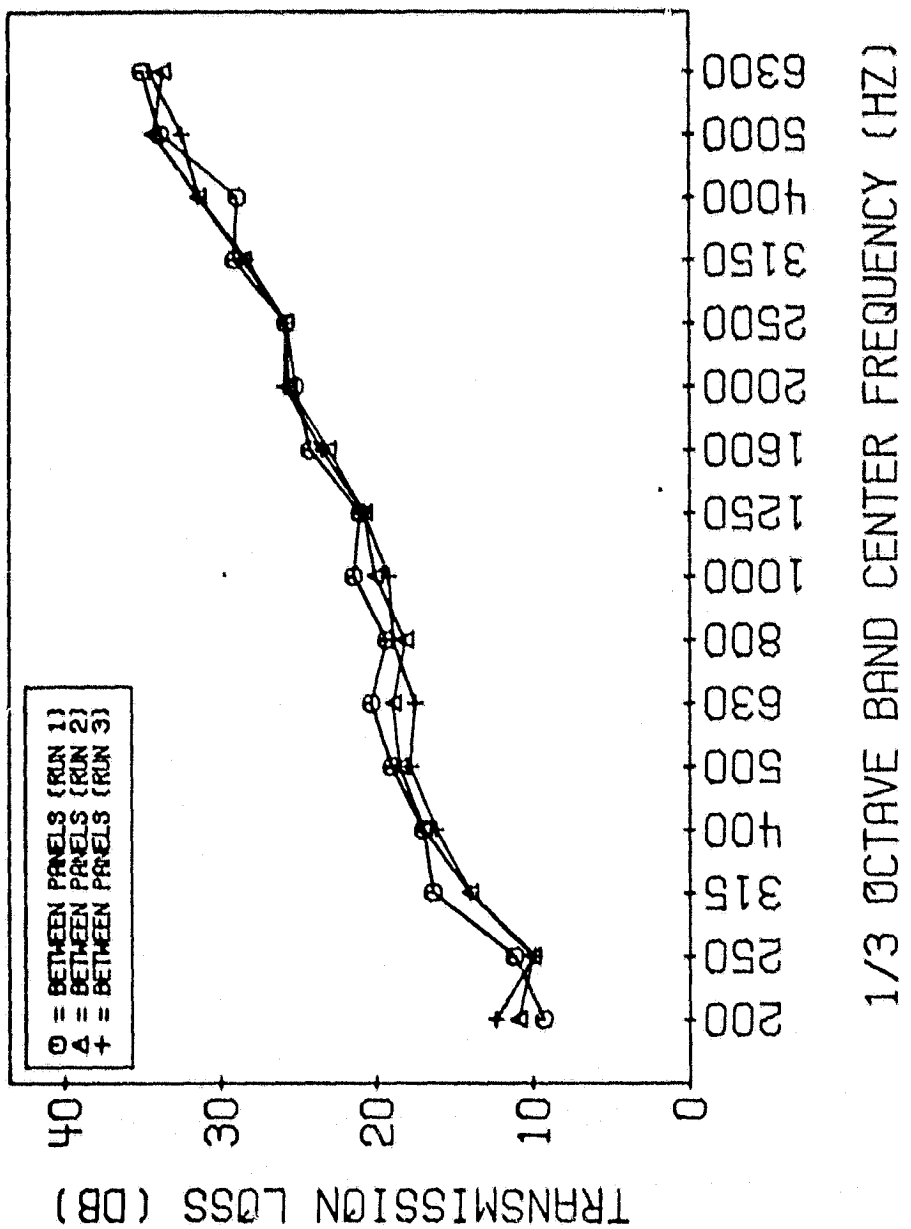

Figure 3.28 Comparison between three measurements of the transmission loss of the area in between the windows in the stiffened panel.

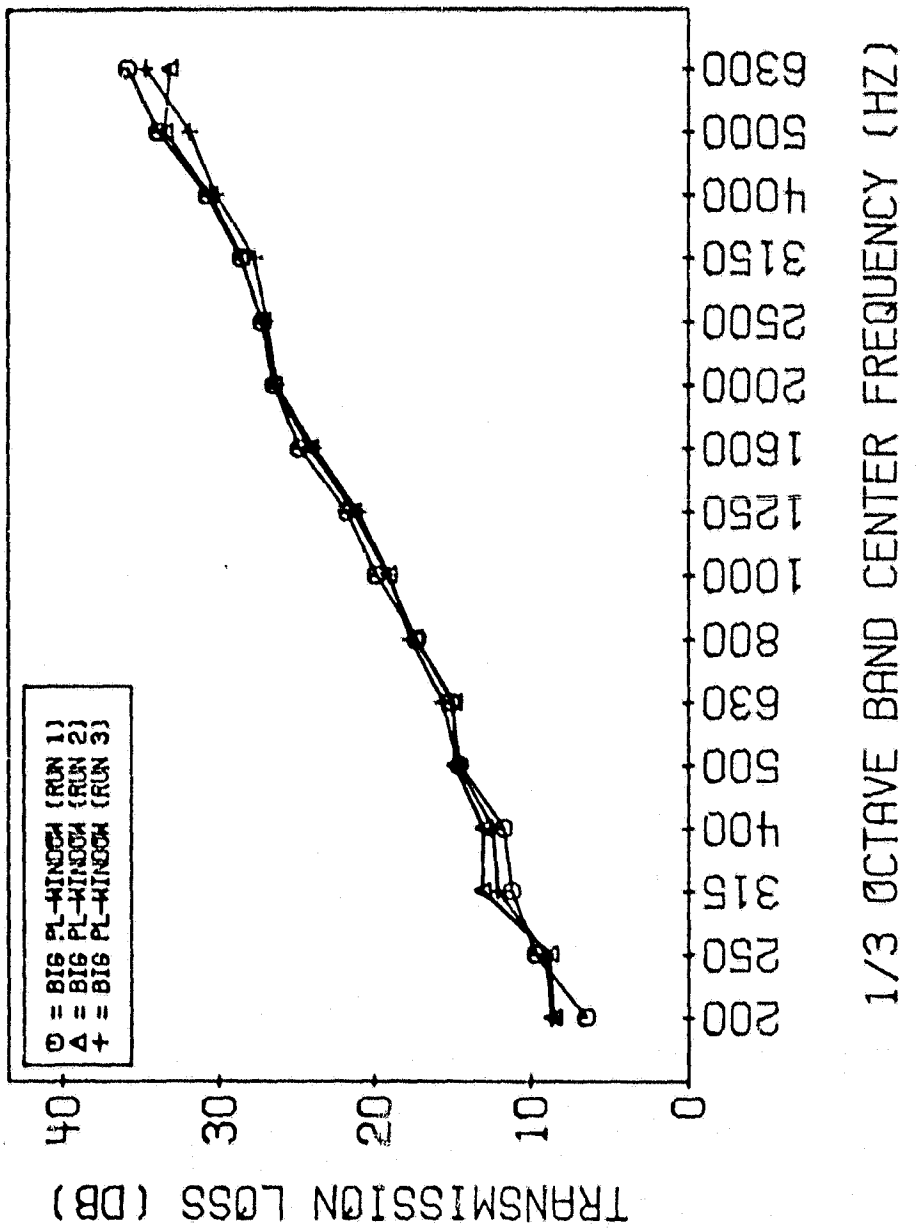

Figure 3.29 Comparison between three measurements of the transmission loss of the big plexiglass window in the stiffened panel.

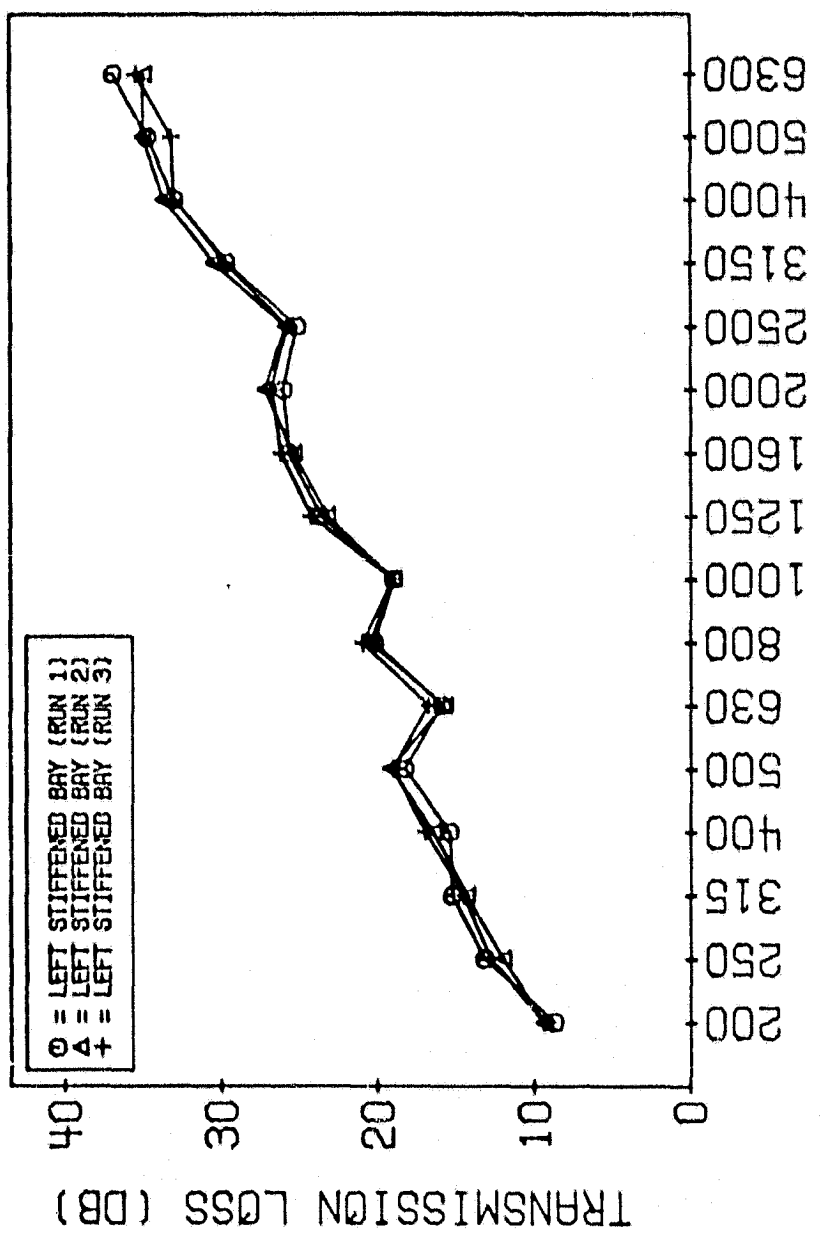

Figure 3.30 Comparison between three measurements of the transmission loss of the left stiffened bay of the stiffened panel.

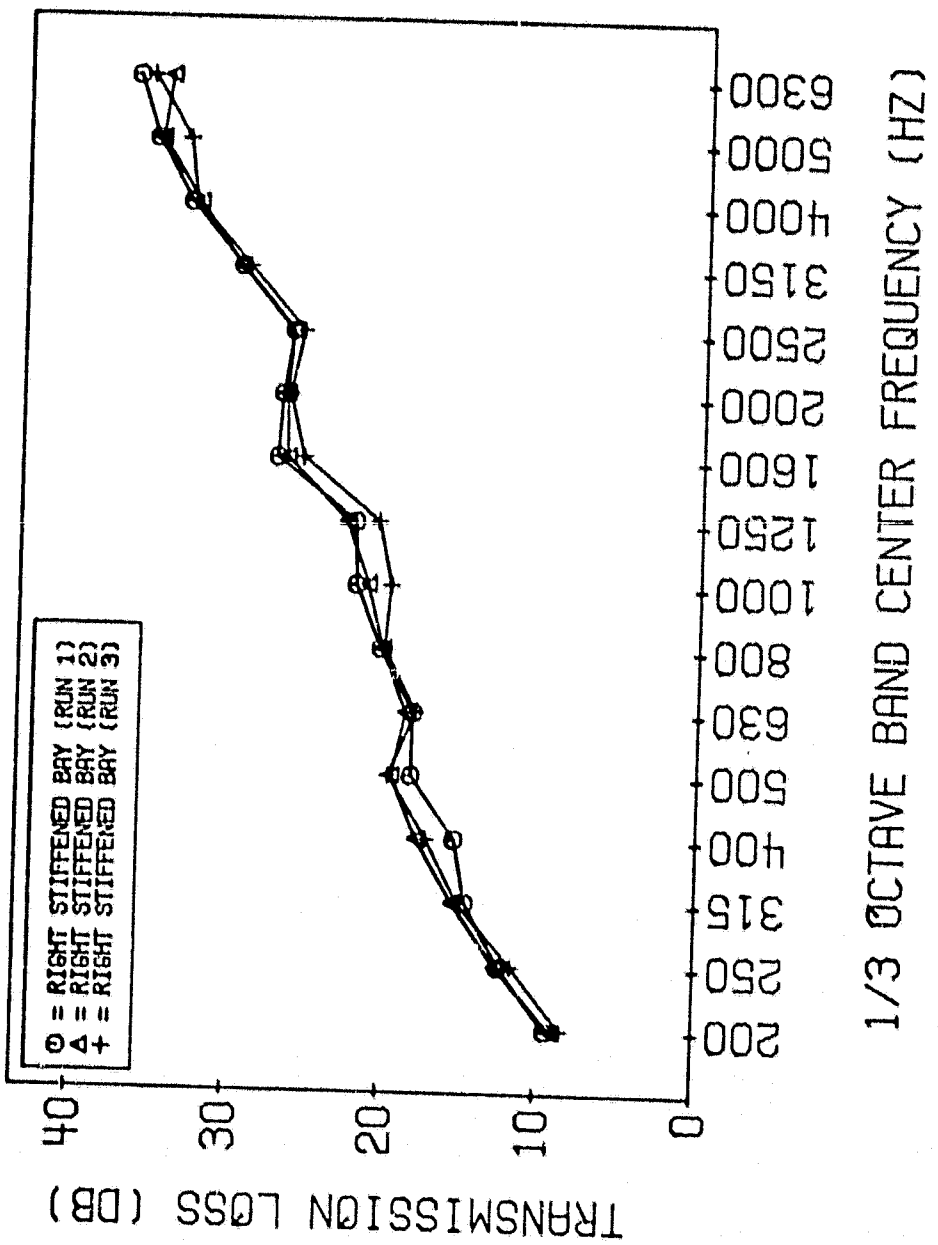

Figure 3.31 Comparison between three measurements of the transmission loss of the right stiffened bay of the stiffened panel.

The comparison between theory and measurement is shown in figure 3.32. The internal loss factor of the plexiglass, was assumed as 0.1. The critical coincidence frequency of the aluminum panel is about 9900 Hz. It is seen that the agreement between measured and predicted values is good between 100 Hz and 5000 Hz. Outside this range the intensity values obtained with the one-half inch microphones taped together, are not valid.

3.4 Comparison Between the Single, Composite and Stiffened Panel

The transmission losses of the aluminum sub-area on the composite and stiffened panels are compared with those of the aluminum panel in Figure 3.33. The aluminum part of the composite panel and the whole panel is 3.18 mm thick. This gives a critical coincidence frequency of 3987 Hz. The corresponding values for the aluminum part of the stiffened panel are 1.28 mm and 9900 Hz. Since, in the region below the critical coincidence frequency, the transmitted intensity is approximately halved if the thickness is halved for the same material (see Eq. 9), it follows that the graph corresponding to the stiffened panel should be lower. In fact it should be about 8dB lower which is the case for most of the one-third octave bands. As can be seen in figure 33, the higher critical coincidence frequency is the reason why the coincidence dip has been shifted to higher frequencies for the stiffened panel. If these reasons are taken into account it seems that the three graphs agree fairly well.

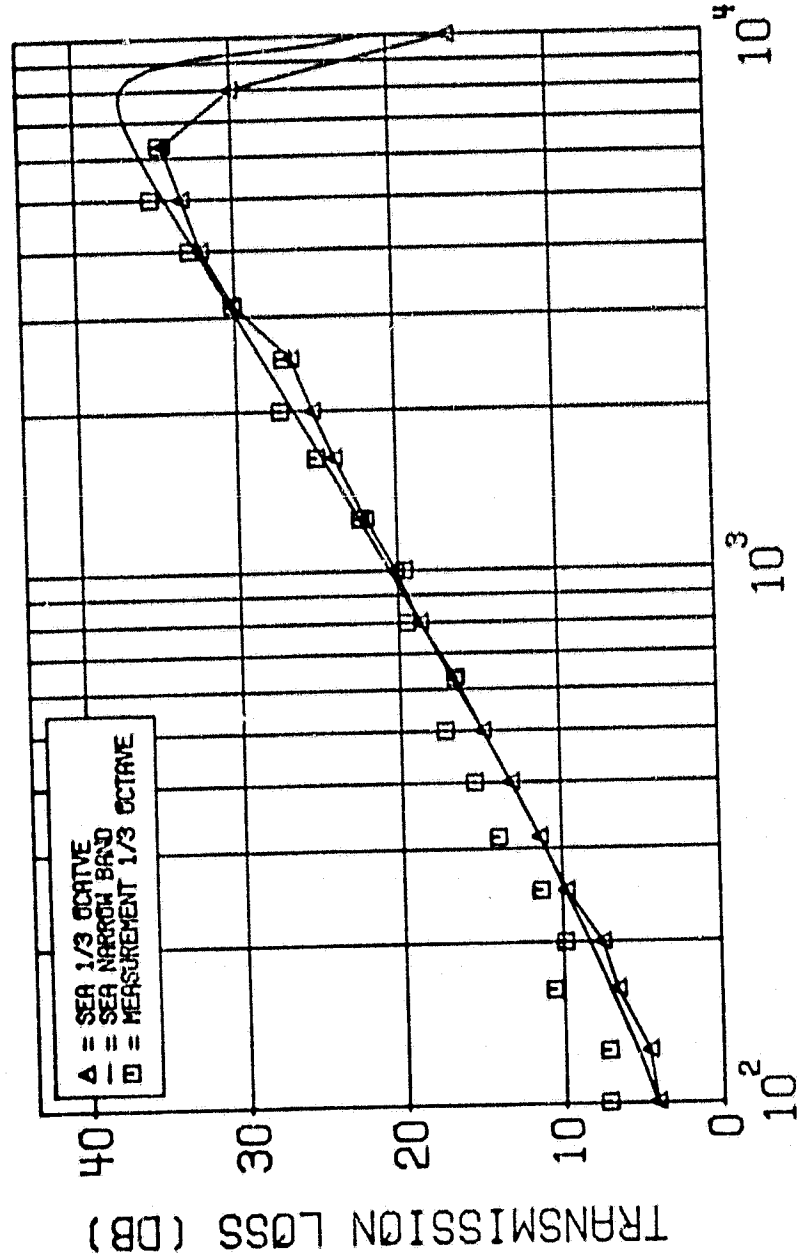

Figure 3.32 Comparison between predicted and measured values of transmission loss of the stiffened panel.

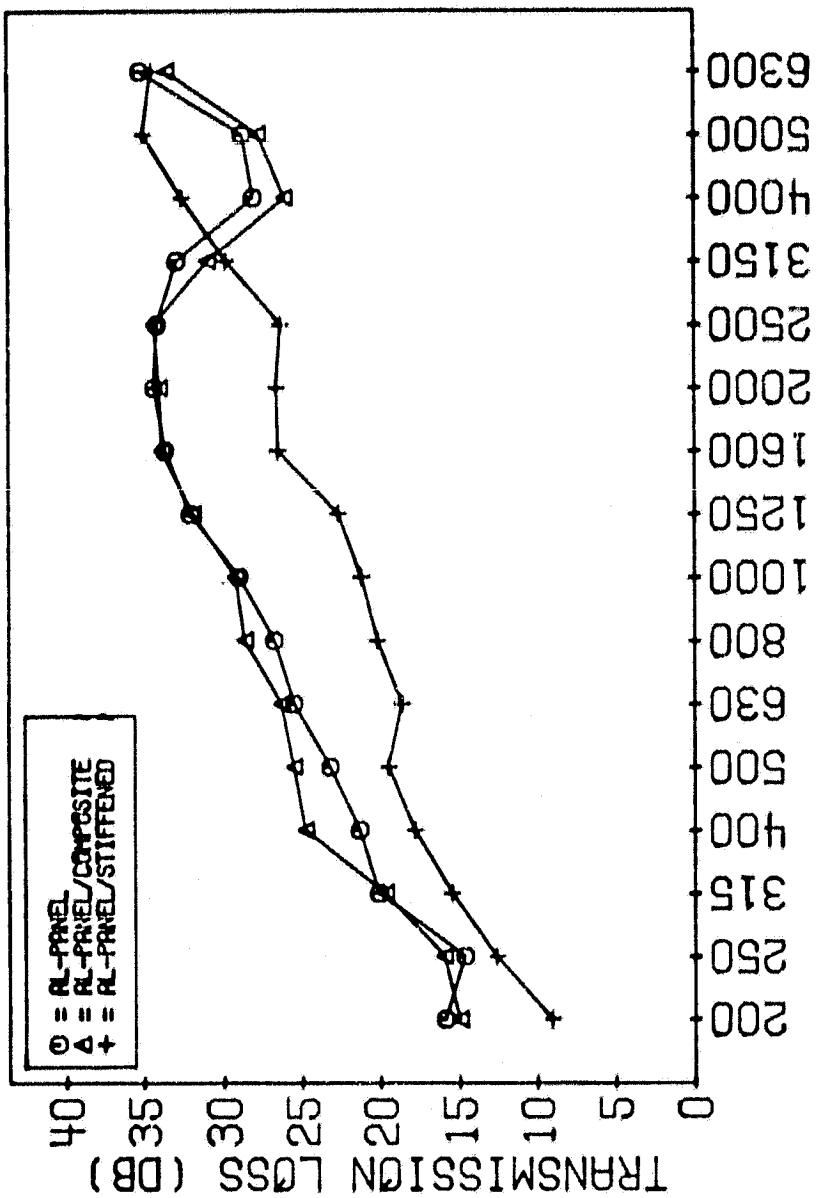

Figure 3.33 Comparison between the transmission loss measured on the aluminum area of the whole aluminum, composite and stiffened panels.

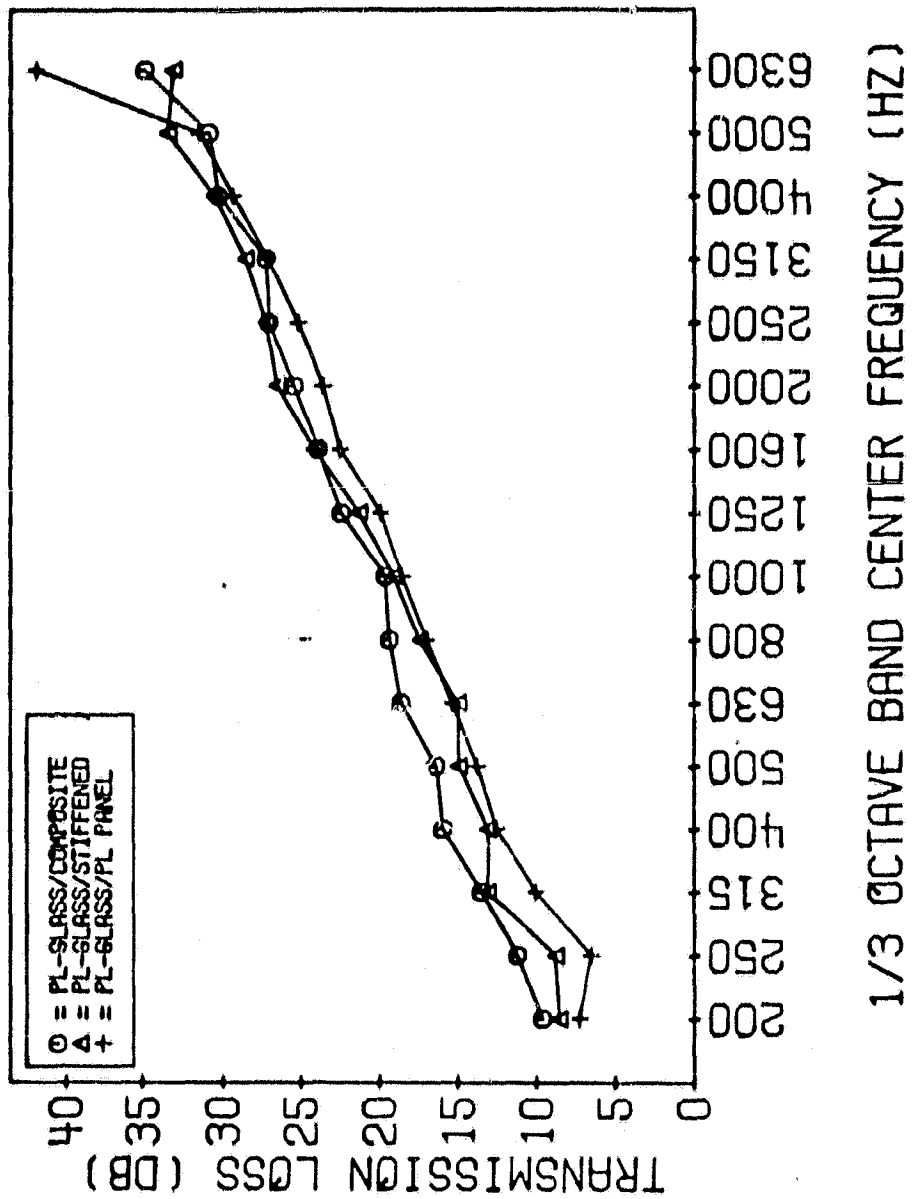

Figure 3.34 Comparison between the transmission loss measured on the plexiglass area of the whole plexiglass, composite and stiffened panels.

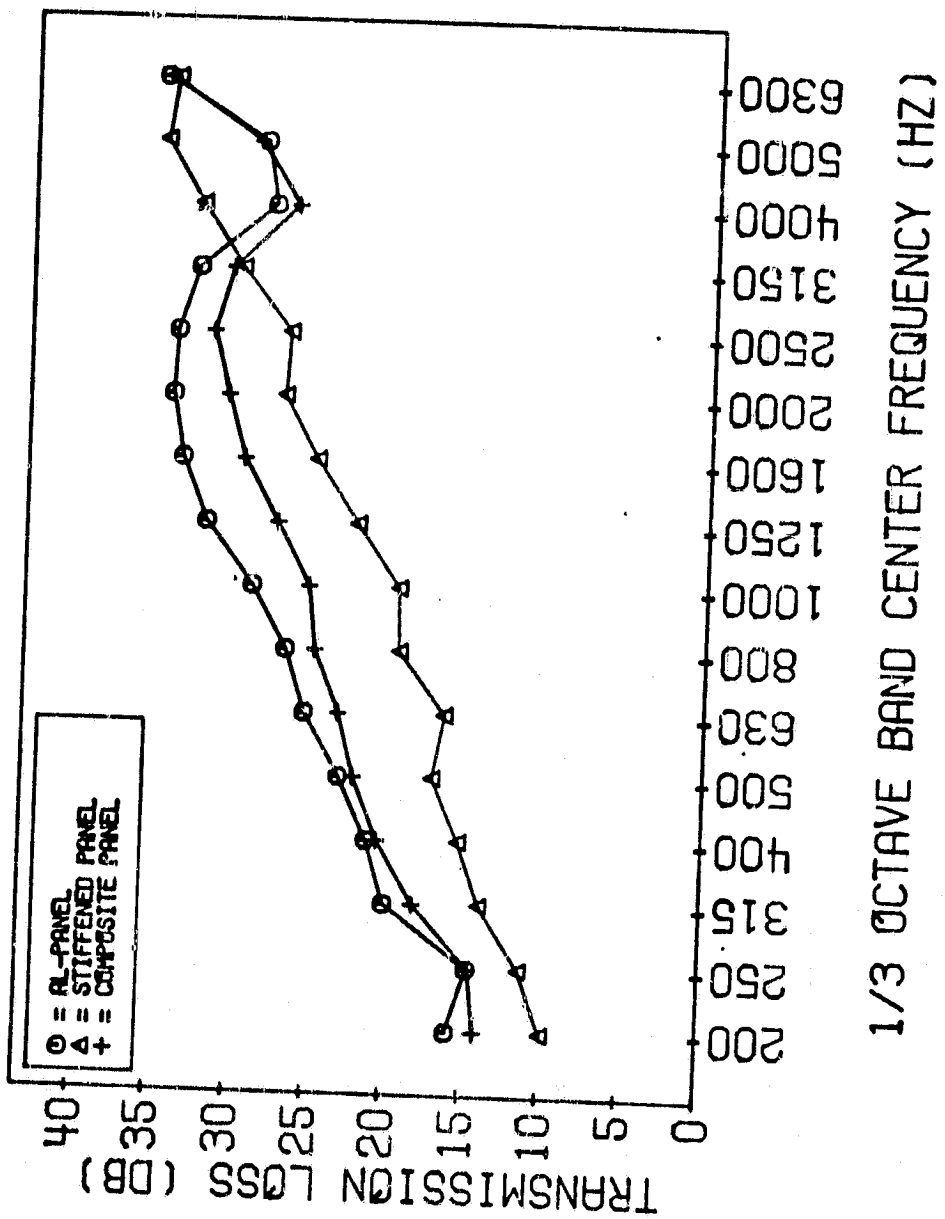

Figure 3.35 Comparison between the transmission loss values in one third octave bands of the whole aluminum, composite, and stiffened panels.

A similar comparison, but for the plexiglass panel is shown in Figure 3.34. It seems that the agreement is fairly good for frequencies above 1000 Hz. Finally, a comparison of the transmission loss of the three panels is shown in Figure 3.35. If the graph of the stiffened panel is raised by about 8 dB for the aforementioned reasons it agrees fairly well with the graph of the aluminum panel. It seems that the effect of the plexiglass window in lowering the transmission loss is more pronounced for the composite panel.

4. THE PREDICTION OF THE SOUND PRESSURE LEVEL IN A RECTANGULAR CAVITY CONNECTED TO A RADIATING PANEL

4.1 Introduction

The estimate of the sound pressure level inside cubic or rectangular cavities is not a new and unsolved problem. It has been discussed in several texts and papers [42,43,44]. Usually, expressions for the sound pressure level at an arbitrary position due to an arbitrary source distribution are determined directly, by using an expansion in eigen functions [43] and employing a green's function technique. The solution for cases, where the walls are acoustically hard, are relatively simple to obtain. However, for a finite wall impedance the eigen functions become complex and the approximate solution is difficult to obtain.

Another approach is the image source theory [41]. In this

theory the reflections from the walls (which could have a finite and the room equation do not give a relation between the sound wall impedance) are modeled as image sources. Adding up all the contributions from all the sources then gives the sound pressure spectrum at an arbitrary position. The equation is similar to the known room equation and is easy to program on the computer. The image source theory has been used to estimate the sound pressure level along the center line of a fuselage cavity in reference [40]. No comparisons between theory and measurement were shown in it. The image source theory has been used in this project. The equation given in reference [41] is basically of the same form as that used in [40]. The equation has been extended here for a three dimensional case. This theory and a discussion between predicted and measured values are presented here.

At this point it should be said that both the image theory and the room equation do not give a relation between the sound pressure level at a point and the spatial distribution of the impedance on the boundary of the enclosure. In both these equations, the room constant only accounts for an average absorption coefficient which is based on the reverberation time.

4.2 The Image Source Theory

consider first a source located between four parallel walls (forming a corridor) as shown in Figure 4.1. S and OB stand for the source and observer respectively. The solid lines are direct

or reflected sound paths, (from the source to the observer). The dashed lines indicate the location of the image sources. If j is an index in the Z direction, it is seen in Figure 1 that the Z coordinates for sources on the positive side of the Z axis are:

$$Z_j^+ = Z_{j-1}^+ + 2\left[- q_j\right]Z_o + Zq_j\left[H - Z_o\right] \quad j=1,2,3... \quad (4.1)$$

where:

$$q_j = \frac{1}{2}\left[1 -(-1)^j\right] \quad (4.2)$$

Similarly the Z coordinates for the image sources on the negative side are given by:

$$Z_j^- = Z_{j-1}^- + Zq_jZ_o - z\left[1-q_j\right]\left[H-Z_o\right] j=1,2,3... \quad (4.3)$$

where H is the height of the corridor and Z_o is the real Z coordinate. The corresponding equations in the Y-direction are

$$Y_i^+ = Y_{i-1}^+ + 2\left[1-q_i\right]\ Y_o + Zq_i\ \left[W-Y_o\right], i=1,2,3... \quad (4.4)$$

and

$$Y_i^- = Y_{i-1}^- - 2q_iY_o - 2\left[1-q_i\right]\left[W-Y_o\right]\ i=1,2,3... \quad (4.5)$$

where W is the width of the corridor and Y_o is the Y-coordinate of the real source and

$$q_i = \frac{1}{2}\left[1-(-1)^i\right] \quad (4.6)$$

If now reflections are allowed in the X-Direction, the corridor becomes an enclosure and two more equations need to be added:

$$X_k^+ = X_{k-1}^+ + 2\left[1-q_k\right]X_o + 2q_k\left[H-Z_o\right] k=1,2,3... \qquad (4.7)$$

and

$$X_k^- = X_{k-1}^- - 2q_kX_o - 2\left[1-q_k\right]\left[L-X_o\right] k=1,2,3... \qquad (4.8)$$

where L is the length of the enclosure, X_o is the X-coordinate of the real source and

$$q_k = \frac{1}{2}\left[1-(-1)^k\right] \qquad (4.9)$$

The total sound pressure level L_p at the observer position OB (X,Y,Z) is given by the room equation:

$$L_p = L_\omega + 10 \log\left[\frac{Q}{4\pi r^2} + \frac{4}{R_T}\right] \qquad (4.10)$$

where L_ω is the sound power level caused by the source, Q is the directivity factor, R_T is the room constant and r is the distance between the observer and the real source. In the image theory the room constant is given by

$$\frac{4}{R_T} = \sum_{ijk}\frac{\Pi_{ijk}}{\Pi 4\pi\ r_{ijk}^2}\Bigg]_{\text{pos.sources}} + \sum_{ijk}\frac{\Pi_{ijk}}{\Pi 4\pi\ r_{ijk}^2}\Bigg]_{\text{neg.sources}} \qquad (4.11)$$

where

$$r_{ijk}^2 = \left[X_k^{\pm} - X_o\right]^2 + \left[Y_i^{\pm} - Y_o\right]^2 + \left[Z_j^{\pm} - Z_o\right]^2 \qquad (4.12)$$

Π is the total acoustic power radiated by a real source, and Π_{ijk} is the power emitted by the (i,j,k) th image source. Π_{ijk} is given by

$$\Pi_{ijk} = \Pi\, F(\alpha_r,k)*F(\alpha_l,-k)*F(\alpha_u,j)*F(\alpha_d,-j)*F(\alpha_f,-i)*F(\alpha_a,i) \tag{4.13}$$

with

$$F[\alpha,h] = [1-\alpha]^{g(h)} \tag{4.14}$$

and

$$g(h) = \begin{cases} 0 & K = 0 \ , \\ |h/2| \ ; & h \text{ even} \ , \\ \text{integer } |\ 1/2h| + 1 & \text{for h; odd; positive,} \\ \text{integer } |\ 1/2h| & \text{for h; odd; negative,} \end{cases} \tag{4.15}$$

where the subscripts r, l, u, d, f and a stand for right, left, up, down, front and aft, α is the absorption coefficient given by

$$\alpha \simeq \frac{60V}{CST} \tag{4.16}$$

where V is the enclosure volume, S is the interior surface area, T is the reverberation time of the enclosure and C is the speed of sound.

The image theory is based on the following assumptions:

1. each sound source is a simple point source with a constant acoustic power output,
2. the acoustic response of each wall can be described in terms of an average sabine absorption coefficient ,
3. the plane walls can be replaced by a set of gradually fading image s, and

4. the contribution of all sources (real and image) are added incoherently.

4.3 Interior Noise Level as a Function of Space and Frequency

The image theory, discussed in the previous section, is now applied to the fuselage in the following suggested way: consider first the experimental set-up shown in figure 4.2. The idea here is that the structure is divided into substructures or more correctly into sub areas. It was decided that the division into subareas should be based on the structural differences within the panel. The plexiglass elements, the stiffened part of the panel in between the windows, as well as the area below the windows as seen in Figue 4.2 formed the different subareas. Since all the sources are considered to be incoherent, the room equation is now modified to account for a summation from all sources,

$$L_p\left[r_{ijk},f\right] = \sum_n \left\{ L_w\left[r_{ijk},f\right] + 10 \log\left[\frac{1}{4\pi\, r_{ijk}^2} + \frac{4}{R_T(f)}\right]\right\} \quad (4.17)$$

where n is the number of subareas and $L_w(r_{ijk},f)$, is the radiated intensity from the n th element times the area.

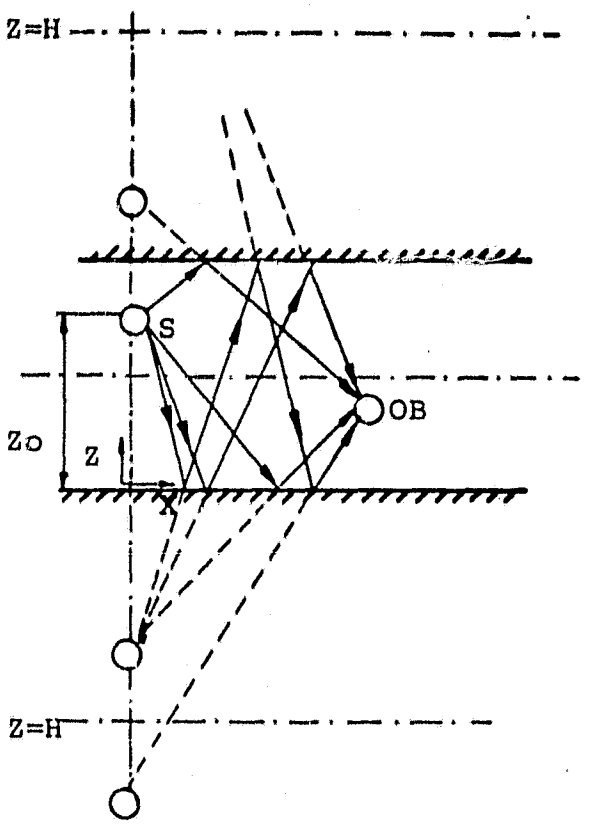

Figure 4.1 The location of observer (OB) and real source (S) position and image source locations, for the image source model.

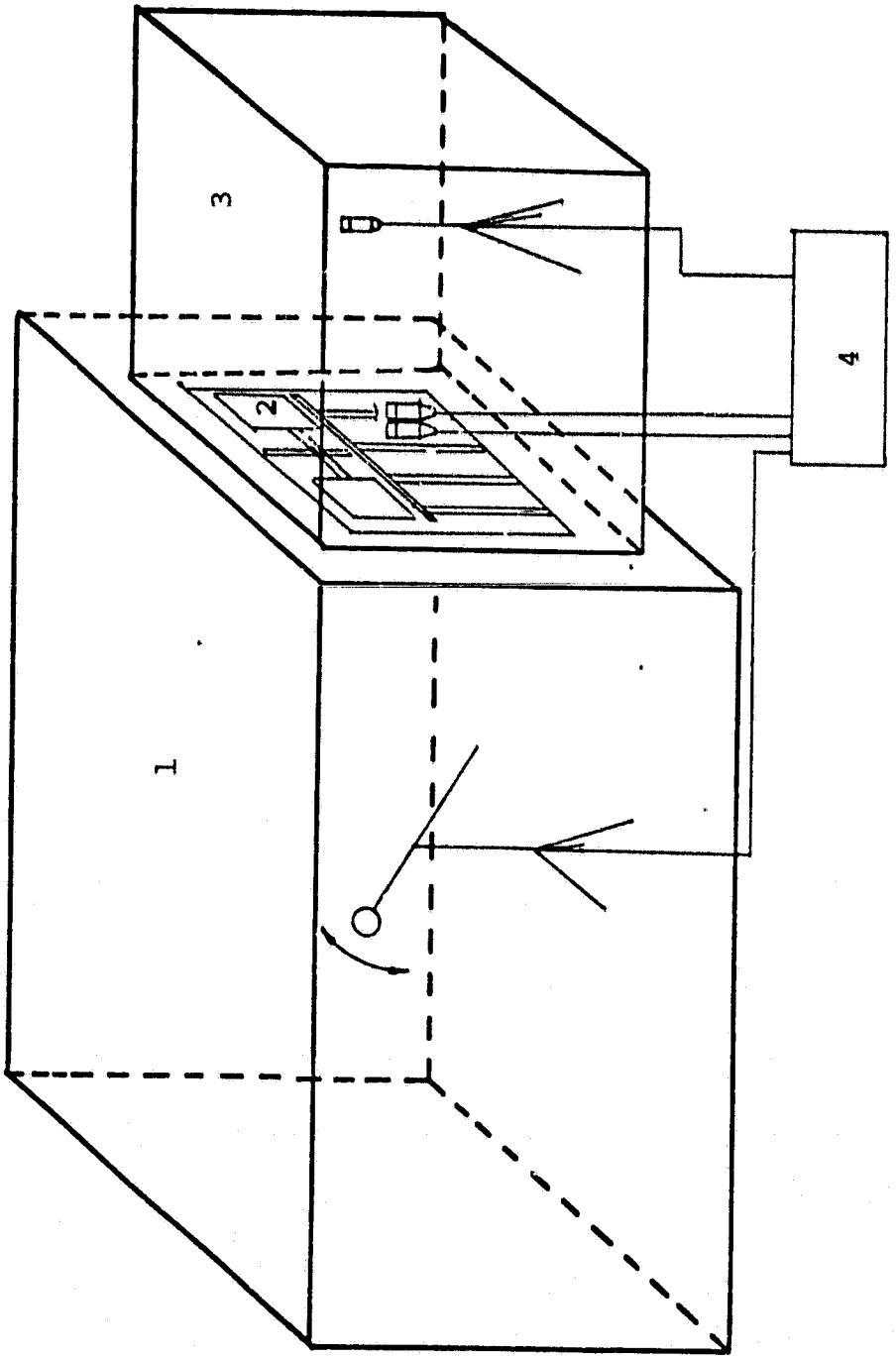

Figure 4.2 Experimenal set-up for the image source model.

1. Reverberation room
2. Stiffened panel
3. Box
4. Filters, pre-amplifiers and FFT

4.4 Experimental Procedures

The side of the panel, in Figure 4.2, which is facing the reverberation room was excited by a reverberant sound field with an overall level of about 130 dB. This level was generated by an electro-pneumatic driver and a jet noise source. For all measurements; the auto power spectrum from the rotating boom in the reverberation room and the signals from the microphone in the cavity as well as the cross power spectrum from the two microphones on the cavity side, were sampled 100 times. These spectra were then stored on the disc and later processed in a fortran routine based on equations (4.10) and (4.11).

The pressure supplied to the electro-pneumatic driver could, for the given sound pressure level, only be maintained at a constant level with fluctuations of 10% for about five minutes. This had the result that the noise source had to be turned off and on between all measurements of the intensity level from the subareas, the intensity level in the reverberation room and the sound pressure level in the cavity. It is difficult to estimate the error inherited in this procedure. It is believed to be within 1dB, for most frequencies. The sweeping of the two microphones was carried out as described in Chapter 3.

4.5 Results and Discussion

The results obtained by using the image theory as well as those obtained by the room equation were calculated and compared.

The room constant used was:

$$\frac{4}{R_T} = \frac{4}{-\sum_n S_n \, l_n \, (1-\alpha_n)} \qquad (4.18)$$

where S_n = subarea and α_n is the aborption coefficient from the n th sub area (diffuse field theory). In the following pages a preliminary output from the fortran subroutine for the case of the stiffened panel is given. In the output the following abbreviations are used:

SPLT = sound pressure level at the observer position (measured)

IMTH = sound pressure level at the observer position predicted by the image source theory.

DFTH = sound pressure level at the observer position predicted by the diffuse field theory

INLV = intensity level from the sub area (source no. X)

The last page of the out put shows the contribution from all sources. The number of sources (5 real + all images) was about 30,000. The image theory and diffuse field theory for the evaluation of sound pressure level inside the cavity seem to agree fairly well with the measured values between 400 Hz and 2500 Hz.

Table 1
OUTPUT FROM THE IMAGE SOURCE PROGRAM

source-co			room-dim			obs-co		
.00	.13	.94	1.78	1.27	1.22	.80	.53	.85

sum-lim			absorption-coeff.					
15	15	15	.10	.10	.10	.10	.10	.10

area					
2.20	2.26	2.26	2.20	1.42	1.42

Contribution From Source No. 1

Freq. Hz.	SPLT	IMTH	DFTH	INLV
163	85.46	75.00	75.66	81.25
200	100.00	88.35	89.01	94.60
250	95.87	90.75	91.41	97.00
315	95.11	87.32	87.98	93.57
400	95.28	85.91	86.58	92.16
500	92.83	84.71	85.37	90.96
630	93.34	78.37	79.03	84.62
800	85.14	71.48	72.15	77.73
1000	80.39	70.63	71.29	76.88
1250	77.02	65.16	65.82	71.41
1600	71.62	60.27	60.93	66.52
2000	70.01	57.52	58.18	63.77
2500	69.52	56.54	57.20	62.79
3150	67.24	52.61	53.27	58.86
4000	64.88	46.92	47.58	53.17
5000	65.85	43.07	43.73	49.32
6300	66.12	53.93	54.59	60.18
8000	64.20	48.98	49.64	55.23

Contribution From Source No. 2

Freq. Hz.	SPLT	IMTH	DFTH	INLV
163	85.46	74.80	75.47	77.52
200	100.00	93.89	94.56	96.61
250	95.87	94.38	95.05	97.10
315	95.11	88.89	89.55	91.61
400	95.28	87.30	87.98	90.02
500	92.83	84.17	84.84	86.89
630	93.34	80.11	80.78	82.84
800	85.14	76.95	77.62	79.68
1000	80.39	71.78	72.45	74.51
1250	77.02	68.48	69.15	71.20
1600	71.62	64.23	64.89	66.95
2000	70.01	61.15	61.82	63.87
2500	69.52	61.08	61.75	63.80
3150	67.24	57.22	57.89	59.94
4000	64.88	51.68	52.34	54.40
5000	65.85	49.91	50.58	52.63
6300	66.12	57.49	58.16	60.21
8000	64.20	53.17	53.84	55.89

Contribution From Source No. 3

Freq. Hz	SPLT	IMTH	DFTH	INLV
163	85.46	78.06	78.76	81.77
200	100.00	90.32	91.03	94.04
250	95.87	94.41	95.11	98.13
315	95.11	89.22	89.92	92.94
400	95.28	90.70	91.40	94.42
500	92.83	86.62	87.33	90.34
630	93.34	83.75	84.46	87.47
800	85.14	76.65	77.35	80.37
1000	80.39	71.51	72.21	75.22
1250	77.02	67.78	68.48	71.50
1600	71.62	62.88	63.58	66.59
2000	70.01	60.41	61.11	64.12
2500	69.52	59.30	60.00	63.01
3150	67.24	57.22	57.93	60.94
4000	64.88	51.53	52.24	55.25
5000	65.85	51.77	52.47	55.48
6300	66.12	56.33	57.04	60.05
8000	64.20	49.80	50.50	53.51

Contribution From Source No. 4

Freq. Hz.	SPLT	IMTH	DFTH	INLV
163	85.46	81.04	81.74	80.59
200	100.00	95.49	96.19	95.05
250	96.87	97.15	97.85	96.70
315	95.11	92.47	93.17	92.03
400	95.28	92.24	92.94	91.80
500	92.83	87.81	88.51	87.36
630	93.34	84.82	85.52	84.38
800	85.14	77.46	78.17	77.02
1000	80.39	75.18	75.88	74.74
1250	77.02	69.34	70.04	68.90
1600	71.62	64.44	65.14	64.00
2000	70.01	63.62	64.33	63.18
2500	69.52	63.61	64.31	63.17
3150	67.24	57.58	58.28	57.14
4000	64.88	52.08	52.79	51.64
5000	65.85	51.90	52.60	51.46
6300	66.12	59.58	60.29	59.14
8000	64.20	55.45	56.15	55.01

Contribution From Source No. 5

Freq. Hz.	SPLT	IMTH	DFTH	INLV
163	85.46	84.96	85.69	84.55
200	100.00	95.95	96.68	95.54
250	95.87	96.70	97.43	96.29
315	95.11	93.86	94.59	93.45
400	95.28	87.48	88.21	87.07
500	92.83	86.58	87.31	86.17
630	93.34	83.53	84.26	83.12
800	85.14	76.91	77.64	76.50
1000	80.39	72.78	73.51	72.37
1250	77.02	69.31	70.04	68.91
1600	71.62	64.36	65.09	63.95
2000	70.01	63.59	64.32	63.18
2500	69.52	64.11	64.84	63.70
3150	67.24	59.24	59.97	58.83
4000	64.88	53.79	54.52	53.38
5000	65.85	54.18	54.91	53.77
6300	66.12	59.74	60.47	59.33
8000	64.20	55.74	56.47	55.33

Contribution Of All Sources

Freq. Hz.	SPLT	IMTH	DFTH	INLV
163	85.46	87.53	88.24	80.47
200	100.00	100.68	101.38	93.03
250	95.87	102.19	102.89	94.33
315	95.11	98.03	98.73	89.67
400	95.28	96.37	97.07	88.07
500	92.83	93.17	93.87	84.71
630	93.34	89.72	90.42	80.58
800	85.14	83.32	84.02	73.92
1000	80.39	79.67	80.37	70.02
1250	77.02	75.25	75.94	65.35
1600	71.62	70.48	71.17	60.34
2000	70.01	68.78	69.49	58.03
2500	69.52	68.73	69.43	57.50
3150	67.24	64.23	64.93	53.25
4000	64.88	58.69	59.39	47.46
5000	65.85	58.36	59.06	46.61
6300	66.12	64.90	65.60	53.13
8000	64.20	60.44	61.15	48.23

OVERALL VALUES (dB)

SPLT	IMTH	DFTH
104.05	106.32	107.02

If an assumed value for α of 0.1 for all 1/3 octave bands [29] is used the agreement in sound pressure-level is within about 3 dB. However, if measured values of α are used the agreement is within about 5 dB.

The disagreement between theory and measurement of the sound pressure level might be caused by several sources of error. One source might be caused by turning the noise source off and on. It was found that, in order to supply the electro-pnuematic driver with about 20 psia which was needed to bring the overall

level up to about 130 dB, the pressure to the driver fluctuated about 10%. Another possible error lies in the intensity measurement. As discussed in the previous section, the sweeping on the stiffened panel was made over an imaginary surface about 5mm from the beams and the beam width + 5mm in between the beams. This might have lead to some contamination from other subareas for almost all frequencies. A third problem might be that the sources are to some extent coherent and therefore assumption (4) in section 4.2 is violated.

In summary, the agreement between experimentally and theoretically determined sound pressure levels is within 3 to 5 dB depending upon the value of used in the prediction scheme. We plan more experiments in an attempt to reveal the problem.

5. REFERENCES

1. R. J. Alfredson, "A New Technique for Noise Source Identification on a Multi-cylinder Automotive Engine," Noise-Con. 77 Proceedings, pp. 307-318, 1977.

2. F. J. Fahy, "Measurement of Acoustic Intensity Using the Cross-Spectral Density of Two Microphone Signals," J. Acoust. Soc. AM. 62, (4), pp. 1057-1059, 1977.

3. J. Y. Chung and J. Pope, "Practical Measurement of Acoustic Intensity - The Two Microphone Cross-Spectral Method. Internoise 78 Proceedings, pp. 893-900, 1978.

4. M. J. Crocker, B. Forssen, P. K. Raju, Anna Melnika, "Measurement of Transmission loss of Panels by an Acoustic Intensity Technique," Internoise 80 Proceedings, pp. 741-746, 1980.

5. M. J. Crocker, P. K. Raju, B. Forssen, "Measurement of Transmission Loss by the Direct Determination of Transmitted Acoustic Intensity," (to be published in Noise Control Engineering).

6. J. Y. Chung, "Cross-Spectral Method of Measuring Acoustic Intensity Without Error Caused by Instrument Phase Mis-Match," J. Acoust. Soc. AM. 64 (6) pp. 1613-1616, 1978.

7. G. Krishnappa, "Cross-Spectral Method of Measuring Acoustic Intensity by Correcting Phase and Mis-Match Errors by Microphone Calibration," J. Acoust. Soc. AM. 69, pp. 307-310, 1981.

8. T. H. Hodgson, "Investigation of the Surface Intensity Method for Determining the Noise Sound Power of a Large Machine in Situ," J. Acoust. Soc. AM., 61, (2), pp. 487-493, 1977.

9. J. D. Brito, "Sound Intensity Patterns for Vibrating Surfaces," Ph.D. Thesis, MIT 1976.

10. J. D. Brito, "Machinery Noise Source Analysis Using Surface Intensity Measurements," Noise Con. 79 Proceedings, pp. 137-142, 1979.

11. N. Kaemmer, "Determination of Sound Power From Intensity Measurements on a Cylinder," MSME Thesis, Purdue University, 1978.

12. M. C. McGary, "Noise Source Identification of Diesel Engines Using Surface Intensity Measurement," MSME, Purdue University, 1980.

13. M. C. McGary and M. J. Crocker, "Surface Intensity Measurements on a Diesel Engine," Noise Control Engineering, Vol. 16, pp. 26-36, 1981.

14. J. A. McAdam, "The Measurement of Sound Radiation from Room Surfaces in Light Weight Buildings," Applied Acoustics, 9, pp. 103-118, 1976.

15. G. Pavic, "Measurement of Sound Intensity," J. Sound and Vib., 51, (4), pp. 533-545, 1977.

16. G. Pavic, "Measurement of Structure Borne Wave Intensity. Part I: Formulation of the Methods," J. Sound and Vib., 49, (2), pp. 221-230, 1976.

17. J. W. Verheij, "Cross Spectral Density Methods for Measuring Structure Borne Power Flow on Beams and Pipes," J.Sound and Vib., 70, (1), pp. 133-139, 1976.

18. A. F. Seybert, "Statistical Errors in Acoustic Intensity Measurements," to be published in J. Sound and Vib.

19. A. H. Davies, "Reverberation Equations for Two Adjacent Rooms Connected by an Incompletely Sound Proof Partition," Phil. Mag., 50, pp. 75-80, 1925.

20. E. Buckingham, "Theory and Interpretation of Experiments on the Transmission of Sound Through Partition Walls," Nat'l Bureau of Stand. Sci. Papers., 20, pp. 194-199, 1929.

21. T. Mariner, "Critique of the Reverberant Room Method of Measuring Air-Borne Sound Transmission Loss," J. Acoust. Soc. AM, 33, (4), pp. 1131-1139, 1961.

22. R. F. Higginson, "A Study of Measuring Techniques for Airborne Sound Insulation in Buildings," J. Sound Vib., 21, (4), pp. 405-429, 1972.

23. A London, "Transmission of Reverberant Sound Through Double Walls," J. Res. Nat'l Bur. Stand US 44, pp. 77-88, 1950.

24. American Society for Testing and Materials "Recommended Practice No. E336," for measurement of airborne sound insulation in buildings 1971 and "Recommended practice E90 Laboratory Measurement of Airborne Sound Transmission Loss," 1970.

25. I. L. Ver and C. I. Holmer, "Interaction of Sound Waves with Solid Structures," in Noise and Vibration Control, edited by L. L. Beranek, McGraw-Hill, New York, 1971.

26. L. Cremer, M. Heckl and E. E. Unger, Structure Borne Sound (Springer Verlag, New York, 1973.)

27. M. J. Crocker and A. J. Price, "Sound Transmission Using Statistical Energy Analysis," J. Sound and Vib. , (9), pp. 469-486, 1969.

28. R. E. Jones, "Intercomparison of Laboratory Determinations of Airborne Sound Transmission Loss," J. Acoust. Soc. AM, 66, pp. 148-164, 1979.

29. E. B. Magrab, Environmental Noise Control, (John Wiley and Sons, pp. 265-268, 1975.) Handbook of Noise Control, edited by C. M. Harris (McGraw-Hill, New York) pp. 1-11, 1979.

30. M. J. Crocker and A. J. Price, Noise and Noise Control, (CRC Press, Cleveland) pp. 28-29, 1975.

31. J. S. Bendat and A. G. Piersol, Random Data Analysis and Measurement Procedure, John Wiley and Sons, New York, pp. 67-86, 1971.

32. R. H. Lyon, Statistical Energy Analysis of Dynamical Systems: Theory and Applications, MIT Press, 1975.

33. M. J. Crocker, "The Response of Structures to Acoustic Excitation and the Transmission of Sound and Vibration," Ph.D. thesis, University of Liverpool, (1969).

34. G. Maidanik, "Response of Ribbed Panels to Reverberant Acoustic Fields," Acoust. Soc. AM 34, 809, 1962.

35. C. F. Gerald, Applied Numerical Analysis, Addison - Wesley, 1978.

36. R. Upton, "Automated Measurements of Reverberation Time Using the Digital Frequency Analyzer Type 2131," Technical Review, B & K, 2, 1977.

37. K. Nakayama, "Prediction of the Sound Pressure Level Inside a Vibrating Rectangular Steel Box Using a Statistical Energy Analysis," MSME Thesis, Purdue University, 1979.

38. L. Cremer, M. Heckl, E. E. Ungar, Structure Borne Sound, Springer-Verlag, New York, 1973.

39. D. C. Rennison, J. F. Wilby, A. H. Marsh, E. G. Wilby, "Interior Noise Control Prediction Study for High Speed Propeller Driven Aircraft," NASA Contractor Report, 159200, 1979.

40. A. G. Galaitsis, W. N. Patterson, "Prediction of Noise Distribution in Various Enclosures from Free Field Measurements," J. Acoust. Soc. AM., Vol. 60, (4), 1976.

41. P. M. Morse, K. U. Ingard, Theoretical Acoustics, McGraw-Hill, 1968.

42. E. J. Richards, D. J. Meade, Noise and Acoustic Fatigue in Aeronautics, Wiley 1968.

43. M. Battacharya and M. J. Crocker, "Forced Vibrations of a Panel and Radiation of Sound into a Room," Acustica, 22, (5), pp. 275-294, 1969/70.

PART II

LIST OF FIGURES

LIST OF SYMBOLS

$A(t)$	Acceleration (m/sec^2)
C	Damping decay rate (dB/sec)
c	Speed of sound (m/sec)
D	Bending stiffness $\left[D = \frac{Eh^3}{12\left[1-\mu^2\right]}\right]$
E	Young's modulus
f	Frequency (Hz)
f_r	Ring frequency (Hz)
f_c	Critical coincident frequency (Hz)
h	Thickness of the material (m)
k	Acoustic wavenumber
k_a	Longitudinal wavenumber function
k_c	Circumferential wavenumber function
L	Length of the cylinder (m.)
M	Mass of the cylinder per unit area (kg/m^2)
m	Longitudinal mode number
n	Circumferential mode number
$n(\omega_o)$	Modal density at angular frequency ω_o
P	Radiated acoustic power (Watts)
R	Radius of the cylinder (m)
R_{mech}	Mechanical resistance
R_{rad}	Radiation resistance
S	Surface area (m^2)
T_R	Reverberation time (sec.)
TL	Transmission loss (dB)

TL_{nr}	Non-resonant transmission loss
TL_{res}	Resonant transmission loss
U	Displacement (m)
v	Velocity (m/sec)
x, θ	Cylindrical coordinates
$\langle\ \rangle$	Spatial averaging of the argument function

GREEK LETTERS

η_m	Roots of the analogous beam
η_{mech}	Damping loss factor
ζ	Critical damping ratio
ρ_m	Density of the material (kg/m^3)
ρ_o	Density of air (kg/m^3)
ν_o	Normalized frequency
μ	Poisson's ratio
σ	Radiation efficiency

1. INTRODUCTION

During recent years, there has been a growing interest in the interior noise levels of general aviation aircraft. The noise is associated primarily with sources such as the propellers, the engines, and the engine exhaust. Studies of general aviation aircraft have indicated that the noise is transmitted into the interior through airborne and structure -borne paths. At the same time, there has been an increasing demand on the general aviation industry to reduce the cabin noise levels. Hence, it is important to study the noise transmission characteristics of such aircraft structures.

The sound transmission property of a structure may be evaluated from a knowledge of its transmission loss, which is proportional to the ratio of the incident sound power to the transmitted sound power. Hence development of both accurate prediction and evaluation techniques is very important in the study of sound transmission through fuselage walls. Here in the second part of this report, the fuselage structure has been idealized into a cylindrical shell. The dimensions of the cylinder were designed to simulate a half-scale model of a light aircraft fuselage. The transmission loss was theoretically estimated by using Statistical Energy Analysis (SEA). The parameters involved in SEA model, such as modal densities and radiation efficiencies were obtained from the wavenumber diagrams. The theoretical prediction will be discussed in Section 2.

Section 3 discusses the experimental evaluation of sound transmission loss through the cylinder. The transmitted intensity was measured using the two-microphone acoustic intensity technique. The results obtained from the experiments compared well with those from the theoretical predictions.

2. THEORETICAL MODEL - SOUND TRANSMISSION THROUGH A CYLINDRICAL SHELL

2.1 Natural Frequencies of a Cylindrical Shell

The vibration analysis of a cylindrical shell is one of the most widely investigated problems in engineering. Many past successful efforts in obtaining information on the natural frequencies and mode shapes of different cylinders with different boundary conditions have been summarized by Leissa [1]. Conventionally, the equation of motion of a circular cylindrical shell is derived from Love's equation. For example, for a cylinder which is simply-supported at the two ends, the general solution for the motion can be assumed to be:

$$U_x(x,\theta) = A \cos \frac{m\pi x}{L} \cos n(\theta-\Phi) ,$$

$$U_\theta(x,\theta) = B \sin \frac{m\pi x}{L} \sin n(\theta-\Phi) , \qquad (2.1)$$

$$U_3(x,\theta) = C \sin \frac{m\pi x}{L} \cos n(\theta-\Phi) ,$$

where U_x, U_θ, U_3 are displacements in longitudinal, circumferential and transverse directions respectively; m, n are mode numbers, and x, θ are coordinates. Theoretically, a solution for the natural frequencies can be found when the eigen functions in Equation 2.1 are substituted into the equation of motion. Unfortunately, the solutions are too complicated to be applied in real engineering problems [2]. When the transverse vibration is considered exclusively, the formula to calculate the natural frequencies can be largely simplified using some practical assumptions. This simplified equation is known as the Donnell-Mushtari-Vlasov equation.

2.1.1 Donnell-Mushtari-Vlasov Equation

Donnell [3,4] and Mushtari [5] simplified the equation of motion for a thin cylindrical shell by focusing attention on the problem of transverse deflection, and made the following assumptions [2],

a. The contributions of in-plane deflection can be neglected in bending strain expressions, but not in the membrane strain expressions.

b. The influence of inertia in the in-plane direction is negligible.

c. The transverse shear terms can be neglected.

d. The mode number n, the length L, and the radius R of the cylinder, satisfy the inequality such that [6].

$$\left[n^2/R^2\right] \gg \left[\lambda/L\right]^2$$

where λ and C are the constants used in the solution

$$U_3 = Ce^{\lambda x/L}\cos\left[n(\theta-\phi)\right]$$

The natural angular frequencies of a circular cylindrical shell can then be reduced to

$$\omega_{mn} = \sqrt{\frac{1}{\rho_m h}\frac{EhR^2}{L^4 n^4}\eta_m^4 + D\left[\frac{n}{R}\right]^4}\ , \qquad (2.2)$$

where ρ_m is the mass density of material, h is the thickness, m and n are mode numbers in the longitudinal and circumferential direction respectively, and E and D are Young's modulus and bending stiffness. The only variable η_m which is the roots of the analogous beam equation, can be determined from the boundary conditions.

Soedel [7] in his recent paper claimed that the assumption (d) in the previous paragraph is not absolutely necessary in most circular cylindrical shell cases. He modified the formula for the natural frequencies into the following form:

$$\omega_{mn} = \sqrt{\frac{Eh\eta_m^4}{R^2L^4\left[\frac{n^2}{R^2}+\frac{\eta_m^2}{L^2}\right]^2} + D\left[\frac{n^2}{R^2}+\frac{\eta_m^2}{L^2}\right]^2}\ \sqrt{\frac{1}{\rho_m h}}\ . \qquad (2.3)$$

For the case of simply-supported boundary conditions at both ends, the above formula can be reduced to:

$$\omega_{mn} = \frac{1}{R}\sqrt{\frac{\left[\frac{m\pi R}{L}\right]^4}{\left[\frac{m\pi R}{L}\right]^2+n^2} + \frac{\left[\frac{h}{R}\right]^2}{12\left[1-\mu^2\right]}\left[\left[\frac{m\pi R}{L}\right]^2+n^2\right]^2}\ \cdot\sqrt{\frac{E}{\rho_m}}\ , \qquad (2.4)$$

where μ is Poisson's ratio. Szechenyi [8] derived the same equation in a different form

$$\omega_{mn}^2 = \frac{Eh^2}{12\rho_m\left[1-\mu^2\right]}\left\{\left[\frac{m\pi}{L}\right]^2 + \left[\frac{n}{R}\right]^2\right\}^2 + \frac{E}{\rho_m\left[1-\mu^2\right]R^2} \cdot \frac{\left[\frac{m\pi}{L}\right]^4 \left[1-\mu^2\right]}{\left\{\left[\frac{m\pi}{L}\right]^2 + \left[\frac{n}{R}\right]^2\right\}^2} \quad (2.5)$$

2.1.2 Boundary Conditions

As discussed in Section 2.1.2, Equations 2.3, 2.4, and 2.5 are formulae to calculate the natural frequencies of a simply-supported cylindrical shell. It was also mentioned that the undecided variable η_m of Equation 2.2 varies with different boundary conditions. The variable η_m is the roots of the analogous beam equation. Tests are given to see how the boundary conditions affect the natural frequencies.

Figure 2.1 shows the differences in natural frequencies between a simply-supported cylinder and a clamped cylinder. It is observed that there exists a considerable difference for mode

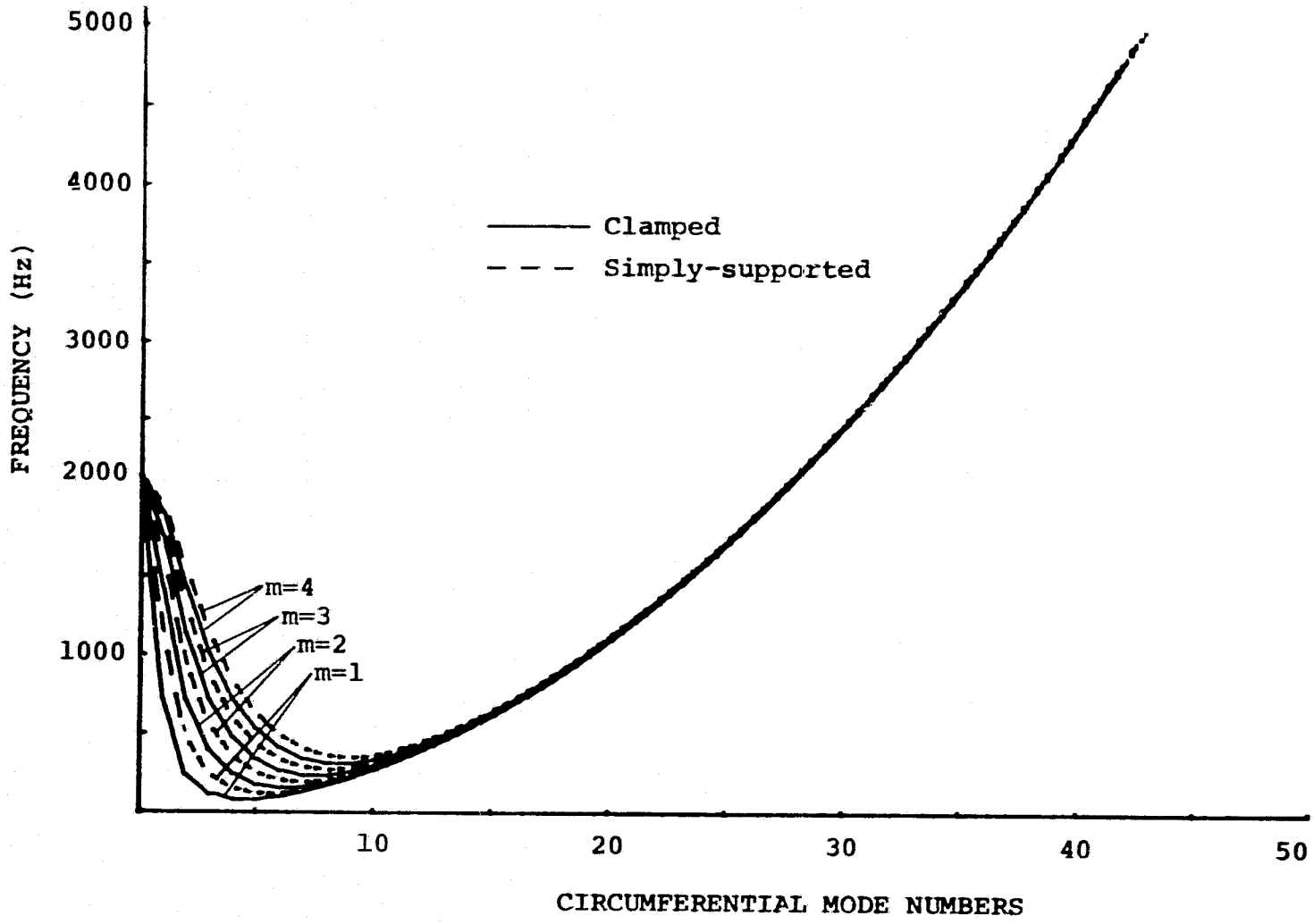

Fig. 2.1

Natural Frequencies of a Simply-Supported Cylinder (----) and a Clamped Cylinder (——).

numbers below five. However, for higher mode numbers, the differences decrease sharply. Hence the boundaries of the cylinder under investigation are assumed to be simply-supported even though they may be nearer to the clamped case. Hopefully, the error that results from this approximation is only limited to the lower modes.

2.2 The Wavenumber Diagram of a Cylinder

The wavenumber diagram (sometimes called the "k-space diagram") has been found to be a very powerful tool in the Statistical Energy Analysis (SEA). Instead of solving for each mode individually, SEA investigates the average behavior of variables over a frequency band. Among the most important parameters in SEA are the modal density, mode classification (surface modes, edge modes, and corner modes), and loss factors. All these parameters may be obtained from the wave number diagram. One other parameter, namely, the damping loss factor of the structure may have to be obtained experimentally.

2.2.1 Modal Density of Cylindrical Shell

The wavenumber functions are defined as [9]:

$$k_a = \left[\frac{m\pi}{L}\right] \left[h^2R^2/12\left[1-\mu^2\right]\right]^{1/4} , \qquad (2.6)$$

and

$$k_c = \left(\frac{n}{R}\right) \left[h^2R^2/12\left[1-\mu^2\right]\right]^{1/4} , \qquad (2.7)$$

where k_a and k_c are the longitudinal wavenumber and circumferential wavenumber functions, respectively. The advantage to use the wavenumber functions rather than frequencies is the further simplification of Equation 2.5 into the following form:

$$\omega_{mn} = \left[\left(k_a^2 + k_c^2\right)^2 + k_a^4/\left(k_a^2 + k_c^2\right)^2\right]^{1/2} \cdot 2\pi f_r , \quad (2.8)$$

where f_r is the ring frequency of the cylinder:

$$f_r = \left(\frac{1}{2\pi R}\right)\sqrt{\frac{E}{\rho_m}} .$$

If the natural frequencies are normalized by the ring frequency, Equation 2.8 becomes:

$$\nu_o = \frac{\omega_{mn}}{2\pi f_r} = \left[\left(k_a^2 + k_c^2\right)^2 + k_a^4 / \left(k_a^2 + k_c^2\right)^2\right]^{1/2} . \quad (2.9)$$

Equation 2.9 gives the relationship between normalized frequency ν_o and the two directional wavenumbers k_a and k_c. With a given frequency ν_o every value of k_c has a corresponding value of k_a. Therefore, the frequencies can be plotted on a wavenumber diagram as shown in Figure 2.2.

A frequency band, which consists of both upper and lower limits of frequencies, is plotted on the wavenumber diagram as a strip between two frequency contours. Each mode is represented by a point on the diagram. All the modes are approximately

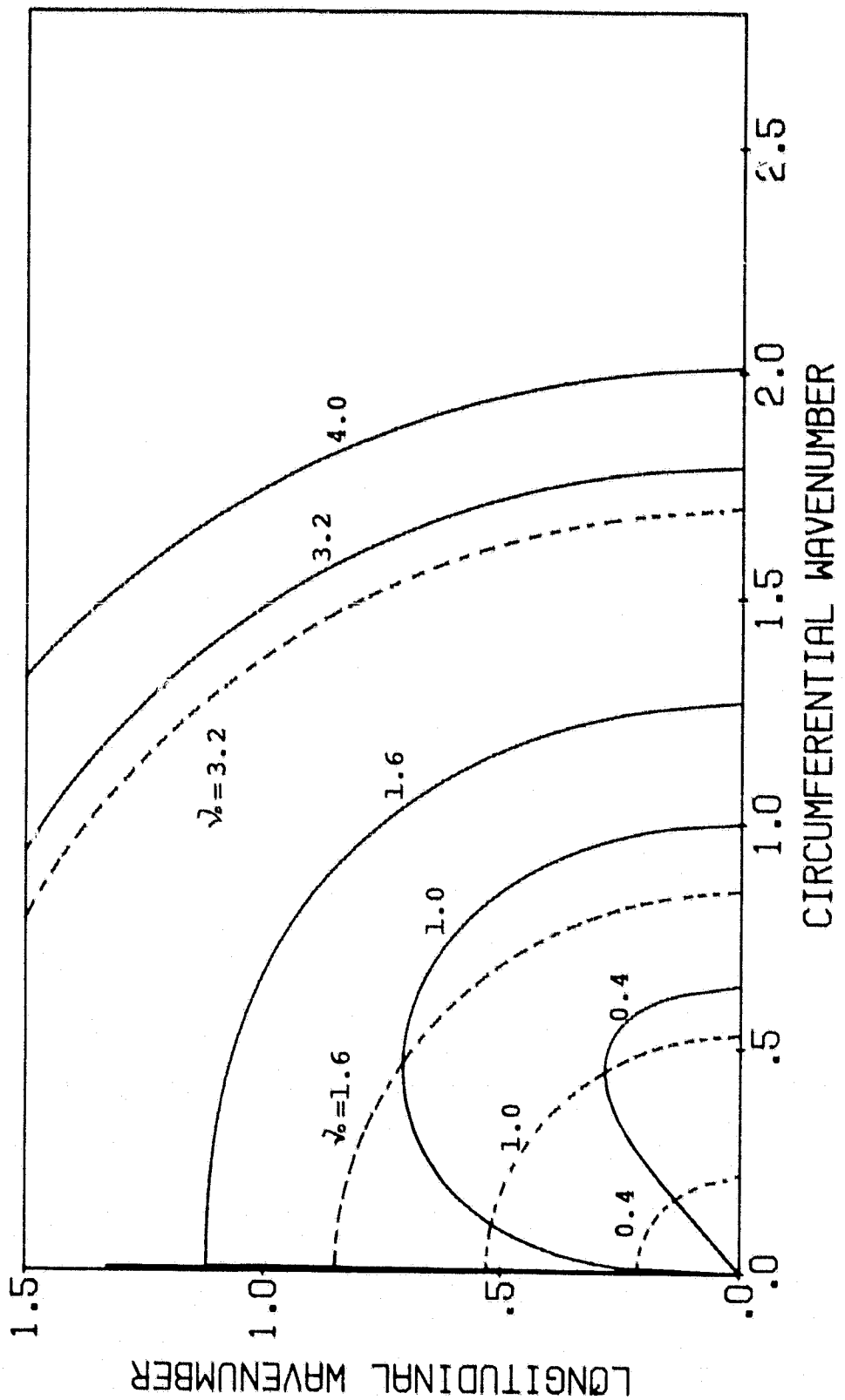

Fig. 2.2

Wavenumber Diagram; —— Structural Waves, ----- Acoustical Waves.

distributed as a regular lattice on the diagram, with each mode occupying an area equal to:

$$\frac{\pi h/L}{\left[12\left[1-\mu^2\right]\right]^{1/2}} \quad .$$

Following this concept, the number of modes in a frequency band is then equal to the ratio of the area occupied by the strip containing the frequency band to that of a unit mode. The modal density in a frequency band, given the unit as modes / Hz, can then be obtained from the number of modes and the bandwidth. Figure 2.3 gives a plot of the modal density versus frequency for the cylindrical shell under investigation.

2.2.2 Acoustic Wavenumbers

On the wavenumber diagram, for each given frequency, ν_o, the acoustic wavenumber k is plotted as a segment of a circle with a radius $\nu_o\sqrt{f_r/f_c}$. Any change in either the geometry or the material of the cylinder alters the ring frequency f_r and the critical coincidence frequency f_r. Consequently, the radius of the circle required to plot the acoustic wave number must also be adjusted. Figure 2.2 shows the plots of the structural wavenumbers and acoustic wavenumbers corresponding to the following three values of the normalized frequency ν_o, namely ν_o = 4.0, 3.2, 1.6, 1.0, and 0.4.

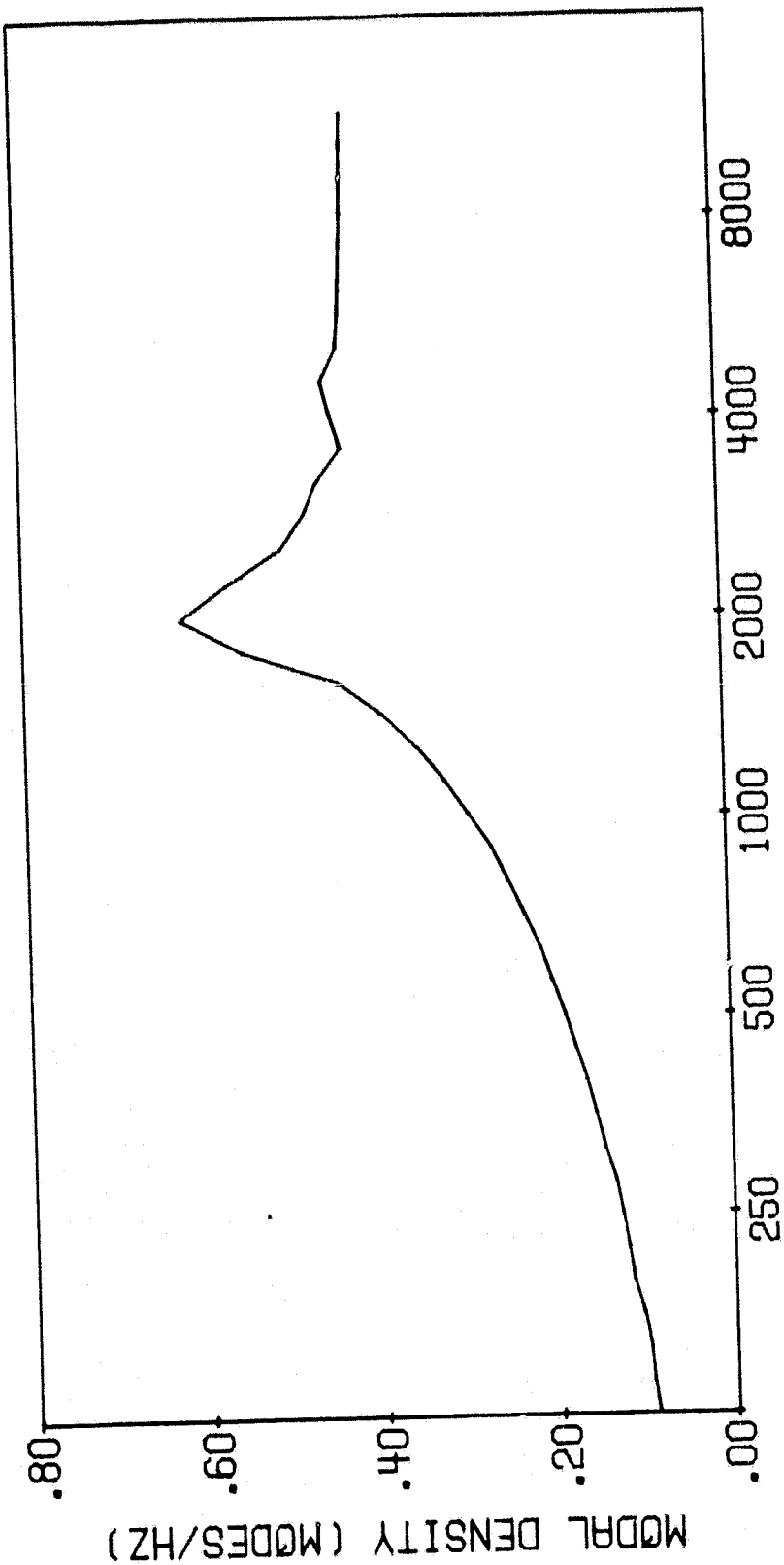

Fig. 2.3
Modal Density of the Cylindrical Shell.

2.2.3 Acoustically Fast and Slow Modes

Acoustically fast modes of a cylinder are defined as the modes for which both the longitudinal wavenumber and the circumferential wavenumber are less than the corresponding acoustic wavenumber. These modes play a key role in the sound radiation from the cylinder. On the other hand, the acoustically slow modes are those modes for which either the longitudinal wavenumber k_a and/or the circumferential wavenumber k_c are larger than the corresponding acoustic wavenumber k. Following this definition, the modes on the wavenumber diagram can be easily classified as either acoustically fast or acoustically slow as shown in Figure 2.4.

The radiation efficiency, which describes the relationship between the radiated power and the structure vibrational velocity is much higher for acoustically fast modes than that of acoustically slow modes. Usually, the radiation efficiency is unity for the acoustically fast modes. However, for the acoustically slow modes, where the circumferential wavenumber k_c is less than the accustic wavenumber k, while the longitudinal wavenumber k_a is greater than the acoustic wavenumber k, the edges aligned in the circumferential direction produce so-called edge modes. Because of the geometric constraints of the cylindrical shell, Manning and Maidanik observed that edge modes do not exist in the longitudinal direction [10]. For the same reasons, corner modes do not exist on a cylinder. Figure 2.4 shows a frequency band which

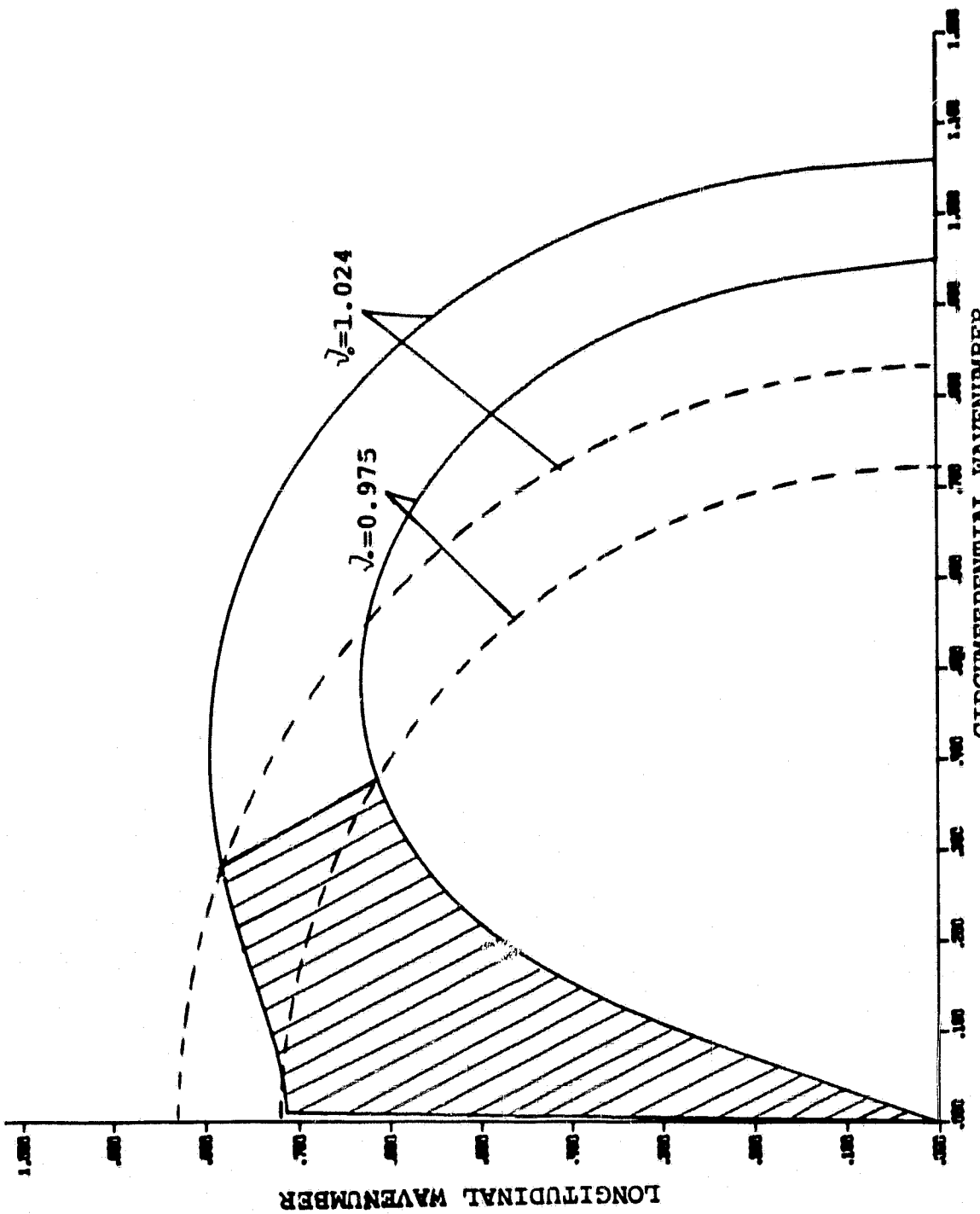

Fig. 2.4

A Frequency Band Consists of Some Acoustically Fast Modes and Some Acoustically Slow Modes; ——— Structural Waves, ----- Acoustic Waves; Shaded Area is Acoustically Fast Modes.

consists of some acoustically fast modes and some acoustically slow modes. Figure 2.5 gives two extreme cases, wherein, in the first case all the modes in a frequency band are acoustically fast as in Figure 2.5(a) and the other case in which all the modes are acoustically slow as shown in Figure 2.5(b).

2.2.4 Radiation Efficiency

The radiation efficiency indicates how efficiently sound is radiated from a structure to the acoustic field. It is defined as [11]

$$\sigma = \frac{P}{\rho_o c S \langle v^2 \rangle} \quad , \tag{2.10}$$

where P is the acoustic power radiated from the structure, $\rho_o c$ is the characteristic impedance of the air, S is the surface area, and $\langle v^2 \rangle$ is the spatially averaged mean-square velocity on the radiating surface.

The radiation efficiency of the modes resonant in a frequency band of interest varies as follows.

1. Is unity for a frequency band that includes solely acoustically fast modes.
2. For a band which has both acoustically fast and slow modes, the radiation efficiency may be assumed to be given approximately by the ratio of the number of acoustically fast modes to the total number of modes resonant in that band.

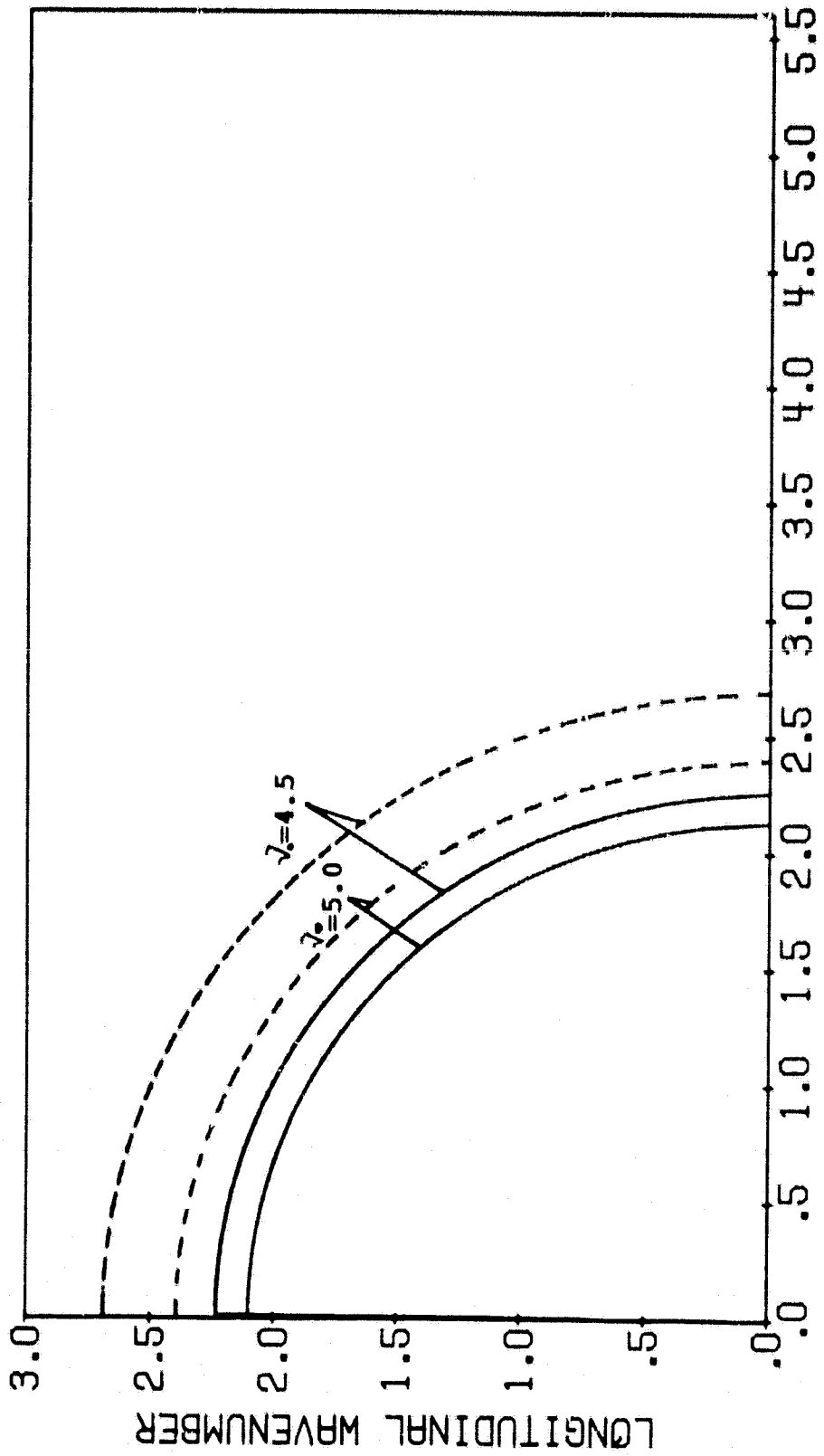

Fig. 2.5(a)
Frequency Band Consisting of Only the Acoustically Fast Modes.

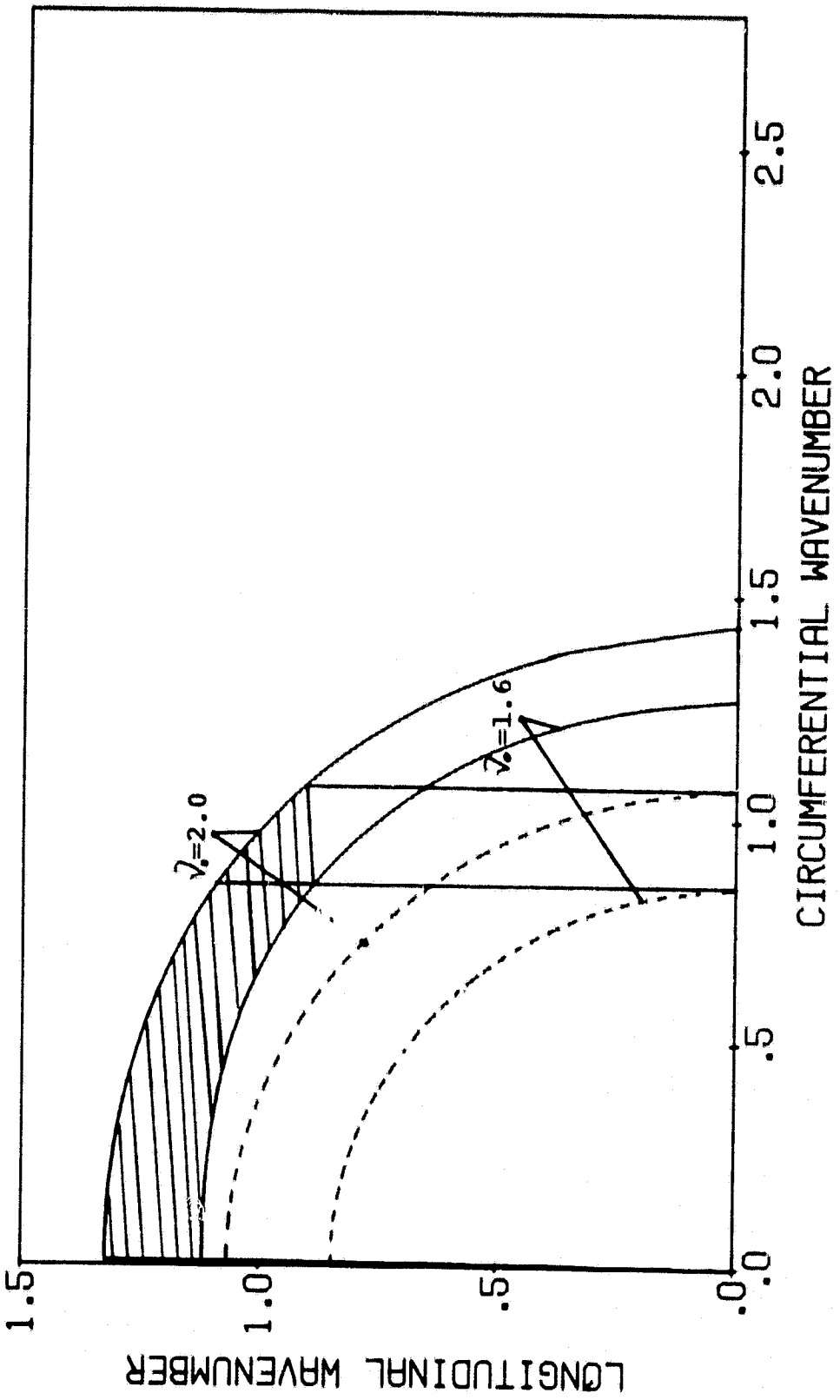

Fig. 2.5(b)

Frequency Band Consisting of Only the Acoustically Slow Modes. The Circumferential Edge Modes are Located in the Shaded Area.

3. For a band which has exclusively acoustically slow modes, the radiation efficiency for those modes (circumferential edge modes of the cylinder) is given by Szechenyi as [9]:

$$\sigma = \frac{(hR)^{1/2}\left[\ln\left[\frac{1+\left[f/f_c\right]^{1/2}}{1-\left[f/f_c\right]^{1/2}}\right] + 2\left[f/f_c\right]^{1/2}/\left[1-f/f_c\right]\right]}{\pi L\left[12\left[1-\mu^2\right]\right]^{1/4}\left[k_a^2+k_c^2\right]^{1/2}\left[1-f/f_c\right]^{1/2}} \quad , \quad (2.11)$$

where f is the frequency, f_c is the critical coincidence frequency, ln is the natural logarithm, and the other quantities are defined in earlier equations. The radiation efficiency of a cylindrical shell with the ring frequency at 2134 Hz and the critical coincidence frequency at 7452 Hz is plotted in the Figure 2.6. The radiation efficiency in Figure 2.6 is given in decibels with a reference value of 1.0.

2.3 The Sound Transmission Loss of a Cylinder

The study here of sound transmission loss through a finite cylindrical shell starts with the simplest case, wherein only the cylindrical shell is considered and diffraction at the ends is ignored. The sound transmission loss is then defined as

$$TL = 10\log\left[\frac{\text{Incident Acoustic Power}}{\text{Transmitted Acoustic Power}}\right]. \quad (2.12)$$

The sound transmitted through a structure can be divided into two parts; the resonant transmission and the non-resonant

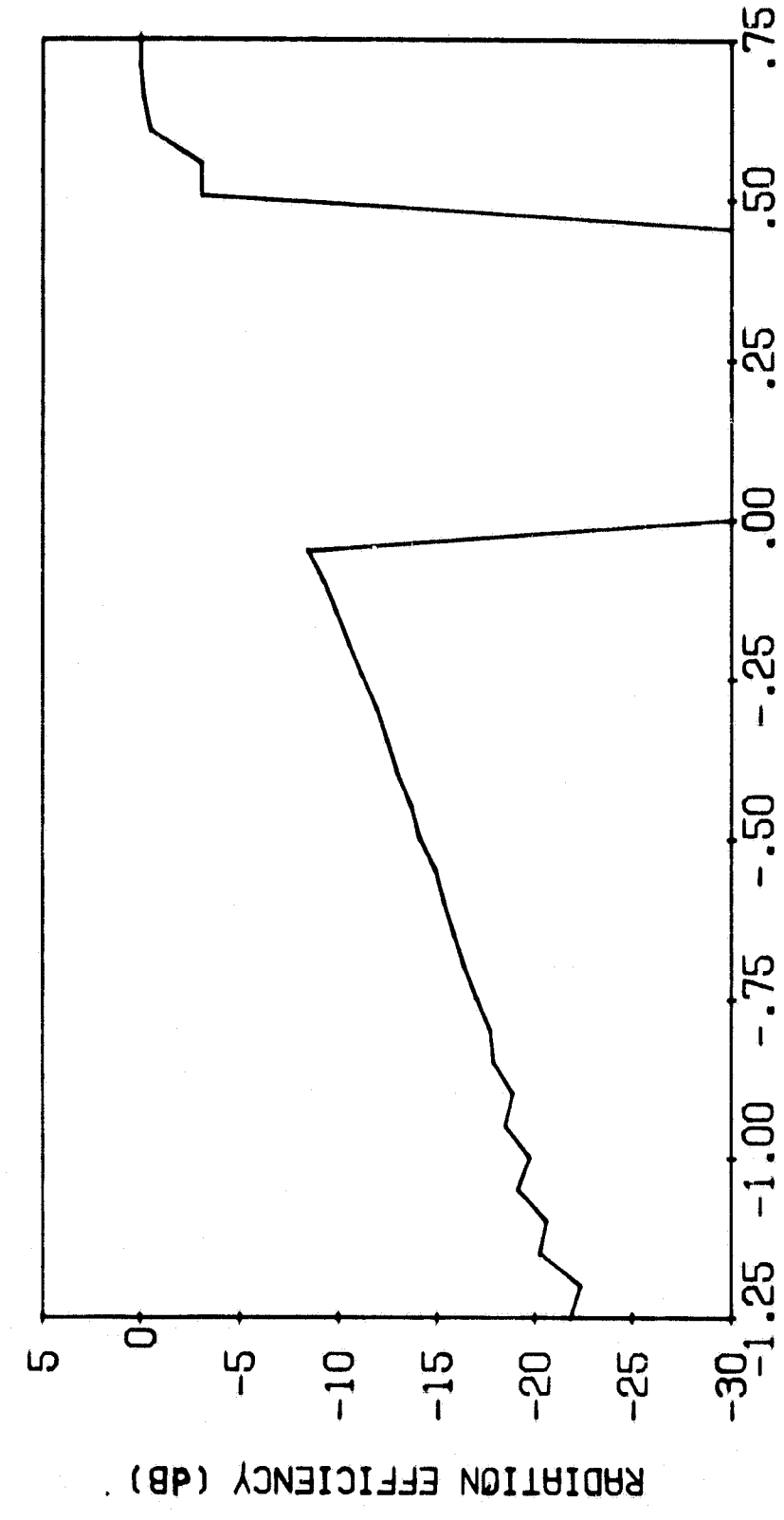

Fig. 2.6
The Radiation Efficiency of a Cylindrical Shell.

transmission. The non-resonant transmission dominates in the frequency range below the critical coincidence frequency, while the resonant transmission increases in importance at higher frequencies. The resonant transmission can be derived from the power balance equation as [13].

$$TL_{res.} = -10\log\left[\frac{8\pi^2 c^2\, n(\omega_o)\, R_{rad}^2}{\omega_o^2\, MS^2\left[2R_{rad} + R_{mech}\right]}\right], \qquad (2.13)$$

where $n(\omega_o)$ is the modal density in modes/Hz, R_{rad} is the average radiation resistance of all the modes resonant in the band under consideration ω_o is the center frequency (of the band), M is the mass of the cylinder per unit area, S is the radiating surface area, and R_{mech} is the mechanical resistance. The non-resonant vibration can be much more important at the frequencies where the resonant radiation properties are weak.

An incident acoustic wave forces any panel structure to vibrate off-resonance with a flexural wavelength equal to the acoustic trace wave length. Consider a structural mode with resonance frequency f_s having the same wavenumber components as those of the acoustic wave when incident on the structure (ie. same trace wavenumber vector.) This mode can be excited as follows [13].

(i) if $f_a > f_s$, the vibration amplitude (hence the transmission) is mass controlled, this response is said to be sub-coincident.

(ii) if $f_a = f_s$, the mode is excited at resonance and the response is said to be coincident.

(iii) if $f_a < f_s$ the vibration and transmission are stiffness-controlled and the response is said to be super-coincident.

Thus the non-resonant transmission for any incident acoustic wave is mass controlled if its frequency is greater than the natural frequency of the structural mode having the same coordinate wavenumbers, and stiffness controlled if the frequency is less than this natural frequency. In a diffuse incident sound field all the structural modes having wavenumbers k_a and k_c such that $k_a^2 + k_c^2 < k^2$ will be excited in non-resonant vibration [13]. The non-resonant modes of a cylindrical shell can be classified into mass controlled modes and stiffness controlled modes below the ring frequency because of the curvature effect. This is different from the case of a flat plate where the mass and stiffness controlled regions are easily defined, because all incident waves will be subcoincident for all frequencies up to the critical coincidence frequency. Although both represent non-resonant vibration, the mass controlled subcoincident waves are much superior to the stiffness controlled super-coincident waves in sound transmission. Accordingly, below the ring frequency, the non-resonant transmission calculation takes only the mass controlled modes into account though in that region both mass and stiffness controlled modes exist. For those frequencies above the ring frequency, since all the non-resonant modes are mass controlled, the non-resonant transmission is the same as that of a flat panel. In summary, the non-resonant transmission losses are given by the following two equations for the two frequency regions [13].

$$TL_{nr} = 8.33 \log\left[\left[\nu_o^2 (h/R)^2 \, E \, \rho_m / 4\rho_o^2 \, c^2\right] \left[1-\left[\nu_o f_r/f_c\right]^2\right]^2 + 2.3\right]$$

$$-3 + 20 \log\left[\pi/2 \sin^{-1}\left[\nu_o\left[1-\left[\nu_o f_r/f_c\right]^2\right]^{1/2}\right]^{1/2}\right], \quad (2.14)$$

for $\nu_o < 1$ (below ring frequency)

(2.15)

$$TL_{nr} = 8.33 \log\left[\left[\nu_o^2 (h/R)^2 E \rho_m / 4\rho_o^2 c^2\right]\left[1-\left[\nu_o \, f_r/f_c\right]^2\right]^2 + 2.3\right] - 3 \quad ,$$

for $\nu_o > 1$, (above ring frequency)

The total transmission loss of diffuse incident waves on the cylinder is the sum (in an energy sense) of the resonant and the non-resonant transmission loss. The transmission loss obtained theoretically in decibels versus frequency is shown in Figure 3.14.

2.4 Computer Programs and Discussion of the Theoretical Approach

Previous studies on the transmission of sound through cylindrical shells such as the work of Manning et al [10] and Szechenyi [8,9] utilized some approximations in obtaining the wavenumber diagrams. For example Szechenyi measured the areas in the wavenumber diagrams required for the evaluation of modal

densities with a planimeter and with several approximations. Whereas in the work reported here a series of computer programs have been developed to calculate the modal densities and the radiation efficiencies etc, from the wavenumber diagrams. These results are believed to be more accurate since the approximations made in earlier work have been avoided.

From Equation 2.9, for each given frequency ν_o, the locus ν_o is plotted on the wavenumber diagram with k_c and k_a as the axis and ordinate of the diagram respectively. A computer program has been developed to solve the following equation which is an expanded form of Equation 2.9:

$$k_a^8 + \left[4k_c^2\right]k_a^2 + \left[6k_c^4 + \nu_o^2 + 1\right]k_a^4 \qquad (2.10)$$

$$+ \left[4k_c^6 - 2\nu_o k_c^2\right]k_a^2 + \left[k_a^8 - \nu_o^2 k_a^4\right] = 0 \quad .$$

Three hundred values of k_c and the same number of values of k_a are calculated for every value of ν_o. In addition, the increment of ν_o has been chosen to be one-sixth of an octave. This results in a total of forty three different values of ν_o in the range from 0.05 to 6.4.

The surface area under a curve on the wavenumber diagram has been estimated by numerical integration. Whereas these areas have only been measured approximately in earlier work. Hence it has been possible to compute accurately these areas in the present work. Therefore, possible computation errors were minimized.

a. Szechenyi [9] made the assumption that $R_{rad}/R_{mech} << 1$ in the evaluation of the non-resonant transmission loss. Our experiments (described in the next section) suggest that this assumption was poor for some cylindrical shells. Hence the results in the present work were computed by taking into consideration the values of R_{rad} and R_{mech}.

b. Again in reference 9, the ratio of the number of mass-controlled modes to that of the total number of modes (required in the evaluation of modal density and radiation efficiency of the cylinder) has been evaluated by approximating the areas with the arcsine term in Equation 2.14. Whereas the ratio of the two wavenumber diagram areas have been evaluated by a numerical integration scheme through a computer program in the work reported here.

c. The calculation of radiation efficiency for those frequency bands containing some acoustically fast modes was carried out with computer programs without any approximation. Szechenyi [9] approximated the area of a frequency band in the wave number diagram to that of a triangle as shown in Figure 2.7. This assumption may cause larger errors for those cylindrical shells with a more curved shape.

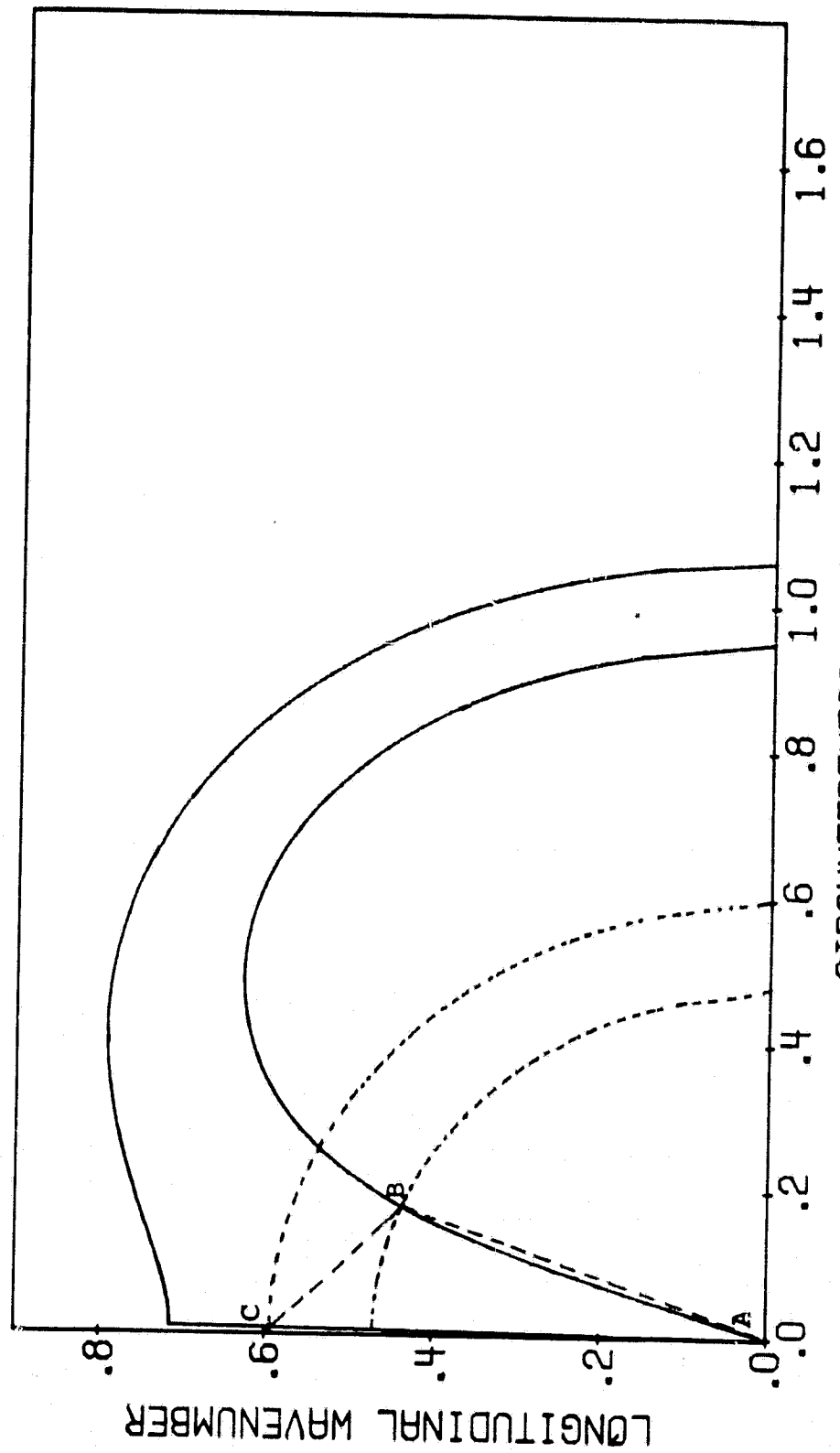

Fig. 2.7

Wavenumber diagram. Szechenyi [9] Approximated the Area of Acoustically Fast Modes in the Wavenumber Diagram by Taking It as a Triangle (ABC on the Figure)

3. EXPERIMENTAL INVESTIGATIONS

A cylindrical shell was designed to simulate a half scale model of a light aircraft fuselage. In Phase I of the study, the following series of experiments were conducted on the cylindrical shell assembly.

a. Measurement of the natural frequencies and modal density of the cylindrical shell.

b. Measurement of the internal loss factors of the cylinder.

c. Measurement of the interior sound intensity generated by a loudspeaker mounted inside the cylinder.

d. Measurement of the radiation efficiency of the cylinder.

e. Measurement of the sound intensity which is transmitted from the cylinder.

3.1 The Cylindrical Shell Assembly

The 0.762 m (30 inch) diameter cylindrical shell was built by rolling 1.6 mm (1/16 inch) thick sheet steel into circular shape and then welding it at the joint. Its length is 1.676 m (66 inches). The cylindrical shell has a pair of steel rings at both ends. Both the inner ring and the outer ring are 9.5 mm (3/8 inch) in width. After the cylindrical shell and the rings were assembled, the outer rings were fixed on two end plates. The end plates were made of 6.35 mm (1/4 inch) thick steel. This whole assembly as shown in the Figure 3.1 was suspended from the ceiling in the anechoic chamber with two chains during the experiments.

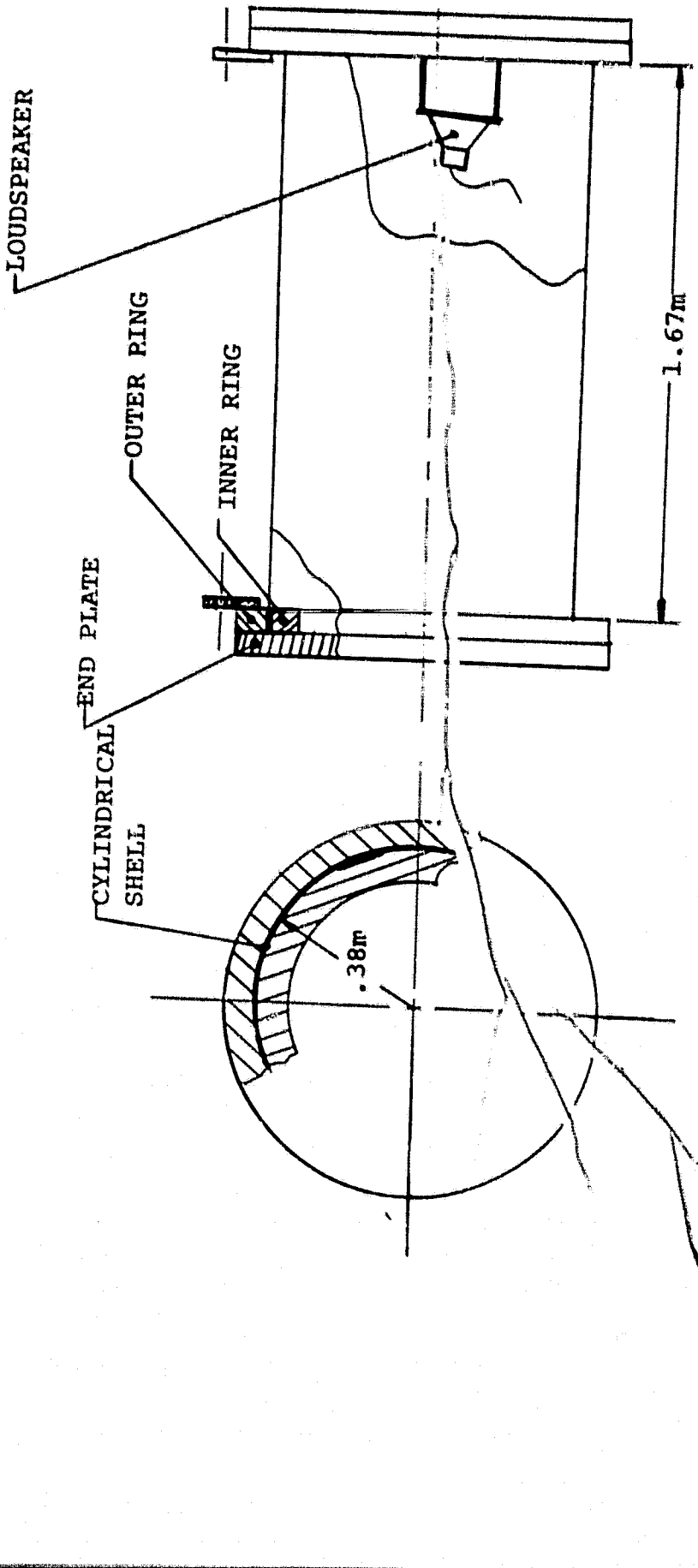

Fig. 3.1
The Cylinder Assembly.

3.2 The Natural Frequencies

The natural frequencies of the cylinder were measured by an accelerometer in conjunction with a force transducer. The natural frequencies were obtained by observing the peaks of the mobility curve and the zero crossing of the phase plot of the curve simultaneously. The mobility is the transfer functions between input force and response velocity. Both the impact method (using the hammer) and the impedance head method (using a shaker) were utilized in the measurements. Table 3.1 shows a comparison of the first ten natural frequencies obtained theoretically and those obtained by the two experimental approaches. The two experimental results compared very well with each other while the theoretical predictions (Equations 2.4) were different by a few hertz. However, as far as the modal density is concerned, the theory and the measurements matched very well. Figure 3.2 shows the mobility curve acquired from the impact method.

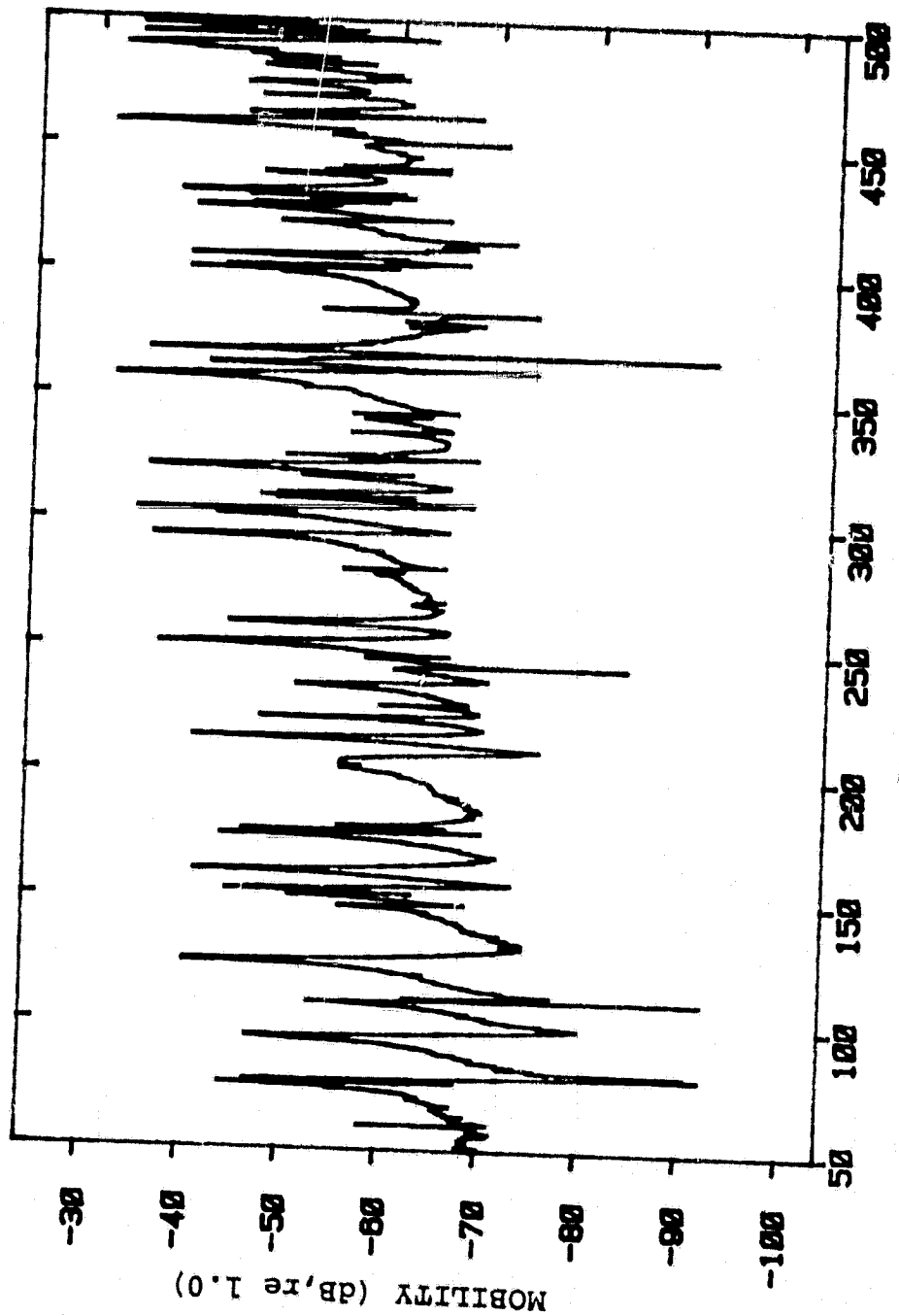

Fig. 3.2
Cylinder Mobility Obtained by the Impact Method from 50 Hz to 500 Hz.

Table 3.1
FIRST TEN NATURAL FREQUENCIES

Mode m	Number n	Calculated Frequency (Hz)	Measured Frequency (Hz)	
			Impact Method	Impedance Head Method
1	4	79.9	75.8	74.4
1	5	81.0	77.4	77.6
1	6	102.8	94.8	94.6
1	3	118.0	109.0	110.6
1	7	135.2	124.8	124.6
2	6	154.2	151.4	151.2
2	7	162.1	161.2	161.2
1	8	174.6	172.0	169.6
2	5	177.7	177.6	177.8
2	8	189.8	179.4	179.4

3.3 The Damping Loss Factor

A knowledge of the damping loss factor is most essential in SEA theory. Three related parameters are widely used to indicate the damping character of structures. They are the damping loss factor η_{mech} the reverberation time T_R, and the critical damping ratio ζ [14]. The relationships between these measures are:

$$\zeta = (1/2)\eta_{mech} , \tag{3.1}$$

and

$$T_R = 2.2/f\eta_{mech}. \tag{3.2}$$

3.3.1 Difficulties In Damping Measurements

Damping measurement can be classified into two main approaches, (1) the steady state method and (2) the decay rate method. The steady state method uses the concept of energy flow balance. The steady state method was not used in this project. The decay rate method, which was adopted in this investigation employs a level recorder to record the decay in vibration of the structure when the exciting force is suddenly shut off. Because this is a widely used method, no details of the measurement procedure will be explained here. However, the difficulties involved in measuring the decay rate are listed as following:

a. It is quite subjective as to where to draw a straight line on the recorded paper strip, since the recording usually consists of a considerable number of "ripples."

b. For an extremely highly damped structure, the paper speed must be extremely high if the decay rate is to be obtained accurately.

c. The experiments have to be repeated several times in order to get repetitive measurements. This is a time consuming process and hence a major disadvantage.

3.3.2 Damping Measurements Using the FFT

By applying similar ideas, the conventional decay rate method can be very much improved by using a high sampling rate A/D converter. The HP5451C Fast Fourier Analyzer has sampling rate available as frequently as every five micro-seconds. In addition, data can be processed directly on the machine by using Fortran programs. These features make the FFT a very powerful tool in decay rate measurements.

The acceleration decay curve from an accelerometer attached to the structure can be expressed mathematically as [15]

$$A(t)=Ct+b+n(t), \tag{3.3}$$

where A(t) is the acceleration level in decibels, t is the time. C and b are constants, n(t) is the "noise" signal representing the flutter in the decay. The decay rate C, can be determined by estimating (C) in such a way that n(t) becomes a noise component with zero mean. Hence the integral of n(t)dt with respect to t is eliminated. Equation 3.3 is thus reduced to

$$\int_0^t A(t)dt = \frac{C}{2} t^2 + bt \quad . \tag{3.4}$$

Both Figures 3.3 and 3.4 illustrate the procedures explained above.

Based on the assumption that the acceleration level decays exponentially, the decay rate in decibels/sec is the constant C in Equation 3.3. Therefore, the decay rate can be obtained either by choosing any two points on the Figure 3.4 or by fitting the curve with least square error to Equation 3.4. On the FFT, searching for the best estimate of the constant C is carried out by a Fortran program.

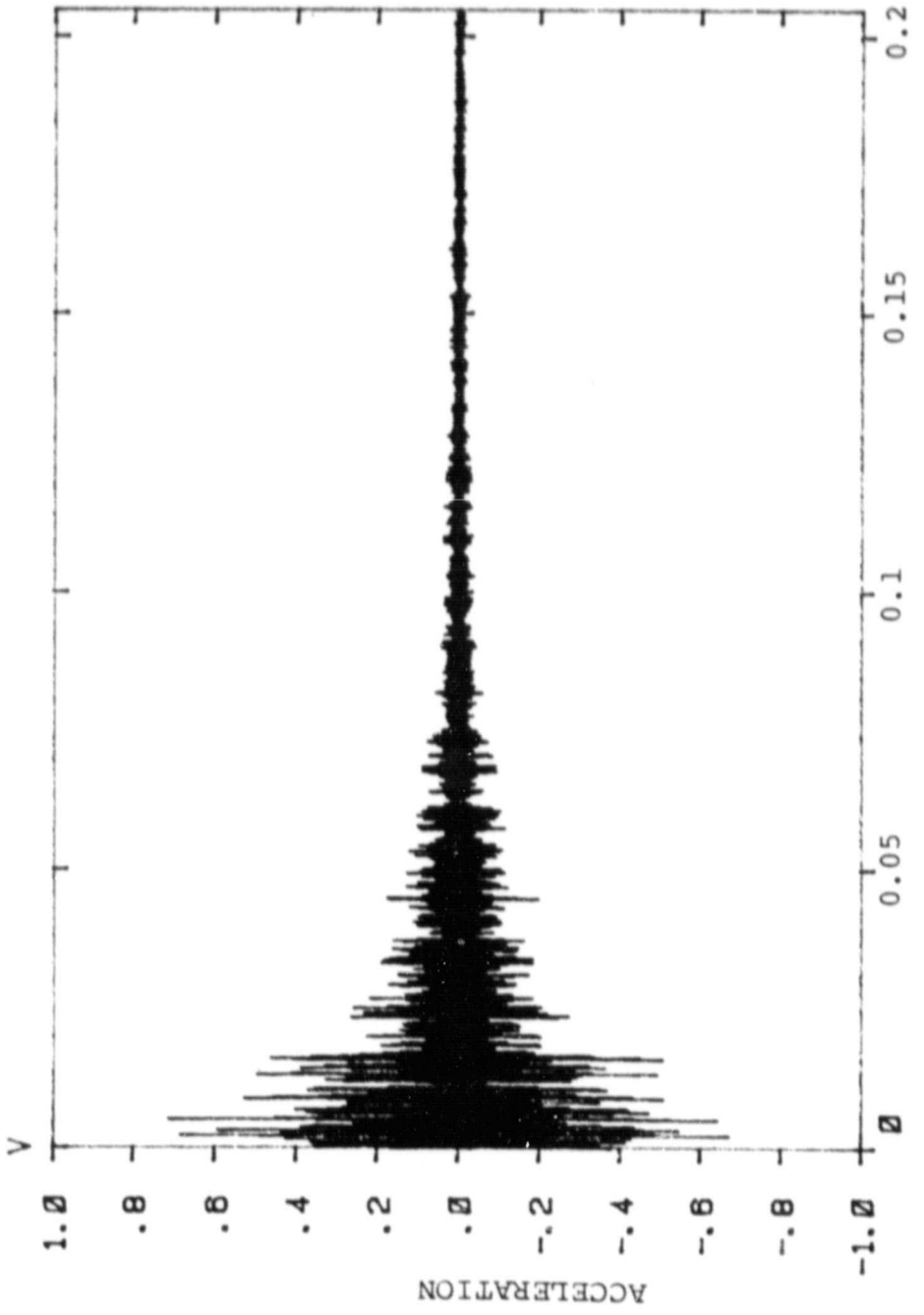

Fig. 3.3
The Acceleration Level Decay in the Time Domain.

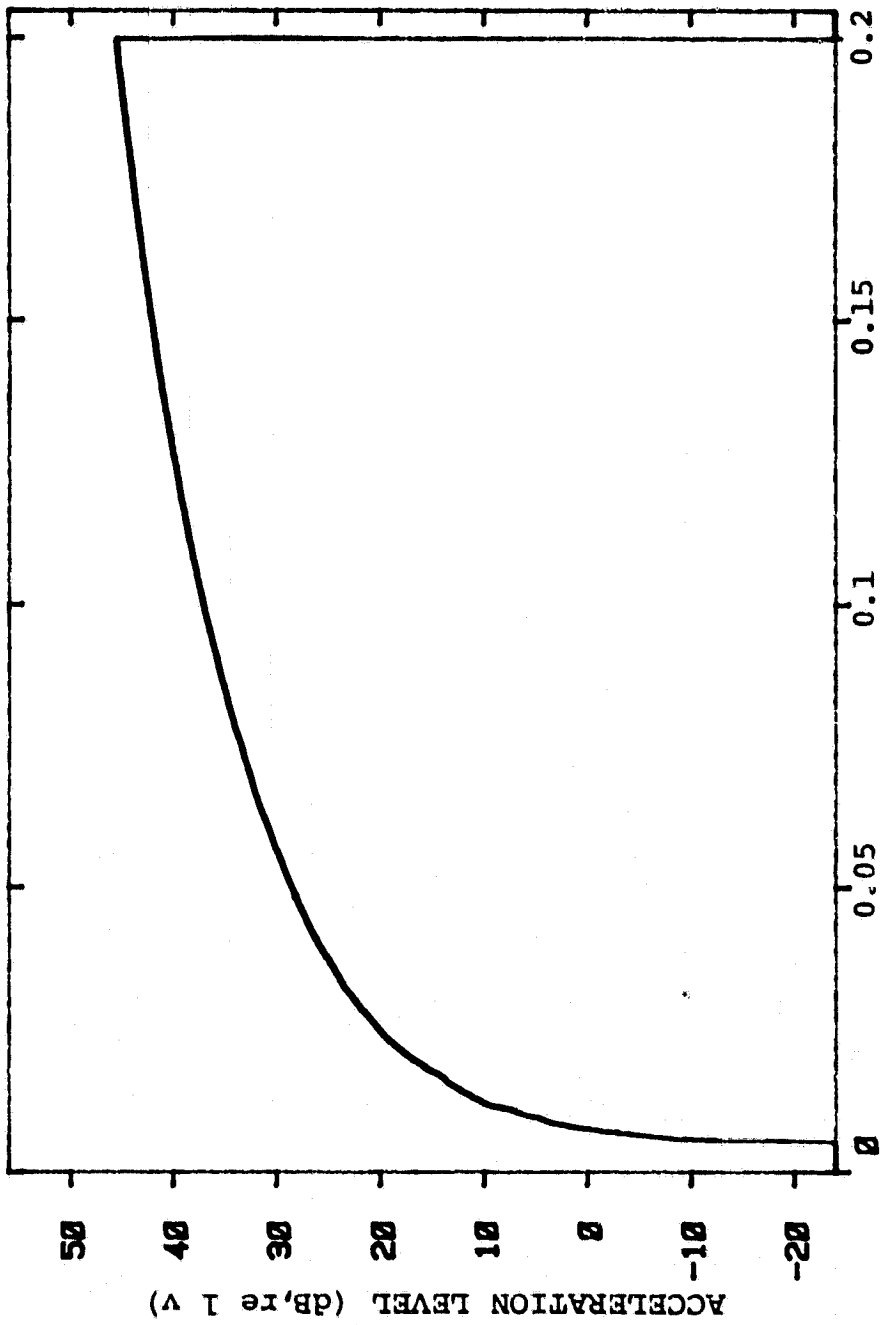

Fig. 3.4
The Result of Integrating the Acceleration with Respect to Time.

This improved method of measurement of the decay rate has proved reliable and time-saving. This method has been used to verify the reverberation time measurements of the reverberation room in the Herrick Laboratories. The results obtained by this new method compared well with those obtained by the conventional method in most frequency ranges [16]. There seems to be some slight disagreement in the high frequency range between these two types of measurements [16].

3.3.3 Damping Loss Factor of the Cylinder

Figure 3.5 is the schematic diagram of the instrumentation used for damping measurements. The white noise signal is generated by a B&K 1024 Sine-Random Signal Generator, and then fed through a B&K 2112, One-Third Octave Filter. This signal amplified by a Phase Linear Amplifier is supplied to a shaker to drive the cylinder at a point. The output acceleration signal is picked up by a B&K 4344 accelerometer. After amplification, this signal is fed through a B&K One-Third Octave Filter to the A/D converter of the FFT. A 6V battery provides an external triggering source to the FFT through a double switch. Whenever the noise source is cut off, by means of the switch the FFT starts to trigger.

The damping loss factors of the cylindrical shell under

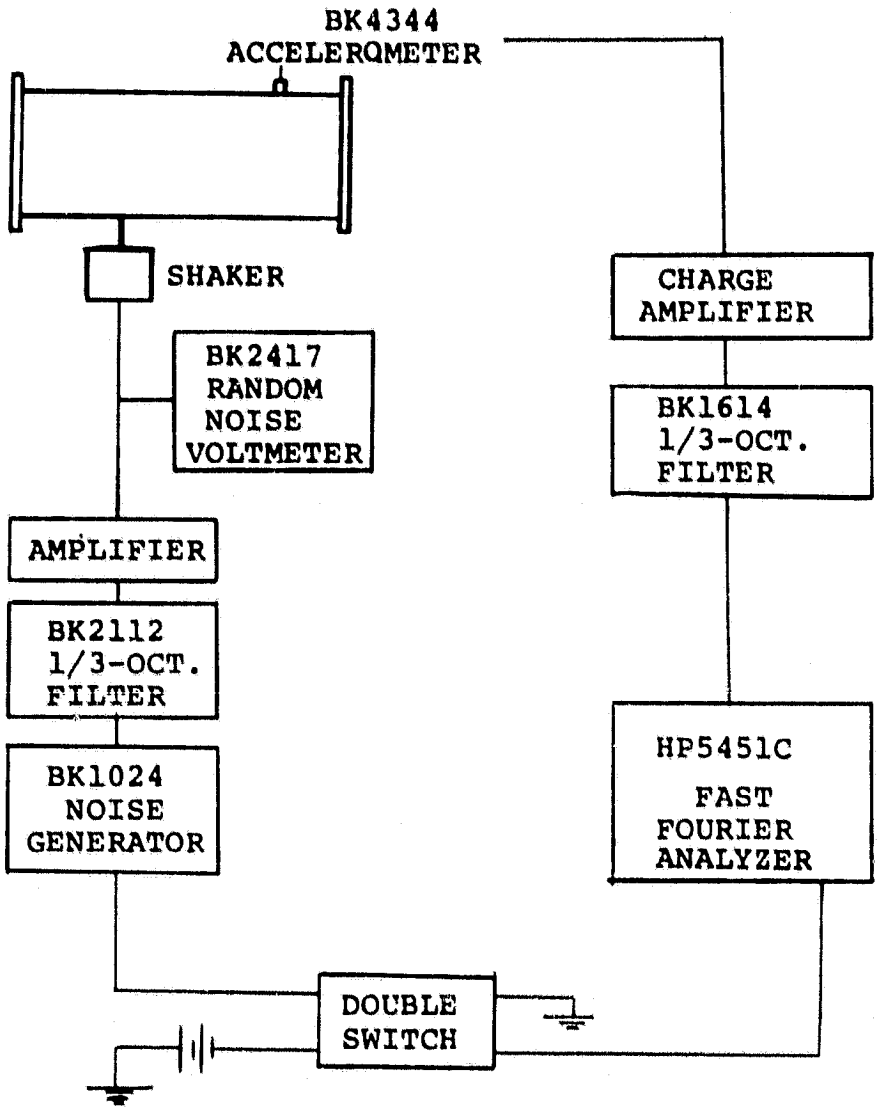

Fig. 3.5

Schematic of the Experimental Set Up for the Damping Measurement.

investigation were measured in each one-third octave frequency band. Table 3.2 shows the results.

Table 3.2
THE DAMPING LOSS FACTORS OF THE CYLINDRICAL SHELL

Center Frequency (Hz)	Decay Rate (dB/sec)	Damping Loss Factor
100	12.71	0.00466
125	12.38	0.00363
160	11.98	0.00274
200	12.58	0.00230
250	9.15	0.00134
315	11.25	0.00131
400	12.69	0.00116
500	14.59	0.00107
630	14.13	0.00082
800	19.69	0.00090
1000	33.87	0.00124
1250	38.47	0.00113
1600	36.79	0.00084
2000	71.15	0.00130
2500	66.78	0.00098
3150	52.14	0.00061
4000	50.49	0.00046
5000	67.73	0.00050
6300	74.67	0.00043
8000	184.54	0.00084
10000	373.53	0.00137
12500	427.11	0.00125
16000	391.47	0.00090

3.3.4 The Radiation Losses

The loss factor measured using the decay technique discussed in the previous section is the total loss factor and includes the damping losses as well as the radiation losses of the structure. Hence the true internal loss factor should be obtained by subtracting the radiation loss factor from the total loss factors.

In most panel studies, the radiation losses turn out to be very low compared to the total damping losses in the range below the critical frequency [17,19,20]. This is mainly because the panel is heavily damped at the boundaries for either clamped or simply supported conditions. However, an examination of the total loss factors, as given in Table 3.2, leads to the conclusion that the cylindrical shell under investigation is not a heavily damped structure. Therefore, the radiation loss should be subtracted from the total loss factor so as to obtain the correct internal loss factor.

The radiation loss factor η_{rad} is defined as

$$\eta_{rad} = \frac{\rho_o c \sigma}{\omega M} , \qquad (3.5)$$

where σ is the radiation efficiency given by Equation 2.10, and M is the surface density in kg/m^2. The measurement of the radiation efficiency is discussed in Section 3.4.2.

Table 3.3
INTERNAL LOSS FACTORS OF THE CYLINDER

Center Frequency (Hz)	Total Loss Factor	Radiation Loss Factor	Internal Loss Factor
100	0.00466		0.00466
125	0.00363		0.00363
160	0.00274		0.00274
200	0.00230		0.00230
250	0.00134	0.000420	0.00092
315	0.00131	0.000840	0.00047
400	0.00116	0.000332	0.00083
500	0.00107	0.000265	0.00080
630	0.00082	0.000337	0.00048
800	0.00090	0.000265	0.00063
1000	0.00124	0.000335	0.00090
1250	0.00113	0.000238	0.00089
1600	0.00084	0.000166	0.00067
2000	0.00130	0.000419	0.00088
2500	0.00098	0.000134	0.00085
3150	0.00061	0.000030	0.00031
4000	0.00046	0.0000167	0.00044
5000	0.00050	0.0000127	0.00049
6300	0.00043	0.0000150	0.00042
8000	0.00084	0.0000105	0.00082
10000	0.00137	0.0000042	0.00013

3.4 Sound Intensity Radiated From the Cylinder

A 15 watt, double coned loudspeaker was mounted, on brackets six inches away from the endplate, at one end of the cylinder. It was oriented toward the end plate and was mounted eccentric to it. After a steady sound field was produced inside the cylinder, the sound intensity transmitted through the cylindrical shell was measured by sweeping the combination of two microphones over the surface of the cylinder. The intensity measurement is shown in Figure 3.6 (a). The instrumentation used for the transmission loss measurements is shown in Figure 3.6 (b).

Fig. 3.6a Acoustic Intensity Measurement on the Cylindrical Shell.

Fig. 3.6b Instrumentations for the Acoustic Intensity Measurements

3.4.1 Two Microphone Intensity Measurement

The use of the combination of two microphones for the measurement of acoustic intensity has been discussed in Part 1 of this report. In this study, three different microphone spacings, 6.35 mm, 12.7 mm, and 25.4 mm, were employed in order to produce satisfactory results at both high and low frequencies. For all the measurements, the signal-to-noise ratios were carefully checked. These ratios varied from 25 dB at low frequencies to more than 50 dB at high frequencies.

3.4.2 Radiation Efficiency

As discussed in the section 2.2.4, the radiation efficiency, can be determined by measuring the velocity of the vibrating structure and the power radiated by it. In this investigation, the spatially averaged velocity is taken at 60 randomly distributed locations over the cylindrical shell. Simultaneously the sound power radiated was measured with the two-microphone intensity method. The results of the radiation efficiency were analyzed in both narrow and one-third octave bands. Figure 3.7 presents the narrow band analysis over a frequency range of 0 Hz to 10000 Hz. Figure 3.8 exhibits a comparison between the theoretical predictions (Sec. 2.2.4) and the experimental results of the radiation efficiencies for one-third octave center frequencies. The agreement seems to be fairly good.

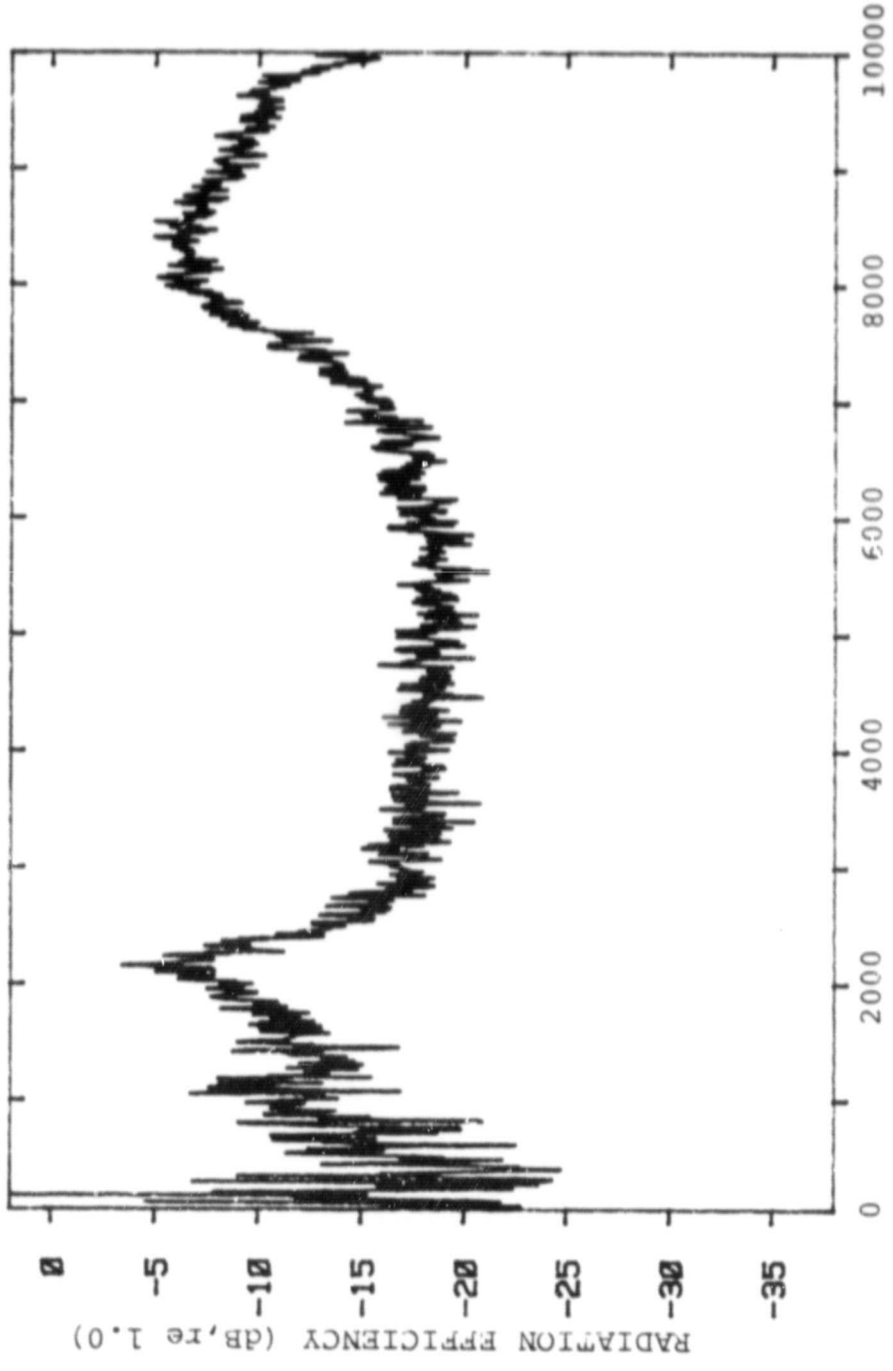

Fig. 3.7
Measured Radiation Efficiency of the Cylindrical Shell.

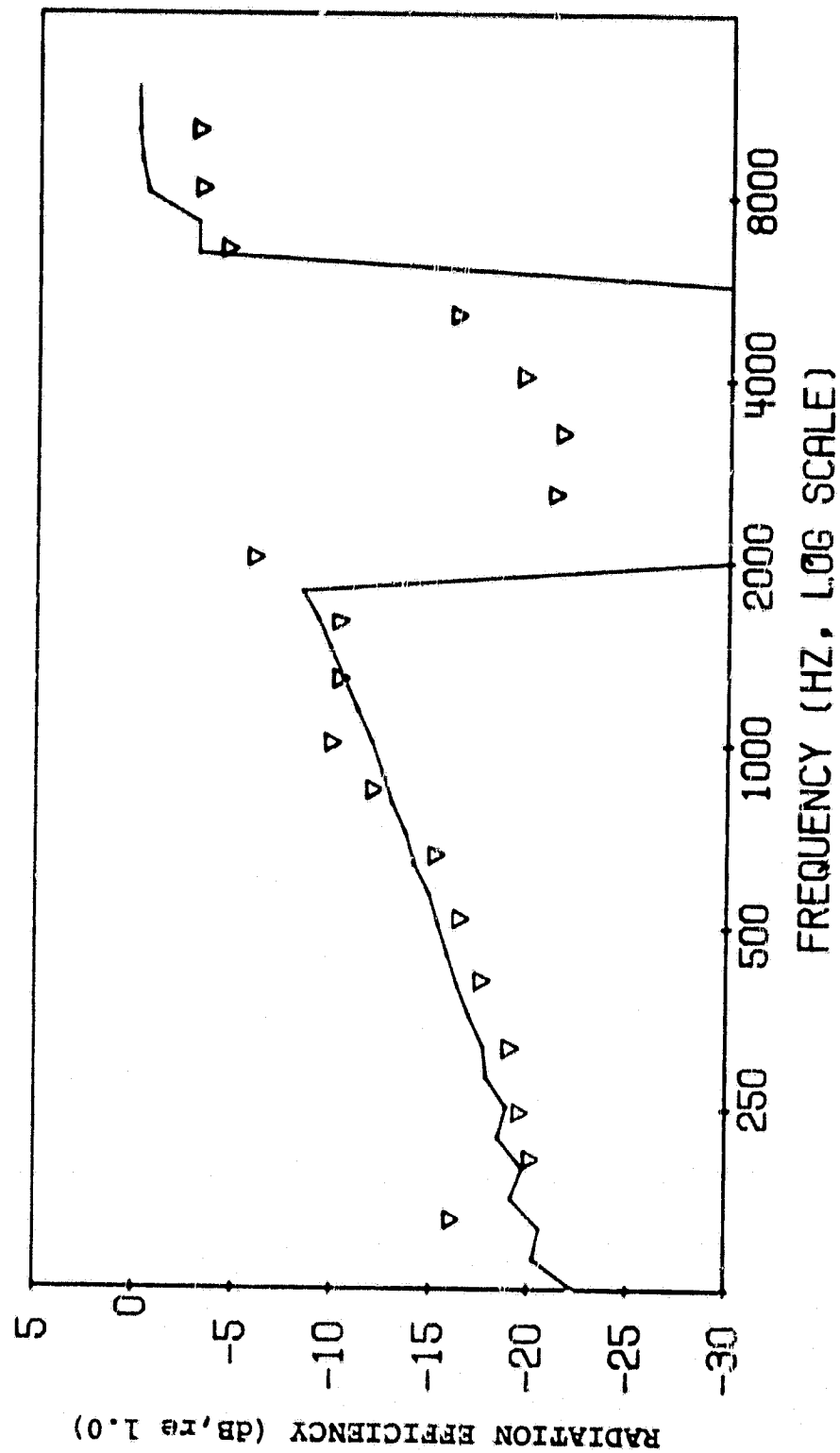

Fig. 3.8
Comparison between Theoretical Predictions of Radiation Efficiencies and the Measured Results (in One-Third Octave Center Frequencies, Marked as ▽).

3.5 Sound Transmission Through the Cylindrical Shell

As explained in the project proposal [18], attention is focused in this project on techniques to determine the sound transmission through an aircraft fuselage. In phase 1 of the study, emphasis is placed on the sound transmission through a cylindrical shell.

Traditionally, the transmission loss of a structure is determined from the noise reduction with associated corrections for the area of the structure and the absorption in the receiving space. In order to evaluate the transmission loss, usually some complicated testing procedures and mathematical calculations are needed. Moreover, the basic assumption of two reverberant fields in the measurement, required either a pair of costly reverberation rooms or sacrifice of measurement accuracy. Now, the measurement of transmission loss is completely simplified by the two- microphone intensity method [12].

The sound field inside the cylinder is generated by a loudspeaker placed inside the cylinder. As generally known, the sound pressure is distributed unevenly in the low frequency range. In other words, there exists some standing waves. Among them, the first two longitudinal modes at 100 Hz and 200 Hz and the first two cross modes at 265 Hz and 439 Hz tend to have high amplitudes at their resonance frequencies. Around these modal frequencies (mainly below 500 Hz), the modal densities are too low to build up a diffuse field. Hence the assumption that it is

a diffuse sound field inside the cylinder may cause a large discrepancy in the results in the low frequency region. In order to obtain a good spatially averaged sound pressure level, a bent microphone probe is moved both longitudinally and circumferentially inside the cylinder during the sound level measurements. Table 3.4 shows the spatially averaged sound level (from 300 samples) and the sound level at two arbitrarily picked points inside the cylinder. The agreement between the three measurements at high frequencies suggests that the sound field is indeed quite diffuse.

Table 3.4
SOUND PRESSURE LEVELS OF TWO FIXED POINTS INSIDE THE CYLINDER COMPARED TO THE SPATIALLY AVERAGED SOUND PRESSURE LEVEL

Frequency (Hz)	L_p at Point A	L_p at Point B	L_p Spatially Averaged
63	61.3	63.0	66.9
80	67.7	75.6	72.7
100	87.3	83.5	89.6
125	74.9	75.9	77.8
160	65.3	67.5	71.6
200	78.7	87.9	86.2
250	79.8	77.3	77.5
315	92.5	92.8	90.8
400	98.0	95.9	95.9
500	94.9	97.2	98.3
630	96.0	98.9	99.6
800	100.3	101.7	100.1
1000	102.1	103.5	104.4
1250	104.7	106.6	105.5
1600	100.7	102.8	102.4
2000	99.9	99.9	99.9
2500	97.8	95.9	96.9
3150	103.4	103.6	103.9
4000	100.1	101.8	101.3
5000	97.1	94.9	95.6
6300	96.1	97.2	96.9
8000	95.7	96.4	96.8
10000	88.7	90.0	90.9

3.5.1 Sound Intensity Radiated to the Exterior of the Cylinder

The sound intensity transmitted through the cylinder was measured by the two microphone technique on the exterior surface of the cylinder. It is of interest to compare the sound radiated from different sections of the cylinder surface area. Figure 3.9 shows the effect of variation of loudspeakers location. Areas #1 and #12 shown in the figure are located at two opposite ends of the cylinder. The loudspeaker was installed near the area #12.

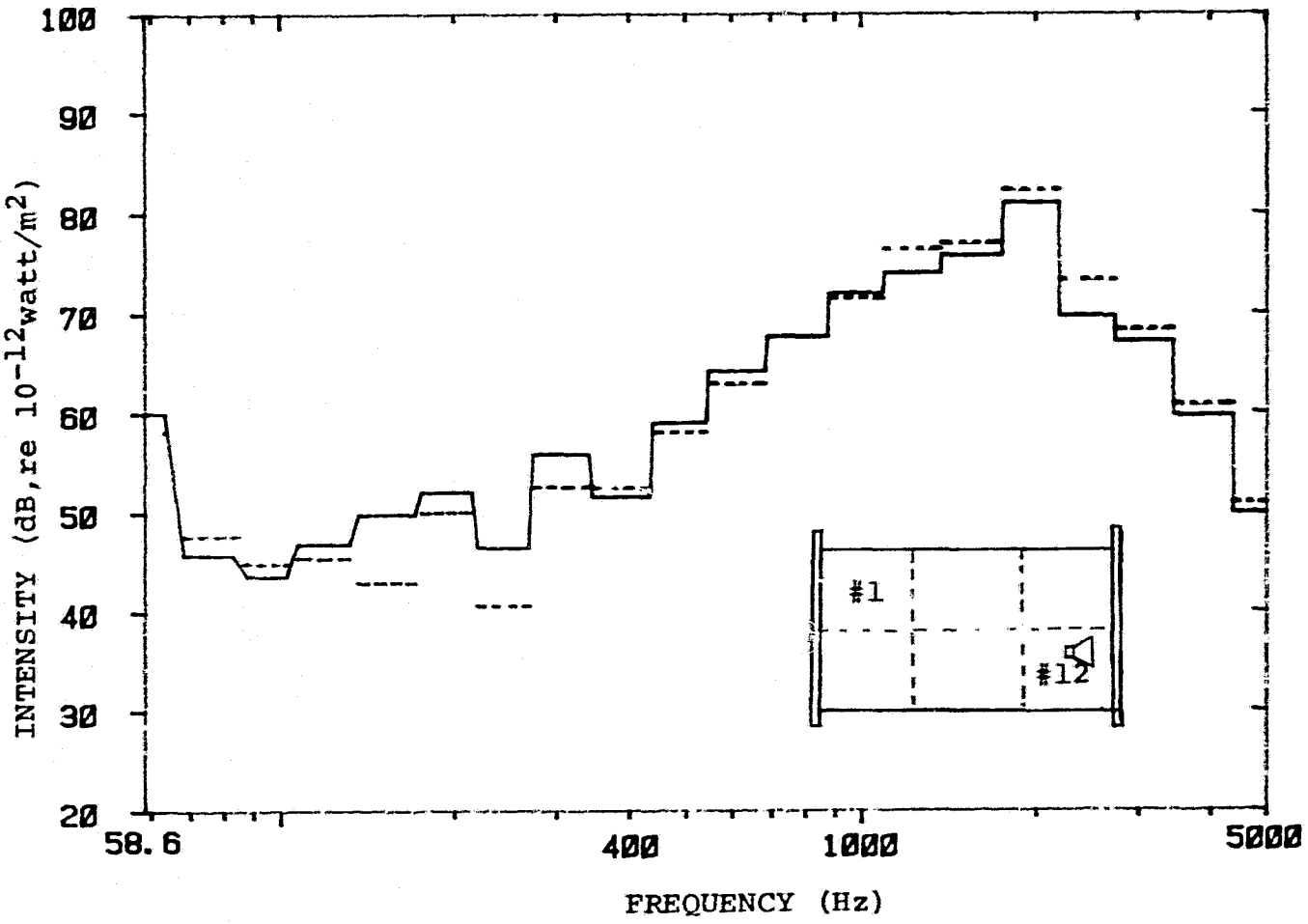

Fig. 3.9

Sound Intensity Radiated from Different Sections of Cylindrical Shell;
---- Section #1, —— Section # 12.

Differences are found in the low frequency range whereas little discrepancy is noticeable at high frequency. Secondly, the edge effect is presented in Figure 3.10. Area #1 has one edge clamped by two rings while area #2 is not clamped along any edge. From the figure, the transmitted intensity seems to be little affected by boundaries. Thirdly a comparison of sections with and without a welding joint was made. The area #8 which consists of a welding joint seems to radiate less power than the area #2 which is without the welding joint. This is illustrated in Figure 3.11.

3.5.2 Sound Transmission Loss

The sound transmission loss is calculated by ten times the logarithm of the ratio of the incident intensity to the transmitted intensity. Under an assumption that the interior sound field is diffuse, the incident intensity can be calculated from $p^2/4\rho_o c$. The transmission loss is then obtained from these intensity levels. Figures 3.12 and Figure 3.13 show the transmission loss of the cylindrical shell in a narrow frequency band and in one-third octave averages respectively.

The experimental results are compared with the theoretical transmission loss predictions in Figure 3.14. The theory agrees

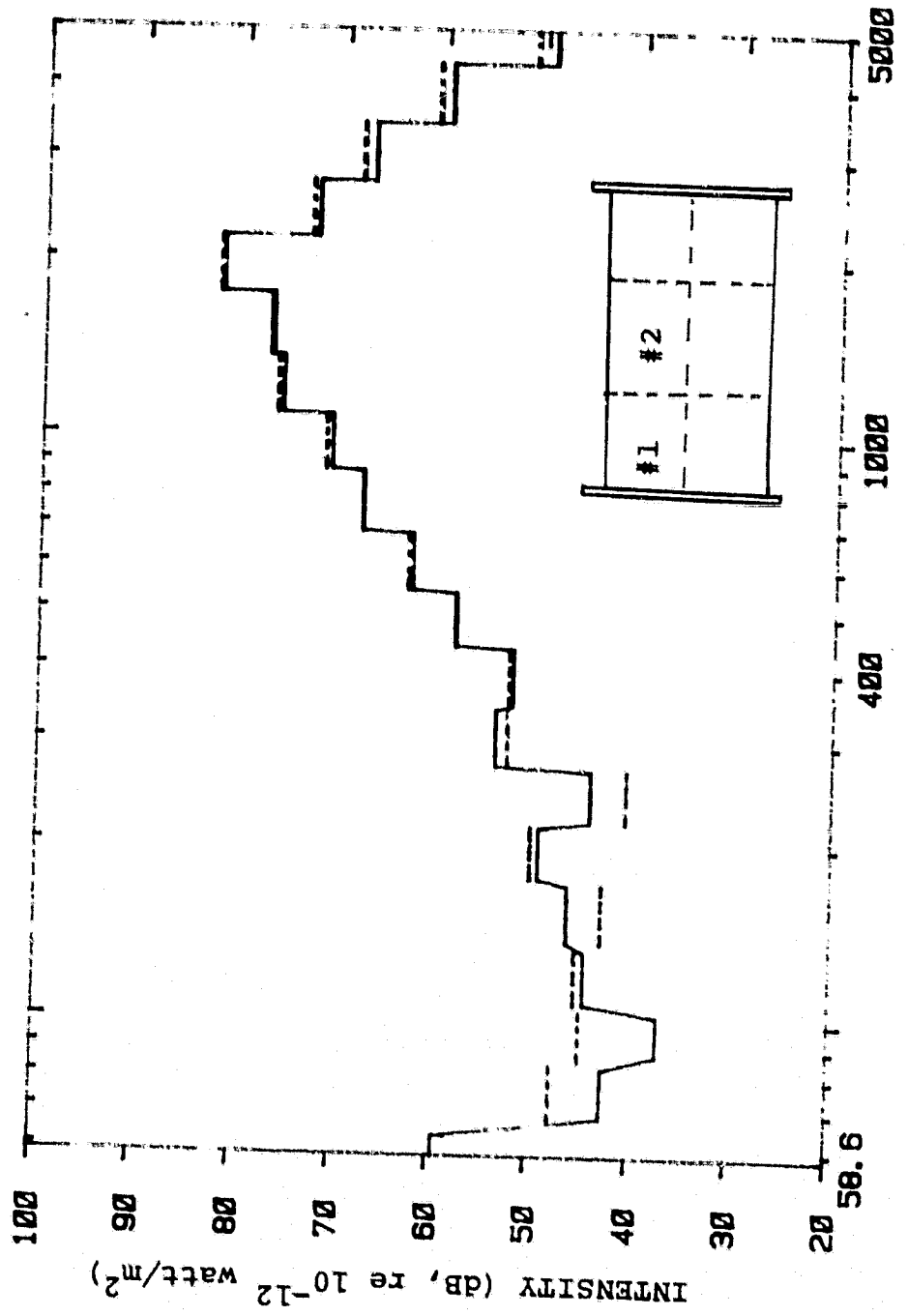

Fig. 3.10

Sound Intensity Radiated from Different Sections of Cylindrical Shell;
---- Section #1, —— Section #2.

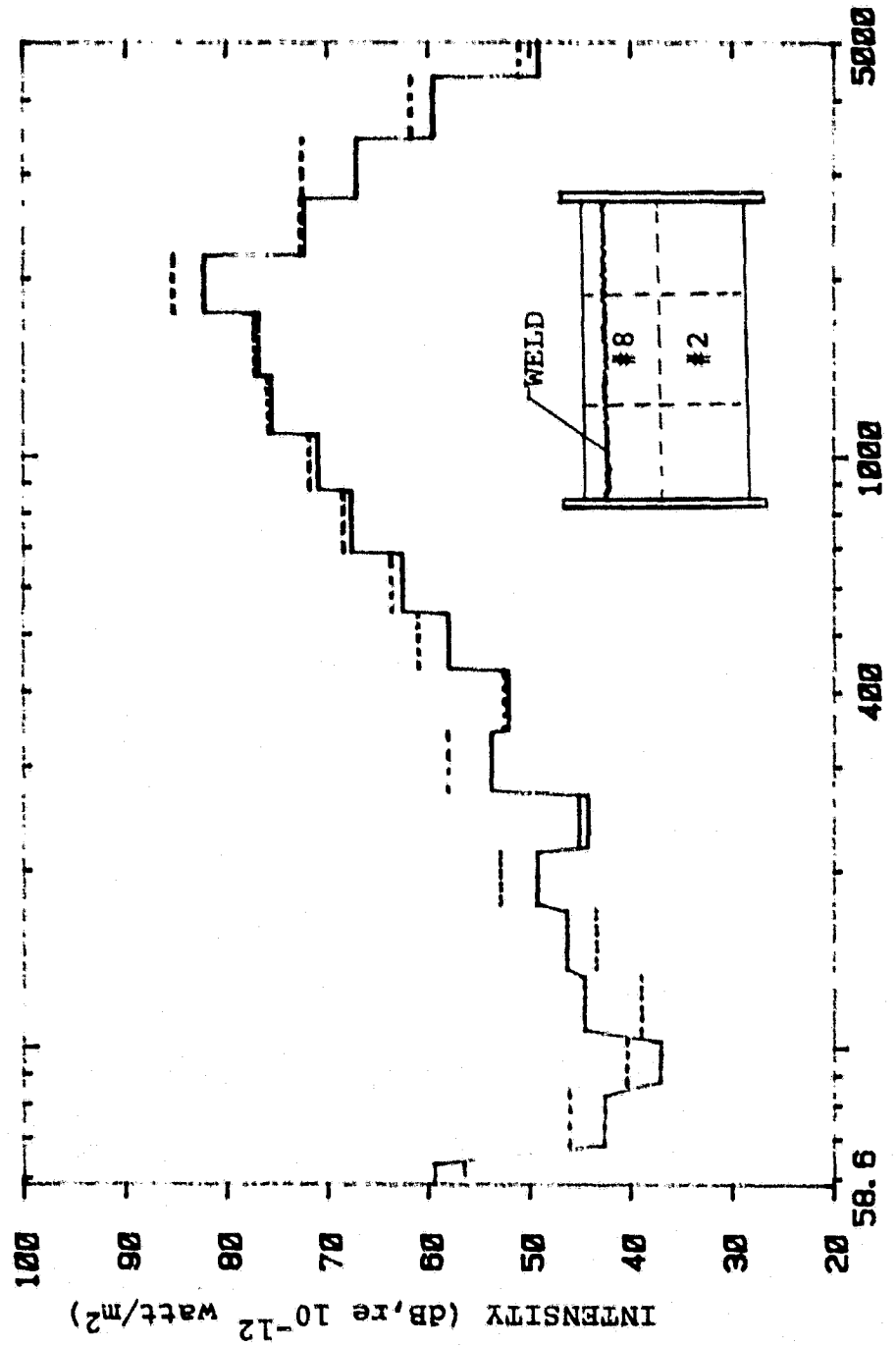

Fig. 3.11
Sound Intensity Radiated from Different Sections of Cylindrical Shell; ---- Section #2, —— Section #8.

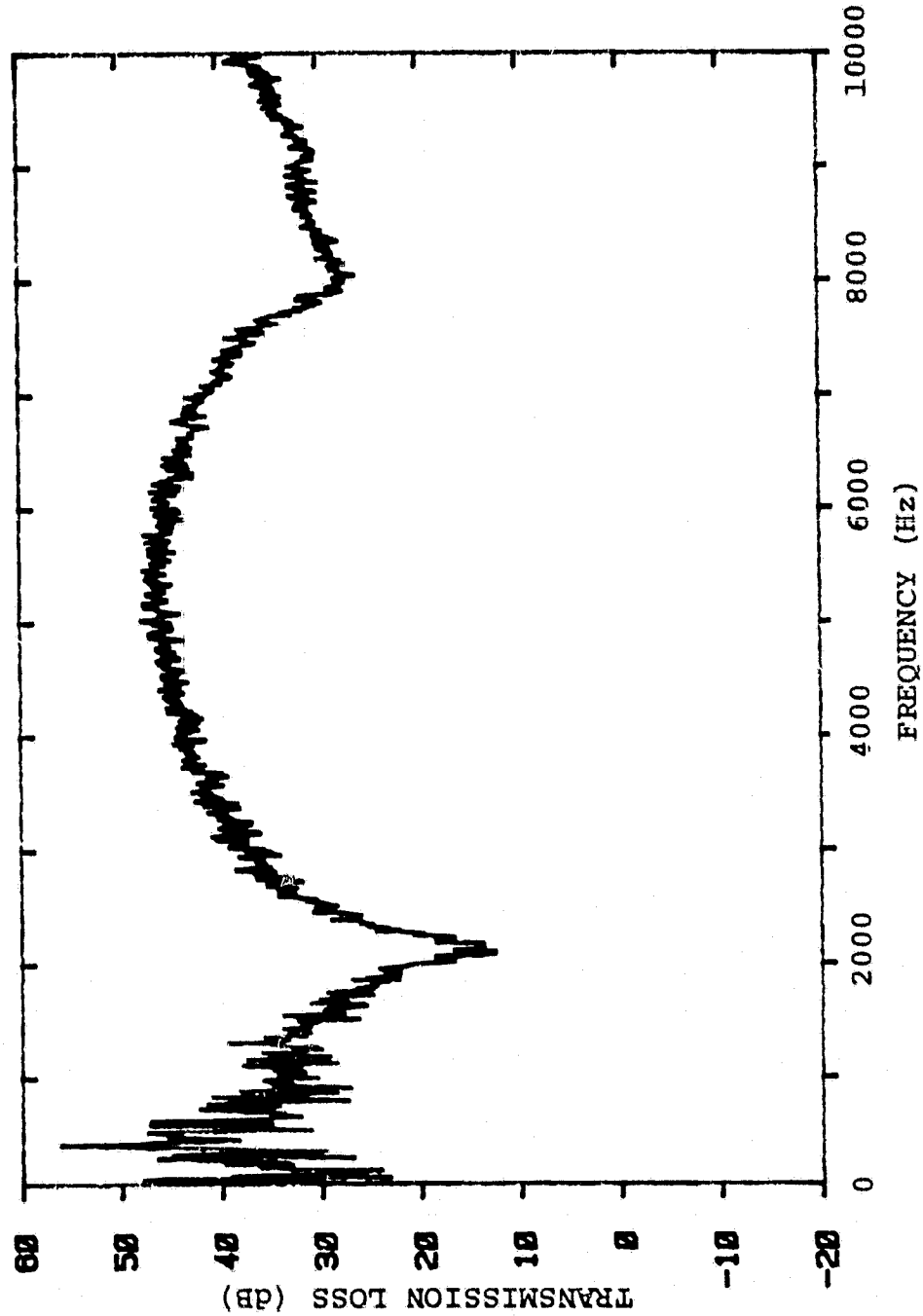

Fig. 3.12
Transmission Loss of the Cylindrical Shell in Narrow Band Analysis.

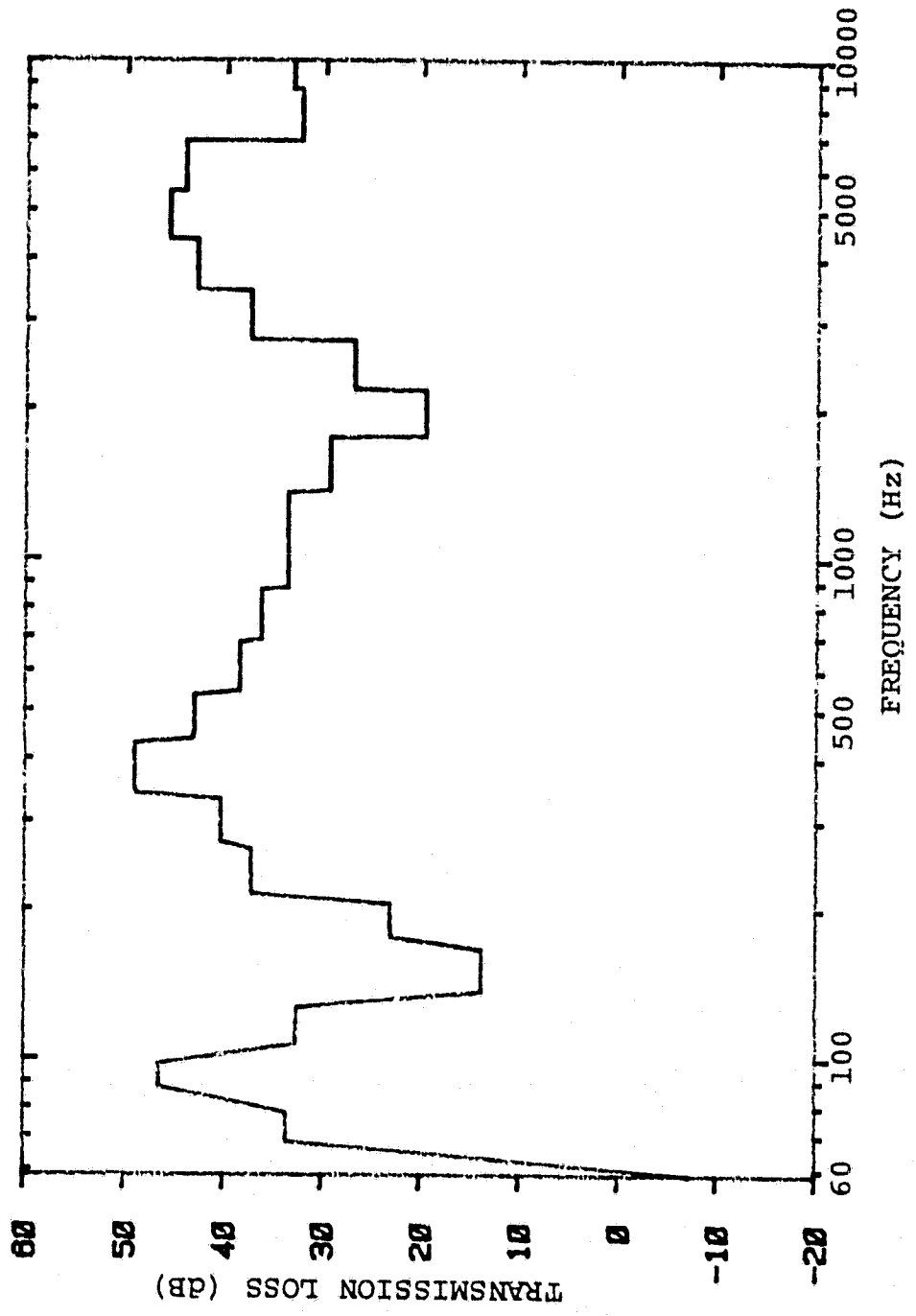

Fig. 3.13
Transmission Loss of the Cylindrical Shell in One-Third Octave Band Analysis.

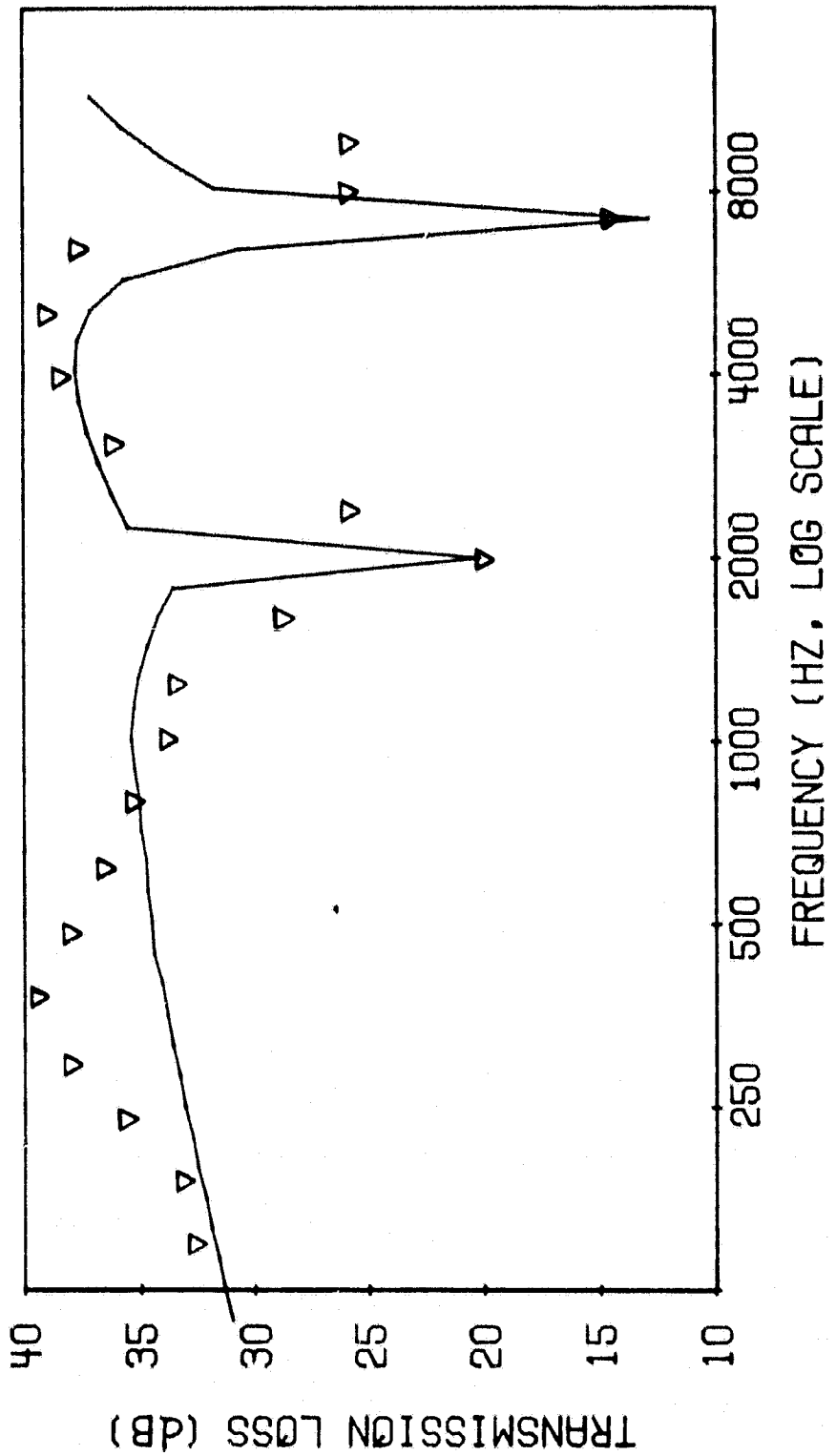

Fig. 3.14
The Experimental Result in One-Third Octave Center Frequencies (V) Compared to the Theoretical Transmission Loss Prediction.

well with the experiment for frequencies above 500 Hz. It is especially noticed that the two dips at the ring frequency (2134 Hz) and at the critical coincidence frequency (7452 Hz) are exactly predicted. However, discrepancies between the theory and the measurement are more pronounced at low frequency. This might be explained in the following ways:

a. As discussed in Section 3.5.1, the interior sound field is not fully diffuse at low frequencies. Hence the use of $p^2/4\rho_o c$ to obtain the incident sound intensity is an invalid assumption.

b. The interior volume of the cylinder does not have enough modes in a frequency band of interest for coupling with the structural mode in the low frequency range. The SEA theory can be completely wrong if none or very few resonant modes exist in certain frequency bands.

c. When the spacing between two microphones is not large enough, the intensity method might result in intensity errors at very low frequencies. This is because of the fact that in measurements with two microphones insufficiently spaced, the phase information of a low frequency wave (large wave length) can easily be in error.

4. REFERENCES

1. Leissa: NASA sp-288 "Vibration of Shells," 1975.

2. Soedel, W., Vibrations of Shells and Plates, Marcel Dekker, Inc., 1981.

3. Donnell, L. H., "Stability of Thin Wall Tubes Under Torsion," NASA Rep. No. 479, 1933.

4. Donnell, L. H., "A Discussion of Thin Shell Theory," Proc. Intern. Cong. Appl. Mech., 1938.

5. Mushtari, K. M., "Certain Generalizations of the Theory of Thin Shells," Izv. Fiz. Mat. ob-va, pri kaz. un-te., Vol. II, No. 8, 1938.

6. Yu, Y. Y., "Free Vibration of Thin Cylindrical Shells Having Finite Lengths with Freely Supported and Clamped Edges," J. of Applied Mechanics, Vol. 22, No. 4, Dec. 1955.

7. Soedel, W., "A New Frequency Formula for Close Circular Cylindrical Shells for a Large Variety of Boundary Conditions," J. of Sound and Vibration, 70 (2), pp. 309-317, 1980.

8. Szechenyi, E., "Approximate Methods for the Determination of the Natural Frequencies of Stiffened and Curved Plates," J. of Sound and Vibration, 14 (3), pp. 401-418, 1971.

9. Szechenyi, E., "Modal Densities and Radiation Efficiencies of Unstiffened Cylinders Using Statistical Methods," J. of Sound and Vibration, 19 (1), pp. 65-81, 1971.

10. Manning, J. E., Maidanik, G., "Radiation Properties of Cylindrical Shells," J. of Acous. Soc. of America, Vol. 36, No. 9, pp. 1691-1698, 1964.

11. Cremer, L., Heckl, M., and Ungar, E. E., Structure-Borne Sound, Springer-Verlag, pp. 455-465, 1973.

12. Crocker, M. J., Forssen, B., Raju, P. K., Mielnicka, A., "Measurement of Transmission Loss of Panels by Acoustic Intensity Technique," Proceedings, Inter-Noise 80, pp. 741-746, 1980.

13. Szechenyi, E., "Sound Transmission through Cylinder Walls Using Statistical Considerations," J. of Sound and Vibration, 19 (1), pp. 83-94, 1971.

14. Lyon, R. H., Statistical Energy Analysis of Dynamic Systems, Chapter 12, MIT Press, 1975.

15. Bjor, O. E., "A Method for Automatic Reverberation Time Measurement," Applied Acoustics, (12), pp. 1-13, 1979.

16. Jaeger, D., "The Reverberation Time Measurement," HL76-27, Herrick Labs, Purdue University, 1976.

17. Nakayama, K., "Prediction of the Sound Pressure Level Inside a Vibrating Rectangular Steel Box Using Statistical Energy Analysis," Master Thesis, Purdue University, 1979.

18. Crocker, M. J., "A Proposal for Research on a Study of Methods to Predict and Measure the Transmission of Sound Through the Walls of Light Aircraft," submitted to NASA, Dec. 1979.

19. Crocker, M. J., "The Response of Structures to Acoustic Excitation and the Transmission of Sound and Vibration," Ph.D. Thesis, the University of Liverpool, 1969.

20. Crocker, M. J., Price, A. J., "Sound Transmission Using Statistical Energy Analysis," J. of Sound and Vibration, Vol. 9, No. 3, pp. 469-486, 1969.